DESIGN AND MICROFABRICATION OF A CMOS-MEMS PIEZORESISTIVE ACCELEROMETER AND A NANO-NEWTON FORCE SENSOR

by

MOHD HARIS MD KHIR

A dissertation submitted in partial fulfillment of the requirements for the degree of

DOCTOR OF PHILOSOPHY IN SYSTEMS ENGINEERING

2010

Oakland University
Rochester, Michigan

Doctoral Advisory Committee:

Hongwei Qu, Ph.D. Chair
Nan K. Loh, Ph.D.
Mohammad-Reza Siadat, Ph.D.
Meir Shillor, Ph.D.

© Copyright by Mohd Haris Md Khir, 2010
All rights reserved

To my wife Jamaliah,my sons Mohd Bukhari, Mohd Amir Firdaus, my daughters

NurAtikah, Nur Anis Suhana, and Nur Afiqah

ACKNOWLEDGMENTS

I would like first to thank my advisor, Dr. Hongwei Qu, for his guidance, advice and support of my research and thesis. His profound expertise especially in CMOS-MEMS field in both theoretical and device fabrication are very helpful and always a source of my inspiration.

I would also like to express my deep appreciation to my PhD. Committee members, Dr. Robert N. K. Loh, Dr. Mohammad Siadat, Dr. Bo-nan Jiang, and Dr. Meir Shillor for their time, advice, and assistant on my research and thesis.

The post microfabrication of the devices was carried out at the Lurie Nanofabrication Facility (LNF), University of Michigan, Ann Arbor, Michigan. Special thanks go to Sandrine Martin, Nadine Wang, Brian VanDerElzen, Brian Armstrong, Russ Clifford, and Steven Sostrom for their support during my work at LNF. I would also like to thank Dr. Kai Sun at the Electron Microbeam Analysis Laboratory, University of Michigan for the assistance in scanning electron microscope (SEM) imaging of the device.

My appreciation also goes to Universiti Teknologi Petronas, Malaysia for sponsoring my studies at the Oakland University. Finally, I am grateful to my family and friends for their support and encouragement. I am indebted to my wife Jamaliah and children Mohd Bukahri, Mohd Amir Firdaus, Nur Atikah, Nur Anis Suhana, and Nur Afiqah.

Mohd Haris Md Khir

ABSTRACT

DESIGN AND MICROFABRICATION OF A CMOS-MEMS PIEZORESISTIVE ACCELEROMETER AND A NANO-NEWTON FORCE SENSOR

by

Mohd Haris Md Khir

Adviser: Hongwei Qu, Ph.D.

This thesis work consists of three aspects of research efforts:

1. Design, fabrication, and characterization of a CMOS-MEMS piezoresistive accelerometer
2. Design, fabrication, and characterization of a CMOS-MEMS nano-Newton force sensor
3. Observer-based controller design of a nano-Newton force sensor actuator system

A low-cost, high-sensitivity CMOS-MEMS piezoresistive accelerometer with large proof mass has been fabricated. Inherent CMOS polysilicon thin film was utilized as piezoresistive material and full Wheatstone bridge was constructed through easy wiring allowed by three metal layers in CMOS thin films. The device fabrication process consists of a standard CMOS process for sensor configuration and a deep reactive ion etching (DRIE) based post-CMOS microfabrication for MEMS structure release. Bulk single-crystal silicon (SCS) substrate was included in the proof mass to increase sensor sensitivity. Using a low operating power of 1.67 mW, the sensitivity was measured as 30.7 mV/g after amplification and 0.077 mV/g prior to amplification. With a total noise

floor of 1.03 mg/√Hz, the minimum detectable acceleration is found to be 32.0 mg for a bandwidth of 1 kHz which is sufficient for many applications.

The second device investigated in this thesis work is a CMOS-MEMS capacitive force sensor capable of nano-Newton out-of-plane force measurement. Sidewall and fringe capacitance formed by the multiple CMOS metal layers were utilized and fully differential sensing was enabled by common-centroid wiring of the sensing capacitors. Single-crystal silicon (SCS) is incorporated in the entire sensing element for robust structures and reliable sensor deployment in force measurement. A sensitivity of 8 mV/g prior to amplification was observed. With a total noise floor of 0.63 mg/√Hz, the minimum detection acceleration is found to be 19.8 mg, which is equivalent to a sensing force of 449 nN.

This work also addresses the design and simulation of an observer-based nonlinear controller employed in a CMOS-MEMS nano-Newton force sensor actuator system. Measurement errors occur when there are in-plane movements of the probe tip; these errors can be controlled by the actuators incorporated within the sensor. Observer-based controller is necessitated in real-world control applications where not all the state variables are accessible for on-line measurements.

TABLE OF CONTENTS

ACKNOWLEDGMENTS iv

ABSTRACT v

LIST OF TABLES xi

LIST OF FIGURES xii

CHAPTER ONE
INTRODUCTION 1

1.1 Introduction to CMOS-MEMS 2

1.1.1 CMOS-MEMS Technologies 2

1.1.2 CMOS-MEMS Micromachining Process 5

1.1.3 CMOS-MEMS Research Cycle 6

1.1.4 CMOS-MEMS Capacitive and Piezoresistive Sensors 8

1.1.5 CMOS-MEMS Piezoresistive Accelerometer 11

1.1.6 CMOS-MEMS Force Sensor 12

1.2 Control of MEMS Actuator and Sensor 12

1.3 Contribution of Thesis 14

1.4 Dissertation Organization 15

CHAPTER TWO
DESIGN AND SIMULATION OF A CMOS-MEMS SENSORS 18

2.1 Design of a CMOS-MEMS Piezoresistive Accelerometer 19

2.1.1 Sensor Self Heating Effect 26

2.1.2 Simulation Results 29

2.1.3 Conclusion 35

2.2 Design of a CMOS-MEMS Nano-Newton Force Sensor 36

2.2.1 Simulation Results 45

2.2.2 Conclusion 48

CHAPTER THREE
OBSERVER-BASED CONTROLLER DESIGN OF A CMOS-MEMS NANO-NEWTON FORCE SENSOR 49

3.1 Sensor Actuator Design 50

3.2 Actuator Model 55

3.3 Feedback Linearization of the Nonlinear Actuator System – Controller Design 58

3.3.1 Input-State Linearization 58

3.3.2 Input-Output Linearization 63

3.4 Nonlinear Observer Design Using Lie Algebraic Exact Error Linearization 64

3.5 Observer-Based Controller Design 69

3.6 Observer-Based Controller Simulation Results 70

3.7 Conclusion 74

CHAPTER FOUR
POST-MICROFABRICATION OF THE CMOS-MEMS SENSORS 76

4.1 Post-CMOS Microfabrication of a CMOS-MEMS Piezoresistive Accelerometer 79

4.2 Post-CMOS Microfabrication of a CMOS-MEMS Nano-Newton Force Sensor 89

4.3 Conclusion 93

CHAPTER FIVE
DEVICE CHARACTERIZATION 94

5.1 Device Packaging 94

5.1.1 Packaging of the Piezoresistive Accelerometer 95

5.1.2 Packaging of the Nano-Newton Force Sensor 96

5.2 Sensor Characterization Setup 96

5.2.1 Piezoresistive Accelerometer Characterization Setup 97

5.2.2 Nano-Newton Force Sensor Characterization Setup 101

5.3 Piezoresistive Accelerometer Characterization 105

5.3.1 Kistler Type 8692B50 Accelerometer Calibration 105

5.3.2 Resistance Measurement 107

5.3.3 Mechanical Test 108

5.3.4 Off-Chip Circuit Test 110

5.3.5 Noise Measurement 110

5.3.6 Dynamic Test 112

5.3.7 Temperature Test 115

5.3.8 Conclusion 117

5.4 Nano-Newton Force Sensor Characterization 119

5.4.1 MS3110 Universal Capacitive Board Calibration 119

5.4.2 Mechanical Test 121

5.4.3 Off-Chip Circuit Test 123

5.4.4 Dynamic Test 124

5.4.5 Noise Measurement 126

5.4.6 Conclusion 127

CHAPTER SIX
CONCLUSIONS AND SUGGESTIONS FOR FUTURE RESEARCH 130

6.1 Overall Conclusions 130

6.2 Suggestions for Future Research 133

APPENDICES

A. MicroElectroMechanical Theory 134

B. Chip Diagram and Instrument Specification 139

REFERENCES 142

LIST OF TABLES

Table 1.1	Etching Techniques for Micromachining the Silicon Substrate	6
Table 2.1	Sensors Desired Performances	19
Table 2.2	Typical CMOS Layers Thickness	20
Table 2.3	Sensor Geometric and Material Parameters	22
Table 2.4	Calculated Values for Thermal Resistances and Capacitances	28
Table 2.5	Typical CMOS Layers Thickness	38
Table 2.6	Geometric and Material Properties	39
Table 3.1	Actuator Parameters and Constants	56
Table 3.2	Resulting Controller and Observer Gains	71
Table 4.1	Typical CMOS Layers Thickness	78
Table 4.2	Anisotropic DRIE Recipe for Back-side Silicon Etching	81
Table 4.3	RIE Recipe for Front-Side SiO_2 Etching	83
Table 4.4	Front-Side Isotropic Silicon Etching	86
Table 5.1	Actual Polysilicon Resistors Measurement	108
Table 5.2	Performance Summary of the Piezoresistive Accelerometer	118
Table 5.3	Performance Summary of the Nano-Newton Force Sensor	129

LIST OF FIGURES

Figure 1.1	CMOS-MEMS research cycle at Oakland University.	8
Figure 1.2	Basic parallel-plate capacitive displacement sensors.	10
Figure 1.3	A uniaxial tensile force in the direction of x.	11
Figure 2.1	A 3D model of the piezoresistive sensor showing the embedded polysilicon resistors in the bimorph beams.	21
Figure 2.2	Schematic cross-section of the released sensor showing the CMOS thin films and their relative locations.	21
Figure 2.3	Circuit model for the self heating of a resistor driven by a voltage source.	26
Figure 2.4	Piezoresistance change in longitudinal direction as a function of out-of-plane acceleration.	29
Figure 2.5	Piezoresistance change in transverse direction as a function of out-of-plane acceleration.	30
Figure 2.6	CoventorWare simulation of the piezoresistance change in longitudinal direction as a function of out-of-plane acceleration.	31
Figure 2.7	CoventorWare modal simulation to estimate the resonant frequencies of the sensor.	32
Figure 2.8	Transient response of the temperature on the bimorph beam simulated using Matlab.	33
Figure 2.9	CoventorWare simulation of the heat flux on the sensor bimorph beam and the thermal resistance equivalent circuit.	34
Figure 2.10	3D model of the force sensor which illustrates the out-of-plane force, F_z at the probe tip and the comb fingers sections.	36
Figure 2.11	Schematic cross-section view of the sensing element where CMOS thin films are used.	37

Figure 2.12	Illustration of the capacitance change when the probe is subject to external force that results in the downward motion of the rotor comb finger.	40
Figure 2.13	Illustration of the sensing structure motion upon a downward force applied to the probe tip.	41
Figure 2.14	Electrical equivalent circuit for the common-centroid configuration of the sensing capacitors.	42
Figure 2.15	Simplified equivalent circuit of the sensor.	43
Figure 2.16	CoventorWare simulation result of capacitance as the function of the out-of-plane force from 1 nN to 1 mN.	45
Figure 2.17	CoventorWare simulation result of the displacement as the function of the out-of-plane force from 1 nN to 1 mN.	46
Figure 2.18	CoventorWare modal simulation to estimate the resonant frequencies of the force sensor.	47
Figure 3.1	3D model of the CMOS-MEMS nano-Newton force sensor.	50
Figure 3.2	Tilting motion due to force perpendicular to the probe tip.	51
Figure 3.3	Illustration of the capacitance change of the sensor when the probe tip is subjected to an external force which results in the downward motion of the rotor finger.	52
Figure 3.4	Undesired in-plane twisting motion.	53
Figure 3.5	Illustration of the actuator rotor finger lateral motion toward the stator finger due to twisting in-plane force.	54
Figure 3.6	Equivalent diagram for a pair of actuator finger.	55
Figure 3.7	The schematic diagram of a nonlinear observer-based controller system.	70
Figure 3.8	Simulation of the observer-based controller state estimation response with the displacement initial condition of 0.2 μm.	72

Figure 3.9	Simulation of the observer-based controller control-input response with the displacement initial condition of 0.2 μm.	72
Figure 3.10	Simulation of the observer-based controller state estimation response with the displacement initial condition of 0.1 μm, 0.2 μm, 0.4 μm, 0.6 μm, and 0.8 μm.	73
Figure 3.11	Simulation of the observer-based controller control-input response with the displacement initial condition of 0.1 μm, 0.2 μm, 0.4 μm, 0.6 μm, and 0.8 μm.	74
Figure 4.1	CMOS-MEMS layout showing the location of the sensor drawn using Mentor Graphic layout tool.	77
Figure 4.2	Schematic cross-section of the released sensor showing the CMOS thin films and their relative locations.	78
Figure 4.3	Back-side photoresist coated around the sensor, and a 4" carrier wafer coated with photoresist with the center of the wafer is cleared for sample placement.	80
Figure 4.4	Schematic cross-section of the sensor, and the Back-side view of the sensor under optical microscope after DRIE process.	81
Figure 4.5	Sample preparation prior to SiO_2 RIE process, which shows a sample on top of 4" and 6" carrier wafers.	82
Figure 4.6	Schematic cross-section of the sensor after SiO_2 RIE, the front-side view of the sensor after metal 3 is exposed, and a gray color in trenches indicates that SiO_2 is fully etched.	83
Figure 4.7	Schematic cross-section of the sensor after silicon DRIE, and image under optical microscope after 10 minutes DRIE process.	84

Figure 4.8 Schematic cross-section of the sensor after isotropic silicon etching, test structure curling after 25 minutes of isotropic etching process, and front-side image under optical microscope after 30 minutes of isotropic etching process. 85

Figure 4.9 Sensor back-side view under optical microscope with inset showing the close-up of the disconnection between substrate and proof mass bottom after 5 minutes of silicon DRIE process, which releases the structure. 87

Figure 4.10 SEM image of the fabricated CMOS-MEMS accelerometer with inset showing the bimorph beams where the piezoresistors are located. 88

Figure 4.11 Back-side view of the sample coated with photoresist and placed on the 4" carrier wafer. 89

Figure 4.12 Schematic cross-section of the nano-Newton force sensor after back-side silicon DRIE process. 90

Figure 4.13 Schematic cross-section of the nano-Newton force sensor after front-side SiO_2 RIE process and the sensor front-side view under the optical microscope. 91

Figure 4.14 Schematic cross-section of the nano-Newton force sensor after the sensor is fully released and the SEM picture of the sensor with the inset showing the close-up view of the sensing comb fingers. 92

Figure 5.1 Test board on which the DUT and the reference accelerometer are mounted. 95

Figure 5.2 Nano-Newton force sensor chip in a ceramic 6 pins DIP package. 96

Figure 5.3 Piezoresistive accelerometer characterization setup. 98

Figure 5.4 Schematic diagram of the Wheatstone bridge configuration implemented for the piezoresistive accelerometer. 99

Figure 5.5	The schematic diagram of the instrumentation amplifier and the high Q band-pass filter.	100
Figure 5.6	Nano-Newton force sensor characterization setup.	102
Figure 5.7	MS3110 universal capacitive circuit schematic diagram.	102
Figure 5.8	The schematic diagram of the amplifier (AD 627) and the low pass filter used for nano-Newton force sensor characterization.	104
Figure 5.9	Force sensor and its circuitry in the Faraday's cage.	104
Figure 5.10	Kistler reference accelerometer on Piezotronics hand held shaker.	106
Figure 5.11	Calibrated reference accelerometer output at 1g acceleration.	106
Figure 5.12	Polysilicon resistors configuration including the 16 DIP pin number.	107
Figure 5.13	Impulse signal applied to the sensor.	109
Figure 5.14	Dynamic frequency response of the sensor with impulse signal.	109
Figure 5.15	Overall noise of the system including the sensor, amplifier and filter circuits.	111
Figure 5.16	Electrical (circuit) noise of the amplifier and filter circuit measured using HP signal analyzer.	112
Figure 5.17	A complete wiring connection of the characterization equipment for piezoresistive accelerometer dynamic test.	113
Figure 5.18	Piezoresistive and reference accelerometers response to 3g acceleration.	114
Figure 5.19	Linear responses of the accelerometers with acceleration from 1g to 7g.	114

Figure 5.20 Linear resistance change with temperature change from 22 ^{o}C to 104 ^{o}C. 116

Figure 5.21 Resistance change with temperature change from 295 ^{o}K to 377 ^{o}K. 116

Figure 5.22 MS3110 board oscillator frequency. 120

Figure 5.23 Impulse signal applied to the sensor. 121

Figure 5.24 Dynamic frequency response of the sensor with impulse signal. 122

Figure 5.25 External amplifier and filter circuit. 123

Figure 5.26 A complete wiring connection of the characterization equipment for the nano-Newton force sensor dynamic test. 124

Figure 5.27 Nano-Newton force sensor response to 1g acceleration. 125

Figure 5.28 Response of the amplifier and filter circuits with no sensor input. 126

Figure 5.29 Overall noise of the system consists of the sensor and amplifier and filter circuits. 127

Figure A.1 A segment of a beam in pure bending. 135

Figure A.2 A bent cantilever beam. 137

Figure B.1 The schematic diagram of the chip pin-out connection. 140

Figure B.2 The schematic diagram of the MS3110 universal capacitive readout circuit. 141

CHAPTER ONE

INTRODUCTION

Microelectromechanical systems (MEMS) devices have been initiated and enhanced from the integrated circuit industry since 1950s. Charles S. Smith from Bell Telephone Laboratories for example reported a uniaxial tension causes a change of resistivity (piezoresistive effect) in silicon and germanium of both *n* and *p* types in 1953 [1]. In 1967, Harvey C. Nathanson and his colleagues have successfully designed and fabricated a variable transistor known as the resonant gate transistor (RGT), which utilize an electrostatically excited tuning fork to vary the gate electrode with respect to the substrate [2]. Hewlett-Packard pioneered the technology of silicon micromachined ink-jet printer nozzles in 1978 [3]. In 1979, Kurt E. Petersen reported a newly integrated planar ink-jet nozzles structure fabricated by anisotropically etching silicon [4]. Bulk and surface micromachining based on silicon substrate for a variety of MEMS devices have dominated the microfabrication of micro devices ever since. Micro motors fabricated in 1988 by Long-Sheng Fan and his colleague using 1.0 μm to 1.5 μm thick polycrystalline silicon is mentioned in [5]. An interesting thermal accelerometer uses thermopiles to detect the temperature difference between the heat source and the sink has been highlighted by U. A. Dauderstadt [6] in 1995. In 2000, a single-crystalline-silicon micro-gyroscope has been fabricated in a single wafer using surface/bulk miromachining process is reported in [7]. The trend of utilizing silicon based material to fabricate MEMS devices has since been greatly appreciated as discussed in [8]-[10].

1.1 Introduction to CMOS-MEMS

The field of complementary-metal-oxide semiconductor micro-electro-mechanical systems (CMOS-MEMS) dates back to mid 1980s, but has grown substantially in the past decade especially since the availability of commercial foundry services from fabrication companies such as IBM, TSMC, and AMI (ON Semiconductor) to support CMOS-MEMS development. CMOS-MEMS is an approach to building MEMS structures directly in widely available CMOS semiconductor materials. The technology represents a breakthrough in monolithic devices. Unlike other MEMS technologies, CMOS-MEMS devices are not fabricated in the thin films on top of CMOS, but instead are fabricated from the metal-dielectric layers of the CMOS itself that are deposited during the standard CMOS processing flow. The same metal/dielectric layers which make up the mechanical MEMS structures also form the electronic circuits which are integrated with the MEMS structures, lead to the highest possible performance. CMOS-MEMS technology enables multiple sensors and associated electronics to be integrated into one common platform. The level of integration available in CMOS-MEMS results in small sizes, high-performance, and cost-effective solutions for numerous device categories such as inertial (accelerometer and gyroscope), RF (resonators and switches), chemical (gas sensors), and acoustic (microphone and speakers).

1.1.1 CMOS-MEMS Technologies

The integration of MEMS structures with CMOS circuits for signal conditioning can be implemented using three approaches; pre-CMOS, intra-CMOS, and post-CMOS technology.

In pre-CMOS technology, MEMS devices are processed first followed by a standard CMOS steps to build the circuit. This process is also known as 'MEMS-first' fabrication approaches [11]. Pre-CMOS technology is developed by Sandia National Laboratory. The M^3EMS (Modular, Monolithic Micro-Electro-Mechanical Systems) technology was the first demonstrations of the MEMS-first integration concept [12, 13]. In this approach, multi-layer polysilicon microstructure is built in a trench, which has been etched into the bulk silicon. After the formation of polysilicon microstructures, the trench is refilled with LPCVD oxide and planarized with a CMP (chemical mechanical polishing) step. Subsequently, the wafers with embedded microstructures are used as starting material in CMOS process, fabricating CMOS circuitry in the area adjacent to MEMS area. CMOS metallization is used to interconnect circuitry and MEMS areas. The back-end of the process requires additional masks to open the protective silicon nitride over the MEMS areas prior to the release of the polysilicon structures by silicon oxide sacrificial etching.

In intra-CMOS technology, MEMS devices are processed in between the regular CMOS process steps. Intermediate micromachining is most commonly used to integrate polysilicon microstructures in CMOS/BiCMOS process technologies [11]. Commercially products fabricated with intermediate micromachining, include Analog Devices ADXL series accelerometers and ADXRS series gyroscopes [14], Infineon Technologies' KP100 series pressure sensors [15] and Freescale's MPXY8000 series pressure sensors [16].

In post-CMOS technology, MEMS devices are processed after the completion of the CMOS process steps [17, 18]. In the case of post-CMOS micromachining, the MEMS devices are either built: (1) from the CMOS layers themselves, or (2) from additional

layers deposited on top of CMOS wafer. In the first approach, most of the microstructures are already formed within the regular process sequence. Further process steps such as etching is only required to release the microstructures from the CMOS thin film and substrate. The fabrication of MEMS devices for this work utilizes the first approach of the post-CMOS process sequence. CMOS thin film layers and bulk silicon are used as the material for the MEMS devices. In the second approach, MEMS devices are built on top of a CMOS substrate. Surface micromachining and sacrificial etching are normally used to release the microstructure. Add-on micromachining requires a good planarity of the underlying CMOS substrate and electrical and mechanical contact between microstructures and CMOS circuits. The constraint of the second approach is the limitation of the Aluminum metallization in the CMOS that is used for the signal routing, which has a melting point of ~600 °C. The LPCVD deposition and annealing of a thin polysilicon films used as a microstructure for example will require a process temperature of ≥ 900 °C. Thus, special structure materials and sacrificial layers that can be deposited and processed at lower temperature such as SiGe/Ge are required.

The advantages of post-CMOS technology compare to other CMOS technologies can be summarized as follows:

- Single-crystal silicon (SCS) can be used as the microstructures compare to only polysilicon material normally use as the microstructures in pre-CMOS and intra-CMOS technology. SCS material has better mechanical performance compare to polysilicon. Thus, increases device performance and sensitivity.

- Structural curling due to residual stress after post-microfabrication can be reduced or avoided with the incorporation of SCS as the microstructures.
- Microfabrication flexibility. Microfabrication process can be performed at numerous foundries such as IBM, TSMC, AMI, ...etc. On the hand, pre-CMOS and intra-CMOS microfabrication must be performed at a dedicated foundry.
- Post-microfabrication of MEMS devices can be performed at a dedicated MEMS foundry

1.1.2 CMOS-MEMS Micromachining Process

The basic microfabrication technologies described in Section 1.1.1 earlier are often combined with special micromachining steps to produce three-dimensional microstructures. The micromachining techniques are categorized into bulk and surface micromachining processes. In the case of bulk micromachining, the microstructure is formed by machining the relatively thick bulk substrate material, whereas in the case of surface micromachining, the microstructure comprises thin-film layers, which are deposited on top of substrate and are selectively removed in a defined sequence to release the MEMS structure [11].

Bulk micromachining techniques, i.e. etching techniques to machine the (silicon) substrate, can be classified into isotropic and anisotropic, and into wet and dry etching techniques, as can be seen in Table 1.1 [19].

Surface micromachining technique involves sacrificial-layer etching [12]. In this process, a microstructure, such as a cantilever beam or plate, is released by removing a sacrificial thin-film material, which was previously deposited underneath the

microstructure. The release of polysilicon microstructures by removing a sacrificial silicon dioxide film is the most popular surface micromachining technique [12]. Metallic microstructures deposited by low-temperature PVD processes can use polymer films as sacrificial layers, which are removed using, e.g., an oxygen plasma [20, 21].

1.1.3 CMOS-MEMS Research Cycle

CMOS-MEMS research approach adopted at the Oakland University falls in the bulk CMOS-MEMS category. It involves a long and comprehensive research cycle. The device research development begins with the theoretical studies and ends at the characterization stage, as shown in Fig. 1.1. Referring to Fig. 1.1, the cycle starts with on-paper theoretical design of the CMOS-MEMS devices as shown in Fig. 1.1(a).

Table 1.1

Etching Techniques for Micromachining the Silicon Substrate

Type	Wet etching	Dry etching
Isotropic	HNA system	Vapor-phase etching
	$HF\text{-}HNO_3\text{-}CH_3COOH$	XeF_2
Anisotropic	Alkali metal hydroxide solutions	Plasma etching
	KOH, NaOH	RIE, deep-RIE
	Ammonium hydroxide solutions	
	$(CH_3)_4NOH$ (TMAH), NH_4OH	
	EDP solutions	
	hydrazine	

Matlab simulation software is used on the second design stage to estimate device electrical and mechanical performances as shown in Fig. 1.1(b). The simulation results obtained from Matlab is further validated using the comprehensive CoventorWare finite element analysis (FEA) software as illustrated in Fig. 1.1(c). Integrated with Electro-thermal-mechanical solver, CoventorWare solver can be used to analyze temperature, capacitance, and mechanical behavior of the device. Once all the simulation results have satisfied the design performance requirement, the next step is to draw the layout of the device using either CoventorWare software itself or a more dedicated layout editor such as Mentor Graphic as indicated in Fig. 1.1(d).

The selection of the layout tools is dependent on the fabrication technology and the fabrication foundry. In this research, AMI (ON Semiconductor) 0.5 μm CMOS technology is used to design and fabricate the device through a multiple-wafer project service agent (MOSIS). Mentor Graphic software is used for the layout design due to its capability and availability of AMI 0.5 μm CMOS technology file. The device design represented by a layout set is then taped out to CMOS foundry through MOSIS for CMOS fabrication.

The returning chip, which is still in solid condition with all the microstructures connected to substrate is then scheduled for the post-CMOS microfabication process as shown in Fig. 1.1(f). Using a customize process recipes, through post-CMOS microfabrication, the movable sensor structures are then released from the substrate. For this research, the post-CMOS microfabrication process is conducted at the Lurie nanofabrication facility (LNF), University of Michigan.

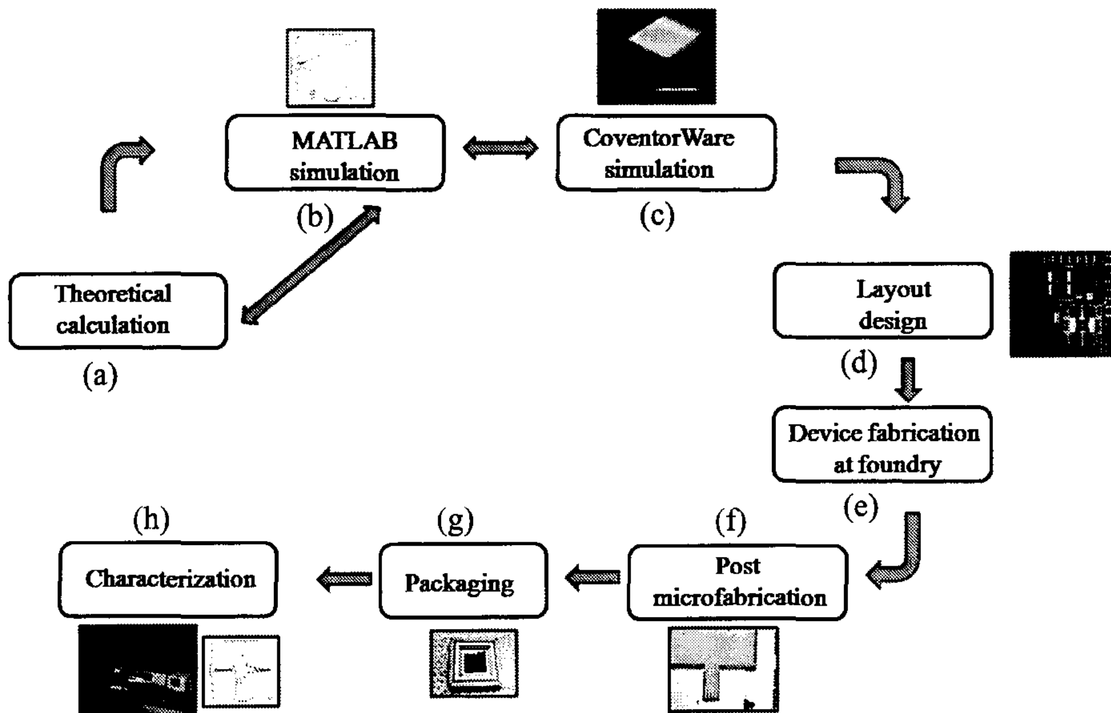

Fig. 1.1. CMOS-MEMS research cycle at Oakland University.

Prior to device characterization, each sensor is packaged and bonded using suitable package such as ceramic dual in-line package (DIP) as demonstrated in Fig. 1.1(g). The final step is to perform device characterization as shown in Fig. (1.1h). Device performances such as mechanical, off-chip, noise measurement, and temperature test have been conducted.

1.1.4 CMOS-MEMS Capacitive and Piezoresistive Sensors

This section discusses the operating principle of the CMOS-MEMS capacitive and piezoresistive sensors that have been developed in this research. CMOS-MEMS

sensors mostly use miniaturized cantilever-type springs that convert force into a displacement, which can be measured using either capacitive [22, 23], piezoelectric [24] or piezoresistive [25, 26] sensing principles.

Capacitive sensors normally employ capacitance change of a system to measure the physical parameters input to the system. Capacitance is a property that exists between any conductive surfaces named electrodes within some proximity. Changes in the displacement between two surfaces change the capacitance. It is this change of capacitance that capacitive sensors use to indicate changes in position of a target. Design of the sensing elements in a capacitive sensor usually takes two forms: parallel-plate capacitors oriented in the vertical (perpendicular to substrate) direction, as shown in Fig. 1.2(a), or, sidewall parallel-plate capacitors oriented in the lateral (in-plane to substrate) direction, as shown in Fig. 1.2(b) [11]. The sidewall capacitors are usually formed from interdigitated beam fingers, called 'comb', to increase the capacitance in the given layout area as illustrated in Fig. 1.2(b). For this research, the interdigitated beam fingers are used to detect the sidewall capacitance change, which will be elaborated in Chapter Two.

A Piezoresistive sensor depends on the piezoresistive effect. Under this effect, electrical material will change its resistance when it experiences a strain deformation (differential deformation) due to certain loading or force applied to the material. When a material is stretched within the limits of its elasticity such that it does not break or permanently deform, it will become narrower and longer. This is minimal in semiconductors such as silicon. The major effect is the strain that caused the resistivity change. The strain is defined as change in length per unit length, $\Delta L/L$.

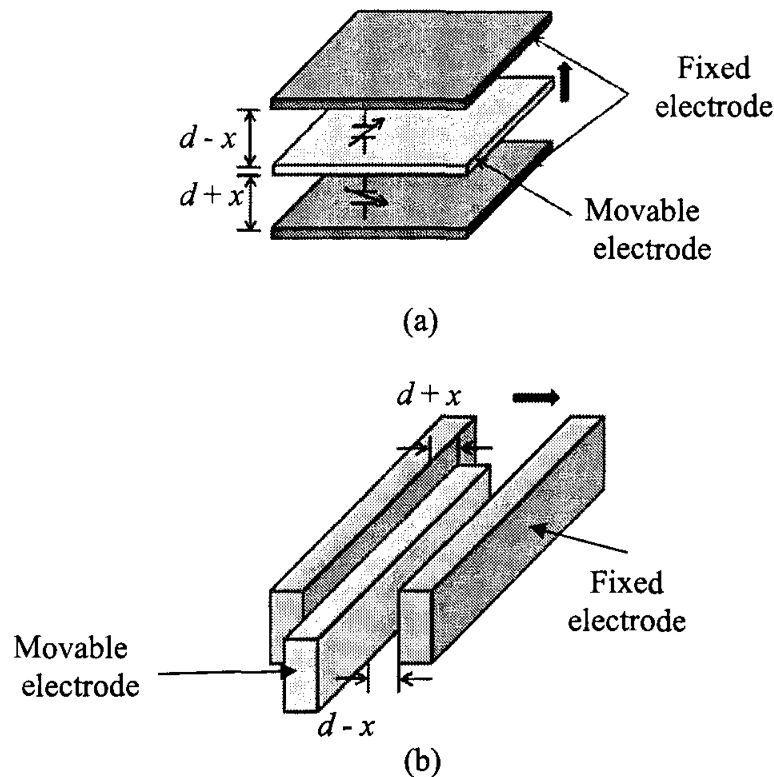

Fig. 1.2. Basic parallel-plate capacitive displacement sensors: (a) vertical plate electrodes, and (b) sidewall electrodes formed with interdigited comb fingers. The arrow shows the direction of motion.

PUSAT SUMBER MAKLUMAT
UNIVERSITI TEKNOLOGI PETRONAS

The change of resistance in metal due to an applied mechanical load was discovered by Lord Kelvin in 1856. Large piezoresistive effects in silicon and germanium materials were discovered in 1954 by Smith [3]. Fig. 1.3 illustrates an example of a uniaxial loading in the direction of x. The uniaxial loading effect contributes to axial stress, σ_x, and strain, ε_x. The relationship between the change of resistance and the strain is defined by the gauge factor, G [11], which will be detailed in Chapter Two.

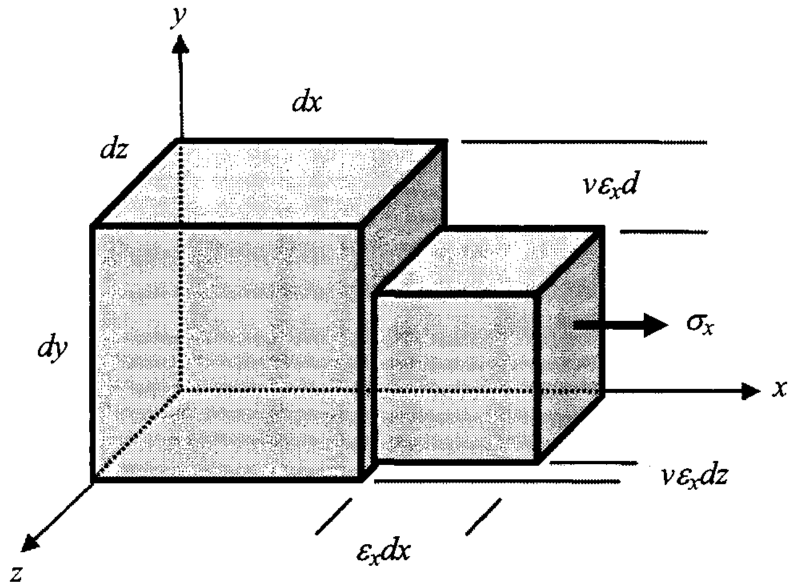

Fig. 1.3. A uniaxial tensile force in the direction of *x*.

1.1.5 CMOS-MEMS Piezoresistive Accelerometers

A number of CMOS-MEMS piezoresistive accelerometers have been demonstrated, in most of which only CMOS thin film micro-cantilever structures were used as proof mass [27-30]. Although the surface micromachining process employed for the creation of these devices is quite simple and cost-effective, yet due to the small structure thickness, the devices suffer low sensitivity and other shortcomings. Moreover, the residual stress in the CMOS thin films often causes large structure curling. Thus, the area and mass of the proof mass structure are also limited. Deep reactive ion etching (DRIE) based dry bulk CMOS-MEMS technology has paved ways for microfabrication

of various devices with robust MEMS structures and considerable device sizes [31, 32]. Compared with wet process for single-crystal silicon (SCS) proof mass manufacturing [33], DRIE method is more effective and environment-friendly due to its enclosed processing.

1.1.6 CMOS-MEMS Force Sensor

Sensors and probes for measurement of small forces ranging from pico Newton (pN) to milli Newton (mN) have been widely explored in various fields such as cell motility study [34, 35] and micro object manipulations research [36, 37]. Most MEMS force sensor designs as reported in [36, 37] have utilized in-plane (lateral) sensing mechanism, which has inherent constrains such as pull-in effect and complicated electrical isolation. Moreover, the use of silicon on insulator (SOI) as structural material as demonstrated in [36], not only complicates the sensor wiring, but also significantly increases the cost for device integration. CMOS-MEMS technology offers an ideal approach for monolithic integration of sensors and conditioning circuits, which is critical for low parasitic system such as small force sensors [38]. Plasma etching based bulk CMOS-MEMS technology has also allowed large proof mass, robust sensor structures in addition to easy integration and rapid device prototyping [39].

1.2 Control of MEMS Actuator and Sensor

MEMS force sensors have been actively explored for biomedical applications. A small dimensional device yet with high sensitivity has allowed MEMS force sensors to measure extremely small forces ranging from milli-Newton to pico-Newton. The design and various applications of such force sensors have been studied and presented [36, 37],

[40-42]. The integration of an actuator (a micro gripper), and a force sensor with a gripping force of 380 μN at a driving voltage of 140 V has been demonstrated in [46]. The application of a capacitive force sensor used to characterize flight behaviour of fruit flies (*Drosophila melanogaster*) was investigated in [37]. In [40], an electrostatic micro force sensor capable of sensing forces from 490 μN to 900 μN has been discussed. A fabrication of multi-degree-freedom force sensor that operates up to 500 μN was explained in [41].

Generally, MEMS sensors operate in an open-loop environment. Challenges have emerged when certain objectives of the measurements are needed. Many researchers have incorporated feedback systems including sensing and actuating elements into MEMS sensors to achieve closed-loop measurement. In [42], the authors suggested the use of a PID controller for force tracking of a micro grasping system with a reference input of 8 μN. Similar force tracking objective achieved by using the robust nonlinear control technique for a piezoresistance nano mechanical-cantilever system was proposed in [43]. A state-feedback force controller in [44] was used in a magnetic levitation system to evaluate the bonding quality between circuit and pads. In [45], phase-locked loop control method was utilized to ensure the operating of MEMS actuators at their resonant frequency. Another application which utilized a Taylor series approximated state-feedback to control the deflection of a parallel-plate electrostatic actuated microgripper was presented in [46].

1.3 Contribution of Thesis

The main focus of this research is on the design, simulation, fabrication, and characterization of two new CMOS-MEMS devices: a piezoresistive accelerometer and a nano-Newton force sensor. A low g piezoresistive accelerometer, which utilizes the piezoresistivity effects, is implemented using inherent CMOS polysilicon as the sensing material. This device is suitable for many applications such as motion sensing in laptop computer, mobile phones, PDAs, hard-disk and CD-drive systems, cameras, and gaming [47]. The second CMOS-MEMS device is a nano-Newton force sensor, which utilizes capacitive sensing principle. It is suitable for many biological applications including cell motility study in which flagellar force measurement on the range of pico-Newton to nano-Newton is needed. AMI 0.5 μm CMOS technology has been used for device fabrication. A Deep reactive ion etching (DRIE) based dry bulk post-CMOS technology is used for device release.

In addition to CMOS-MEMS device fabrication and characterization, this research also explores the potential integration of CMOS-MEMS and control systems for reliable device operation. This aspect of study is to prevent certain device operation issues such as the inherited pull-in effect existing in the capacitive sensor or excessive unnecessary force that may damage the sensor. An actuator system is integrated in the sensor system to provide a feedback for device stabilization. An observer-based controller technique is used for the state estimation and controller design. Actuator model using mass-spring-damper system is used for device simulation.

1.4 Dissertation Organization

Chapter One is dedicated to the introduction of the MEMS research related to this thesis work. This includes the introduction and history of MEMS and CMOS-MEMS. The author also explains the advantages of post-CMOS technology compared to pre-CMOS and inter-CMOS technologies from a perspective of device fabrication. This chapter also introduces the typical CMOS-MEMS research cycle. Current CMOS-MEMS piezoresistive and capacitive sensors are summarized with the inclusion of current literatures on similar topics. Next, the necessity of control for MEMS devices is also explained in Chapter ONE. Finally, author's contribution on CMOS-MEMS research is summarized.

Chapter Two details the design and simulation of the proposed CMOS-MEMS piezoresistive accelerometer. Compared to the reported devices, higher sensor sensitivity and larger process tolerance are achieved for this sensor by using a maskless bulk CMOS-MEMS microfabrication technology to include single-crystal silicon (SCS) as proof mass. Inherent CMOS SiO_2/Aluminum bimorph layers are employed as sensing structures. In the bimorph beams, four polysilicon resistors are appropriately designed to harvest the largest piezoresistance. Using multiple CMOS metal layers, the four polysilicon resistors are conveniently wired to form a full sensing Wheatstone bridge for even higher sensitivity. Next in the same chapter, a CMOS-MEMS nano-Newton force sensor employing out-of-plane sensing mechanism is designed and simulated. Due to its capability of out-of-plane sensing and high sensitivity, it is particularly suitable for biomedical application. Unlike most available force sensors, this device is designed to sense forces that are perpendicular to the sensor plane. This will greatly facilitate device

deployment in force measurement. To validate the unique sensing mechanism, in this work no conditional circuit is integrated on the chip. Instead, a commercially available universal capacitive sensing circuit has been used in device test. Common-centroid wiring of the symmetrically partitioned sensing capacitors allows fully differential sensing and offset cancelation for larger sensitivity.

In Chapter Three, an observer-based controller design for a CMOS-MEMS nano-Newton force sensor actuator system is discussed. The out-of-plane measurement takes place in the sensor system when the sensor is subjected to a force at the probe tip in the z-direction. However, possible twisting in-plane motions (x-y plane) of the sensing elements could occur, which will give rise to out-of-plane measurement errors, or even damage the sensor in severe cases. Therefore, the objective of the investigation is to design of an observer-based nonlinear controller that employs an electrostatic actuator to stabilize the in-plane twisting motions of the sensing elements. The nonlinear controller design utilizes the input-states and input-output feedback linearization technique, while a nonlinear observer is designed to estimate the unknown states. It is well known that observer-based controllers are employed in most, if not all, real-world control applications where all the state variables are required for feedback control but not all of these variables are accessible for on-line, real-time measurements, and/or where the measurements are corrupted by noise.

In Chapter Four, a post-CMOS microfabrication process for the fabrication of the two devices explored in this research is elaborated. The process was developed at Lurie nanofabrication facility (LNF), University of Michigan, Ann Arbor. A Deep reactive ion etching (DRIE) based dry bulk post-CMOS technology is used for device release.

Etching processes are discussed with the inclusion of process schematic cross-section, optical microscope images, and scanning electron microscope (SEM) images for fabrication result examination.

In Chapter Five, the characterization process and results for the piezoresistive accelerometer and nano-Newton force sensor are elaborated and discussed. This includes device packaging, equipment setup and calibration, electrical, mechanical, dynamic, noise, and thermal tests. Test results and device performance are included and discussed.

Important conclusions drawn from the finding in this research are presented in Chapter Six. Future work for device performance, control improvement, and monolithic integration are discussed as well.

CHAPTER TWO

DESIGN AND SIMULATION OF A CMOS-MEMS SENSORS

This chapter presents the design and simulation of the two CMOS-MEMS devices; a piezoresistive accelerometer and a nano-Newton force sensor. Sensors design and fabrication are based on AMI (On Semiconductor) 0.5 μm CMOS technology. The objectives of this research are to design and fabricate these sensors that will meet the following specifications as listed in Table 2.1. Both sensors are expected to operate in out-of-plane motion and with device resonant frequency between 1.0 kHz to 1.5 kHz. This chapter can be divided into two main sections. For the piezoresistive accelerometer, the detectable accelerations are expected to be less than 10g while the sensing force detectable by the nano-Newton force sensor is between nano-Newton to pico-Newton range. Section 2.1 discusses the design of a CMOS-MEMS piezoresistive accelerometer, which includes the theoretical device design, sensor's self heating effect, simulation results, and the conclusion. Section 2.2 elaborates the design of a CMOS-MEMS nano-Newton force sensor, which includes the theoretical device design, the simulation results, and the conclusion. Analytical calculation and simulation utilize MATLAB software as the first design step to estimate sensors performance. The results are then verified using CoventorWare a comprehensive MEMS finite element analysis (FEA) software before proceeding to layout design using Mentor Graphic software.

Table 2.1

Sensors Desired Performances

Piezoresistive Accelerometer	Desired Performance
Sensing axis Resonant frequency Acceleration	Out-of-plane (z-axis) 1.0 kHz to 1.5 kHz < 10 g
Nano-Newton force sensor	**Desired Performance**
Sensing axis Resonant frequency Sensing force	Out-of-plane (z-axis) 1.0 kHz to 1.5 kHz pN to nN-Newton

2.1 Design of a CMOS-MEMS Piezoresistive Accelerometer

Fig. 2.1 shows a 3-D model of the piezoresistive accelerometer with inset showing the cross-sectional view of the CMOS bimorph beams in which sensing poly crystalline silicon piezoresistors are embedded [48]. Inset "A" and "B" shows the cross-sections of the polysilicon resistors that are arranged in longitudinal and transverse orientation, respectively. The sensor has a single crystal silicon (SCS) proof mass with a dimension of 500 μm × 500 μm in size and approximately 40 μm of structural thickness. The SCS proof mass is anchored through four SiO_2/Al bimorph beams that consist of inherent CMOS thin films with a total thickness of approximately 5 μm. The dimension of each bimorph beam is 200 μm × 13 μm. The inherent CMOS polysilicon layer (polysilicon 1), which is used as the piezoresistive sensing material for this device, has a thickness of approximately 0.35 μm, according to the standard AMI 0.5 μm CMOS technology used in this project. The schematic cross-section of the CMOS thin films and their spatial locations are illustrated in Fig. 2.2. The typical CMOS layer thickness in

AMI 0.5 μm CMOS technology, is listed in Table 2.2 [49]. Other parameters such as the sensor geometric and material properties used in sensor design and their values are given in Table 2.3.

When the sensor is subject to an out-of-plane motion (z-axis), the induced stress on the longitudinal and transverse polysilicon resistors will result in the relative change of resistance $\Delta R/R$ given by

$$\frac{\Delta R}{R} = \left(\frac{\Delta R}{R}\right)_l = G_{polyl}\varepsilon_x , \quad (2\text{-}1)$$

$$\frac{\Delta R}{R} = \left(\frac{\Delta R}{R}\right)_t = G_{polyt}\nu\varepsilon_x , \quad (2\text{-}2)$$

Table 2.2

Typical CMOS Layers Thickness

Layer	Thickness (μm)
Single Crystal Silicon (SCS)	~250
Field Oxide under Poly, H_{ox}	0.4
Field Oxide under Metal 1	0.375
Gate Oxide	0.0135
Polysilicon, t_{poly}	0.35
Metal, H_{Al}	0.69
Boro-phospho-silicate-glass (BPSG)	0.7

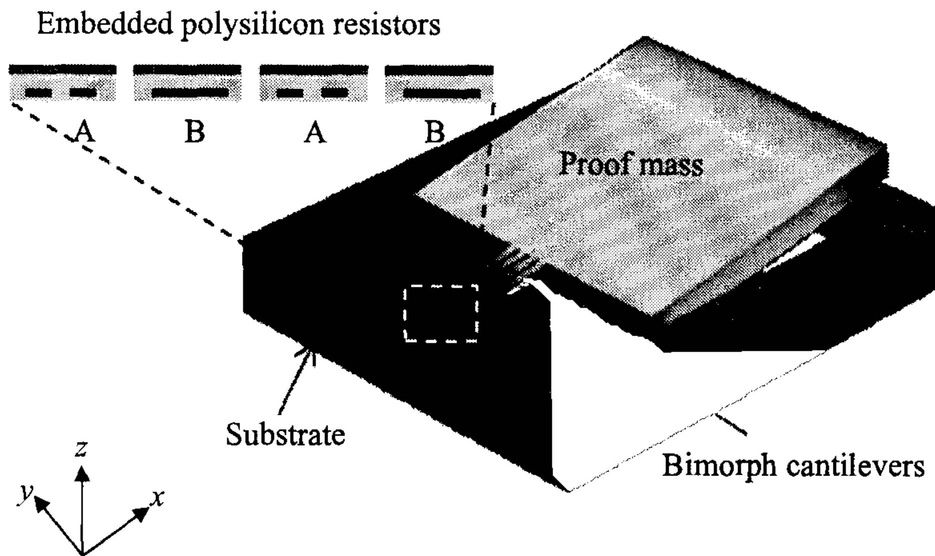

Fig. 2.1. A 3D model of the piezoresistive sensor showing the embedded polysilicon resistors in the bimorph beams.

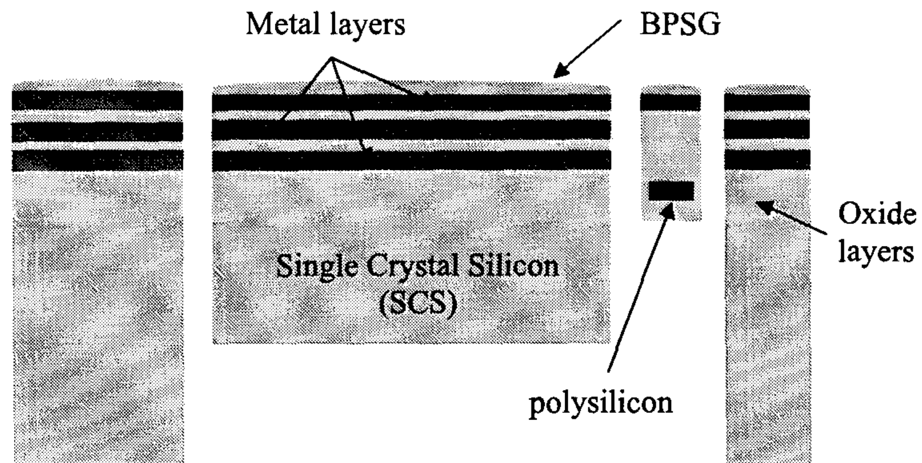

Fig. 2.2. Schematic cross-section of the released sensor showing the CMOS thin films and their relative locations.

Table 2.3

Sensor Geometric and Material Parameters

Parameters	Symbol	Value	Unit
Geometric:			
Bimorph beam thickness from polysilicon layer	H_b	4.2	μm
Bimorph beam width	W_b	13	μm
Bimorph beam length	L_b	200	μm
Proof mass thickness	H_{pm}	40	μm
Proof mass width	W_{pm}	500	μm
Proof mass length	L_{pm}	500	μm
Polysilicon length, width	L_{poly}, W_{poly}	49.4, 1.2	μm
Proof mass weight		1.05×10^{-7}	Kg
Electrical:			
Polysilicon sheet resistance	$R_{\square}$	26.1	Ω/□
Polysilicon TCR	α_{poly}	5.85×10^{-3}	K^{-1}
Polysilicon resistivity	ρ_{poly}	9.135	Ω.μm
Mechanical:			
Aluminum Young's modulus	E_{Al}	65	GPa
SiO_2 Young's modulus	E_{SiO2}	70	GPa
Silicon density	ρ_{Si}	2330	Kg/m^3
Thermal:			
Aluminum thermal conductivity	κ_{Al}	237	W/(K.m)
SiO_2 thermal conductivity	κ_{ox}	1.1	W/(K.m)
Silicon thermal conductivity	κ_{Si}	170	W/(K.m)
Polysilicon thermal conductivity	κ_{poly}	29	W/(K.m)

where the subscript '*l*' and '*t*' denote the longitudinal and transverse relative change of resistance, v is the Poisson's ratio of the silicon having the value of 0.27 while G_{polyl} and G_{polyt} are the longitudinal and transverse gauge factor.

In AMI 0.5 μm CMOS technology used in this work, the polysilicon layer has a nominal sheet resistance, ρ_s of 26.1 Ω/□ [49] which is equivalent to the resistivity, ρ_{poly} of 9.14×10^{-4} Ω.cm and a boron doping concentration of 1.42×10^{19} cm^{-3}. This amount of doping concentration corresponds to the longitudinal and transverse gauge factor of 40 and -15, respectively [50]. The resistivity of the polysilicon can be determined using

$$\rho_{poly} = \rho_s t_{poly}, \tag{2-3}$$

where t_{poly} is 0.35 as defined in Table 2.2 and ε_x is the axial strain. The relationship between the axial and transverse strains can be evaluated using

$$\varepsilon_t = -v\varepsilon_x. \tag{2-4}$$

Referring to Fig. 2.1 and Appendix A.1, the axial strain, ε_x in the direction of x, which occurs on the bimorph beam, is given by

$$\varepsilon_x = -\frac{z}{R_c}, \tag{2-5}$$

where z is the distance from the neutral axis and R_c is the radius of curvature of the bending beam [51]. Since the Young's modulus of aluminum and silicon dioxide (SiO_2) material are close, it is safe to assume that the neutral axis is at the centre of the bimorph beam. The beam bending moment is required to solve Eqn. (2-5). The beam bending moment can be obtained by the integration of the stress through the thickness of the

beam, H_b and is given by [51]

$$M = \int_{-H_b/2}^{H_b/2} \left[\left(W_b dz \right) \sigma_x \right] .z \,, \tag{2-6}$$

where σ_x is the axial stress of the beam. Since the relation between the stress and strain is $\sigma_x = E\varepsilon_x$, Eqn. (2-6) led to

$$M = -\int_{-H_b/2}^{H_b/2} \left[\left(W_b dz \right) \frac{Ez^2}{R_c} \right] = \frac{EW_b}{R_c} \int_{-H_b/2}^{H_b/2} z^2 dz = -\frac{EW_b H_b^3}{12 R_c} \,, \tag{2-7}$$

which can be further simplified to

$$\frac{1}{R_c} = -\frac{12M}{EW_b H_b^3} = -\frac{M}{EI} \,, \tag{2-8}$$

where I is the beam inertia and is given by

$$I = \frac{W_b H_b^3}{12} \,. \tag{2-9}$$

Referring to Appendix A.2, the solution of the bending beam with proof mass, which result in the maximum bending stress at the beam support to substrate ($x = 0$) is given by

$$\frac{1}{R_c} = \frac{d^2 w}{dx^2} = \frac{M}{EI} = \frac{ma}{EI} \left(L_b + \frac{L_{pm}}{2} \right), \tag{2-10}$$

and from Eqn. (2-5), the strain occurs at the top (tension) and bottom (compression at polysilicon layer) of the beam surface is

$$\varepsilon_{poly} = \frac{z}{R_c} = \frac{H_b}{2R_c} \,. \tag{2-11}$$

Inserting Eqn. (2-10) to Eqn. (2-11) yields

$$\varepsilon_{poly} = \frac{H_b}{2}\frac{ma}{EI}\left(L_b + \frac{L_{pm}}{2}\right) = \frac{6m}{EW_bH_b^2}\left(L_b + \frac{L_{pm}}{2}\right)a, \quad (2\text{-}12)$$

which compute the complete solution of the relative change of resistance due to acceleration for four bimorph beams. By substituting Eqn. (2-12) into Eqn. (2-1) and Eqn. (2-2) yields

$$\left(\frac{\Delta R}{R}\right)_l = G_{polyl}\frac{1.5m}{EW_bH_b^2}\left(L_b + \frac{L_{pm}}{2}\right)a, \quad (2\text{-}13)$$

$$\left(\frac{\Delta R}{R}\right)_t = G_{polyt}\frac{1.5mv}{EW_bH_b^2}\left(L_b + \frac{L_{pm}}{2}\right)a, \quad (2\text{-}14)$$

$$R = \rho_{poly}\frac{L_{poly}}{W_{poly}t_{poly}}, \quad (2\text{-}15)$$

where R is the resistance of each poly resistor and is calculated to be 1.1 kΩ using Eqn. (2-15). The resonant frequency, f of the sensor is calculated as 1.85 kHz using the equation given by

$$f = \frac{1}{2\pi}\sqrt{\frac{k}{m}}, \quad (2\text{-}16)$$

in which k is the stiffness coefficient of the bimorph beam calculated to be 14.21 Nm^{-1} and is defined as

$$k = \frac{EW_bH_b^3}{4L_b^3}. \quad (2\text{-}17)$$

Even though from theoretical calculation, the stiffness coefficient is found to be very high, but the inclusion of large and thick proof mass will reduce the stiffness of the sensor and hence reduce the resonant frequency of the device.

PUSAT SUMBER MAKLUMAT UNIVERSITI TEKNOLOGI PETRONAS

2.1.1 Sensor Self Heating Effect

Polysilicon resistor is a type of resistor whose resistance varies with temperature. When a current flows through a polysilicon resistor, it will generate heat which will raise the temperature of the material, which subsequently varies the resistance of the polysilicon resistor. This phenomenon is known as the self heating effect. The resistance change due to self heating effect is considered as an offset to the change of resistance due to acceleration. The joule heating that occurs when a current flows in a resistor can be represented as the lumped-element thermal circuit as shown in Fig. 2.3 [51].

In Fig. 2.3, the electric circuit consists of a resistor and a voltage source. The thermal circuit consists of three elements: a diamond shape dependent current source that provides the Joule heat power V^2/R, a thermal capacitor C_T, which represents the heat capacity of the resistor, and a thermal resistor R_T that represents the heat conduction from

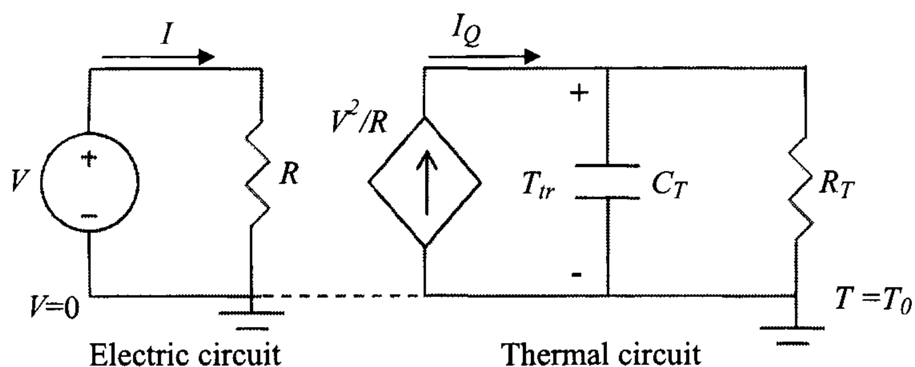

Fig. 2.3. Circuit model for the self heating of a resistor driven by a voltage source.

resistor to a thermal reservoir. $T_0 = T_R$ is the room temperature and is assumed as 25°C or 293 °K. In the thermal circuit, the current variable is denoted as I_Q. The relative change of resistance due to self heating effect in the polysilicon resistor is given by [51]

$$\left(\frac{\Delta R}{R}\right)_{thermal} = \alpha_{poly}\left(T_{ss} - T_R\right) = \alpha_{poly}\Delta T, \tag{2-18}$$

where α_{poly} is the polysilicon temperature coefficient of resistance (TCR) as listed in Table 2.3, while T_{SS} is the steady state temperature due to self heating. The transient response of the temperature, T_{tr} is derived as

$$T_{tr} = T_R + \frac{R_T V^2}{R_R\left(1 + \frac{\alpha_{poly} R_T V^2}{R_R}\right)}\left(1 - e^{-\left(\frac{1}{R_T C_T}\right)t}\right). \tag{2-19}$$

$R_R = R = 1.1$ kΩ is the resistance of the polysilicon resistor at room temperature and can be calculated using Eqn. (2-15). The heat flux is assumed to travel in series from polysilicon resistors to SiO_2 layer then to metal 3 layers and finally distributed on metal 3 surface on substrate. The thermal resistance, R_T and thermal capacitance, C_T can be calculated using Eqn. (2-20) and Eqn. (2-21). The values used are listed in Table 2.4.

$$R_T = R_{Tpoly} + R_{TSiO2} + R_{TAl} = \frac{H_{poly}}{\kappa_{poly} A_{poly}} + \frac{H_{ox}}{\kappa_{ox} A_{ox}} + \frac{L_{Al}}{\kappa_{Al} W_{Al} H_{Al}}, \tag{2-20}$$

$$\frac{1}{C_T} = \frac{1}{C_{Tpoly}} + \frac{1}{C_{TSiO2}} + \frac{1}{C_{TAl}}. \tag{2-21}$$

Table 2.4

Calculated Values for Thermal Resistances and Capacitances

Symbol	Description	Values
A_{poly}	Area of the Polysilicon resistor	5.93×10^{-11} m^2
A_{ox}	Area of the Polysilicon resistor	1.37×10^{-10} m^2
W_{Al}	Area of the oxide	13.4×10^{-6} m
L_{Al}	Width of the metal	10.2×10^{-6} m
R_{Tpoly}	Thermal resistance of polysilicon layer	233 K/W
R_{TSiO2}	Thermal resistance of silicon dioxide layer	1.2×10^{4} K/W
R_{TAl}	Thermal resistance of aluminum layer	4.6×10^{3} K/W
C_{Tpoly}	Thermal capacitance of polysilicon layer	3.88×10^{-11} J/K
C_{TSiO2}	Thermal capacitance of silicon dioxide layer	3.80×10^{-10} J/K
C_{TAl}	Thermal capacitance of aluminum layer	2.32×10^{-10} J/K
R_T	Total thermal resistance	1.7×10^{4} K/W
C_T	Total thermal capacitance	3.1×10^{-11} J/K

2.1.2 Simulation Results

This section presents the sensor performance analysis through simulation when the external out-of-plane acceleration is applied to the sensor. Results from Matlab and CoventorWare simulation such as the mechanical sensitivity, modal analysis, and heat flow for the thermal capacitance estimation due to self heating of the sensor are included and discussed.

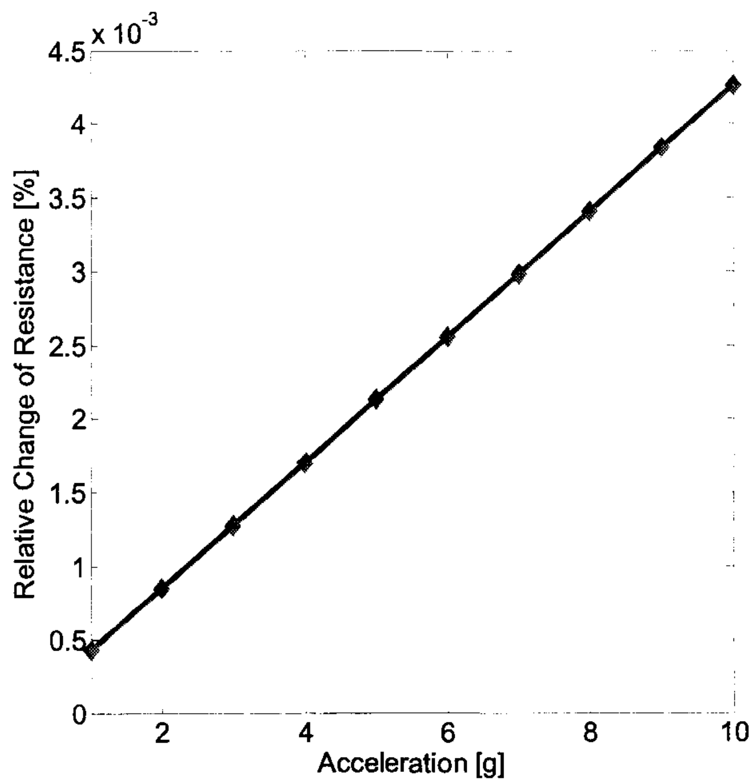

Fig. 2.4. Piezoresistance change in longitudinal direction as a function of out-of-plane acceleration.

Using Eqn. (2-13) and Eqn. (2-14), the longitudinal and transverse relative change of resistance with acceleration from 1g to 10g are estimated and the results obtained from Matlab simulation are shown in Fig. 2.4 and Fig. 2.5. The calculation results show that the longitudinal relative change of the piezoresistance is $+4.26 \times 10^{-4}$ %/g or +4.6 mΩ/g, while the transverse relative change of resistance of the piezoresistance is -0.43×10^{-4} %/g or -0.46 mΩ/g.

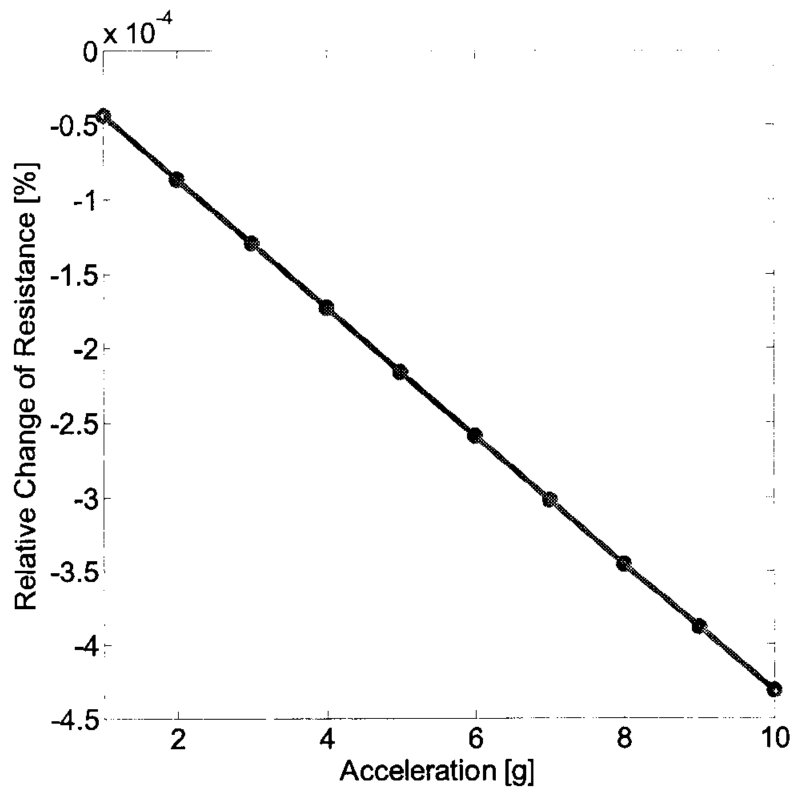

Fig. 2.5. Piezoresistance change in transverse direction as a function of out-of-plane acceleration.

CoventorWare, a comprehensive finite element analysis (FEA) tools dedicated for MEMS design and simulation [52], is used to validate the relative resistance change of the piezo resistors design. From CoventorWare simulation as shown in Fig. 2.6, it is found that the relative piezoresistance change in longitudinal direction can be as high as 1.8×10^{-4} %/g or 1.7 mΩ/g slightly lower from the theoretical result. The FEA simulation result is in good agreement with the theoretical calculation as shown in Fig. 2.6.

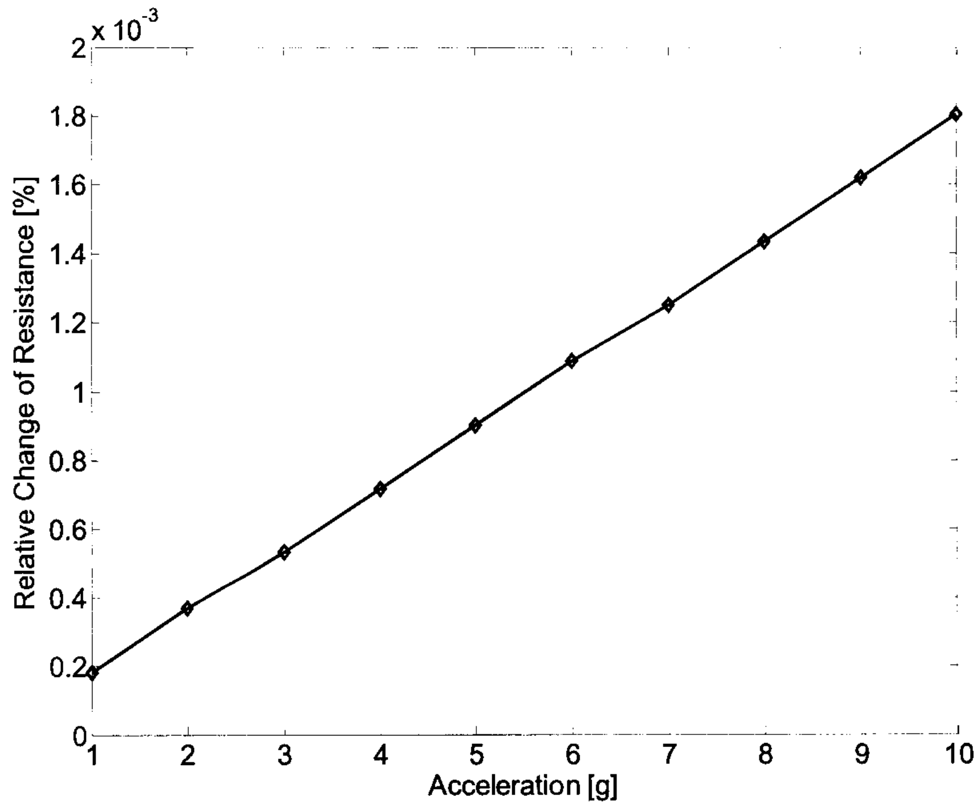

Fig. 2.6. CoventorWare simulation of the piezoresistance change in longitudinal direction as a function of out-of-plane acceleration.

Using similar FEA tool, the resonant frequencies of the sensor are also investigated. The first damped frequency or mode 1 is found to occur at 1.0 kHz with out-of-plane (z-axis) response. The second mode occurs at 3.2 kHz around y-axis while the third mode occurs at 162 kHz along x-axis. From modal simulations, the sensor is found to meet the design requirement, which required the device to safely operate in out-of-plane motion at operating frequencies of 160Hz, which is much lower than the first resonant frequency at 1 kHz. The theoretical result of the first resonant frequency is calculated as 1.85 kHz slightly higher than the result from FEA simulation. CoventorWare modal simulation result is shown in Fig. 2.7.

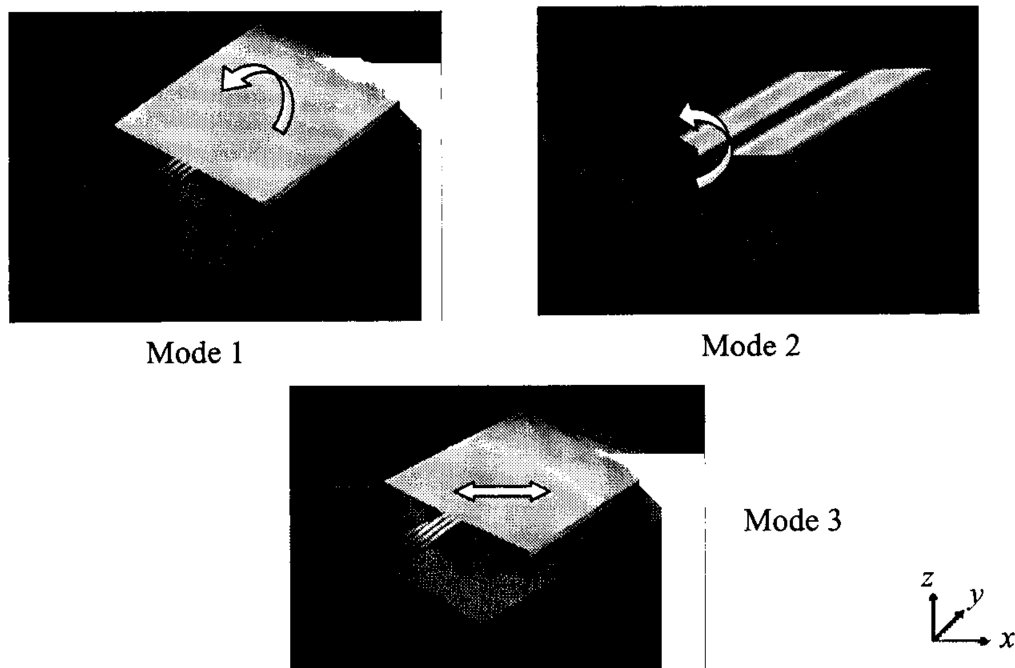

Fig. 2.7. CoventorWare modal simulation to estimate the resonant frequencies of the sensor. (*This figure is presented in color; the black and white reproduction may not be an accurate representation*)

Self heating effect of the polysilicon resistors has also been simulated. The temperature change due to self heating effect of the sensor is found to be ~17 ^{o}K using Eqn. (2-19). The transient response of the temperature when a 1.0 V dc voltage and 1.0 mA of current are applied to the polysilicon resistors is simulated using Matlab as shown in Fig. 2.8, which indicates that the temperature raise in the sensor's beam reaches its steady-state value at ~17 ^{o}K in less than 3ms.

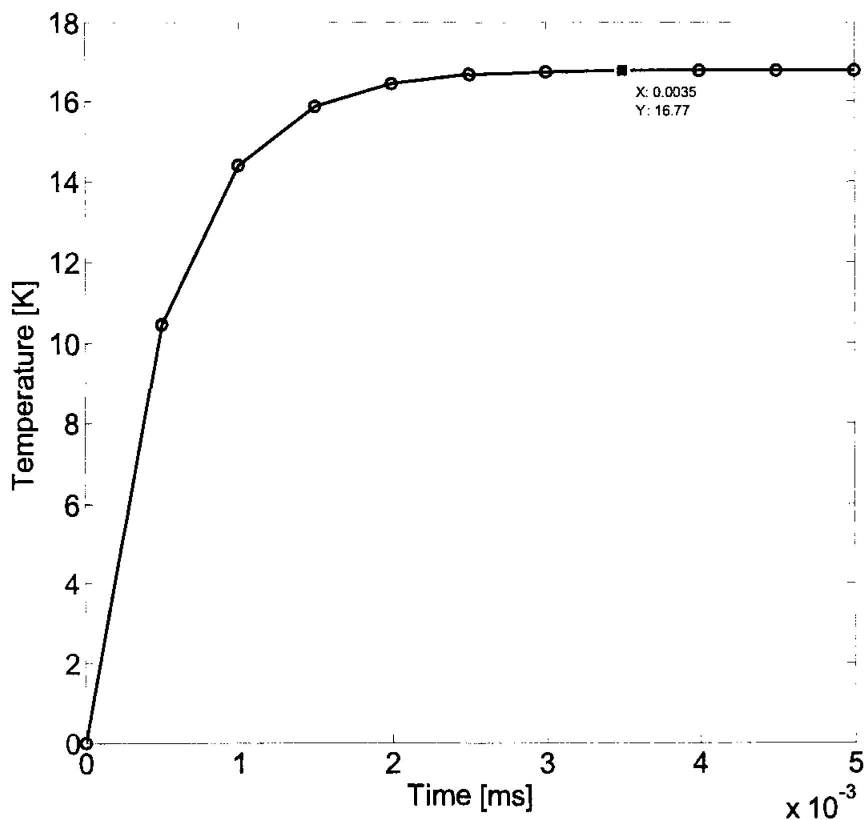

Fig. 2.8. Transient response of the temperature on the bimorph beam simulated using Matlab.

CoventorWare simulation is also been conducted to investigate the flow of the heat flux. Fig. 2.9 shows the CoventorWare simulation result of the heat flux when a current of 1 mA is applied to the polysilicon resistor. From the simulation, the temperature change is found to be ~12 ^{o}K, which is slightly lower than the calculated result at ~17 ^{o}K. The heat flow is observed to be from $Z \rightarrow Y \rightarrow X$ direction as predicted by Eqn. (2-20). This indicates that the FEA simulation results are in good agreement with the theoretical calculation. From the simulation, the relative change of resistance due to the self heating effect is found to be 0.16 %.

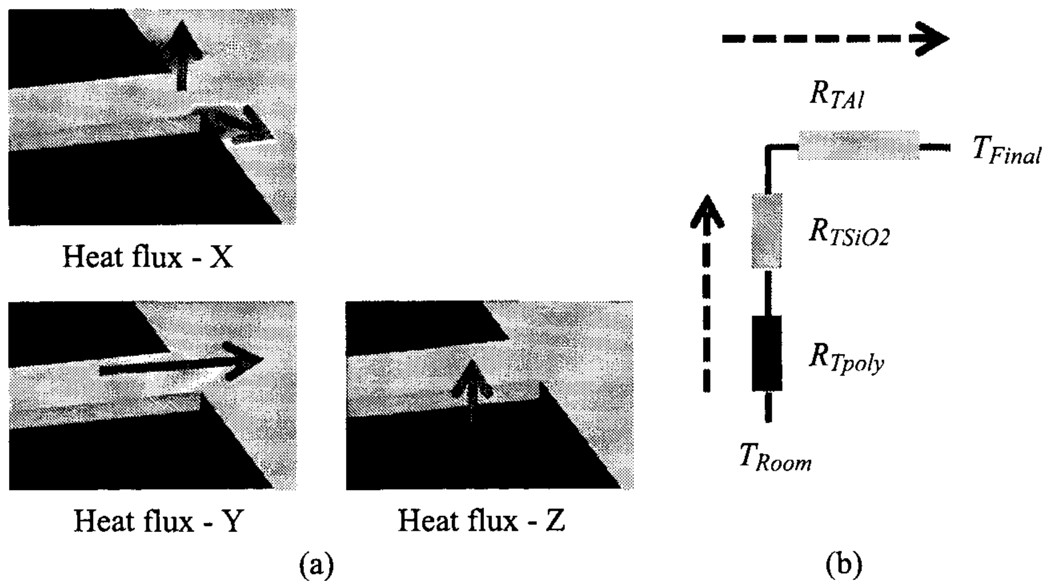

Fig. 2.9. CoventorWare simulation of the (a) heat flux on the sensor bimorph beam and (b) the thermal resistance equivalent circuit. (*This figure is presented in color; the black and white reproduction may not be an accurate representation*).

2.1.3 Conclusion

A high-sensitivity CMOS compatible piezoresistive accelerometer with large proof mass has been successfully designed and simulated. Common issues associated with most of the CMOS-MEMS thin film accelerometer such as structural curling and low sensitivity have been solved by incorporating the SCS as the proof mass. Four bimorph beams employed in the sensor has significantly improved sensor's stability by allowing sorely the out-of-plane motion of the proof mass for larger piezoresistive effect while minimizing in-plane motion. With a nominal sheet resistance, ρ_s of 26.1 Ω/□ from AMI 0.5 μm CMOS technology, the resistivity, ρ_{poly} is calculated to be 9.14×10^{-4} Ω.cm, which contribute to a boron doping concentration of 1.42×10^{19} cm^{-3}. Using the calculated doping concentration, the longitudinal and transverse gauge factors are found to be 40 and -15, respectively. Each poly resistor is calculated to be 1.1 kΩ. The bimorph beam stiffness coefficient, k is calculated as 14.21 Nm^{-1}, and with this stiffness, the resonant frequency is found to be 1.85 kHz from theoretical and 1 kHz from CoventorWare FEA simulator. Theoretical calculation and simulation also conclude that the longitudinal and transverse relative change of the piezoresistance is $+4.26 \times 10^{-4}$ %/g or +4.6 mΩ/g, and -0.43×10^{-4} %/g or -0.46 mΩ/g. Using FEA tool, the longitudinal relative change is found to be $+1.8 \times 10^{-4}$ %/g or +1.7 mΩ/g, which is in agreement with the calculated value. Since the piezoresistance is a temperature dependence material, the effect of self heating shows that temperature is raised ~17 ^{o}K from theoretical calculation and ~12 ^{o}K from the FEA simulation. This has contributed the change of resistance to

0.10 % offset from the theoretical calculation and 0.07 % offset from the FEA simulation.

2.2 Design of a CMOS-MEMS Nano-Newton Force Sensor

Fig. 2.10 shows a 3D model of the force sensor with the arrow on the probe tip representing the out-of-plane force. The sensing element has an overall dimension of approximately 1.7 mm × 1.0 mm with a thickness of approximately 40 μm. The sensor is equipped with a 1100 μm × 50 μm micro probe for out-of-plane force pick-up; and 76 pairs of sensing comb fingers [53].

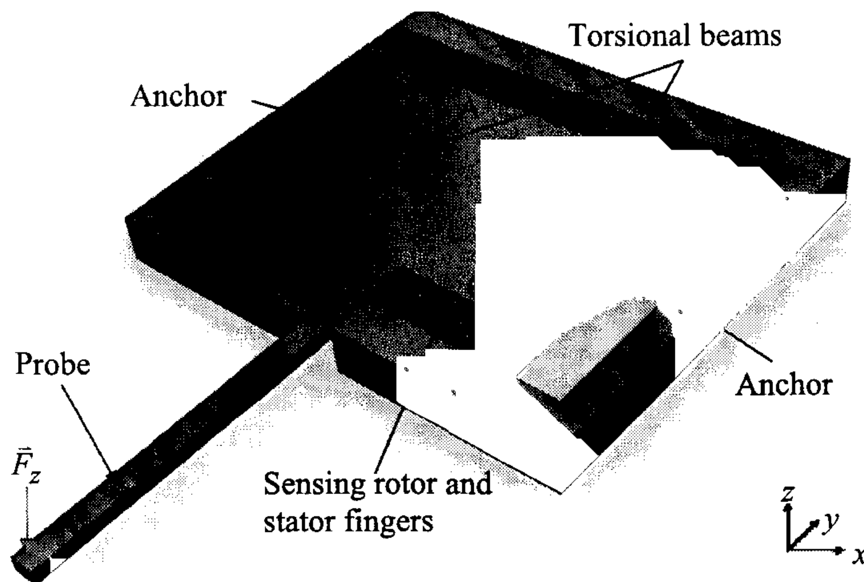

Fig. 2.10. 3D model of the force sensor which illustrates the out-of-plane force, F_z at the probe tip and the comb fingers sections.

From Fig. 2.10, the asymmetric sensor proof mass is suspended to the substrate through two single crystal silicon (SCS) torsional beams. AMI 0.5 μm CMOS technology is used for sensor design and fabrication. Fig. 2.11 shows the CMOS layers used in the device. Note the SCS in the structure is for mechanical support purpose only. The critical technological parameters of AMI 0.5 μm CMOS technology is summarized in Table 2.5 [49]. Other parameters such as the sensor geometric and material properties and their values use for sensor design are listed in Table 2.6. VIAs are used for the connection from Metal 1 to Metal 3 layers, while Metal 1 and Metal 2 layers are used for the signal routing. All three metals are interconnected for the rotor fingers to form one electrode, while Metal 1 and Metal 3 are used as the separate electrodes for the stator fingers.

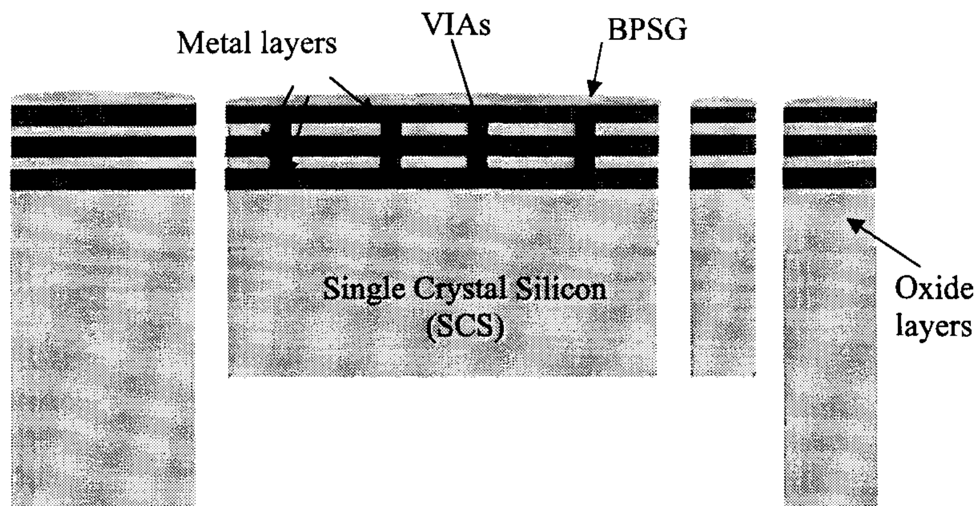

Fig. 2.11. Schematic cross-section view of the sensing element where CMOS thin films are used.

Table 2.5

Typical CMOS Layers Thickness

Layer	Thickness (μm)
Single Crystal Silicon (SCS)	~250
Field Oxide under Poly, H_{ox}	0.4
Field Oxide under Metal 1	0.375
Gate Oxide	0.0135
Via size	0.6 μm x 0.6 μm
Metal, H_M	0.69
Boro-phospho-silicate-glass (BPSG)	0.7

To construct the sensing capacitors and to implement a fully differential sensing, sidewall and fringe capacitances formed by the multiple metal layers is exploited. As shown in Fig. 2.12 in which only one set of sensing capacitors is illustrated, stator comb fingers, which are connected to substrate, use Metal 1 and Metal 3 as capacitor electrodes. In between the stators is a rotor comb finger that is connected to the movable element (torsional beams). The rotor comb finger uses all three metal layers as one electrode. They are connected by the very densely placed interconnected VIAs. Upon the application of a downward force at the probe tip, which is perpendicular to the sensor surface plane, rotor comb fingers in Section B and C will move downward and those in Section A and D will move upward with the same displacement due to the same length of the proof mass on each side of the torsional springs, as shown in Fig. 2.13.

Table 2.6

Geometric and Material Properties

Parameters	Symbol	Value	Unit
Geometric:			
Comb finger length	L_f	100	μm
Gap between comb finger	g	3	μm
Number of comb fingers	N	76	-
Structure thickness	H_{PM}	40	μm
Torsional beam length	L_{TB}	365	μm
Torsional beam width	W_{TB}	4	μm
L × W of the top proof mass to middle of the beam	$L_{TPM} \times W_{TPM}$	924 μm × 250 μm	
L × W of the bottom proof mass to middle of the beam	$L_{BTM} \times W_{BTM}$	700 μm × 250 μm	
Mechanical:			
Aluminum Young's modulus	E_{Al}	65	GPa
SiO_2 Young's modulus	E_{SiO2}	70	GPa
Silicon density	ρ_{Si}	2330	Kg/m^3
Silicon Young's modulus	E_{Si}	165	GPa
Permittivity of the air	E_0	8.85×10^{-12}	F/m
Shear modulus	G	6.7623×10^{10}	Pa

For the sidewall capacitors in Section B, as shown in Fig. 2.12, C_{topB} will decrease and C_{botB} will increase due to the position change of the rotor relative to the stator. To achieve differential sensing and offset cancellation, common-centroid wiring is used to connect the capacitors having the same changing trend together, e.g. C_{topB} and C_{botD}. The initial capacitances of C_{topB} and C_{botB} are different due to the inhomogeneous media surrounding M1 and M2. By connecting C_{topB} and C_{botD} and C_{botC} and C_{topA} together, the same total capacitance with opposite changing trend can be reached.

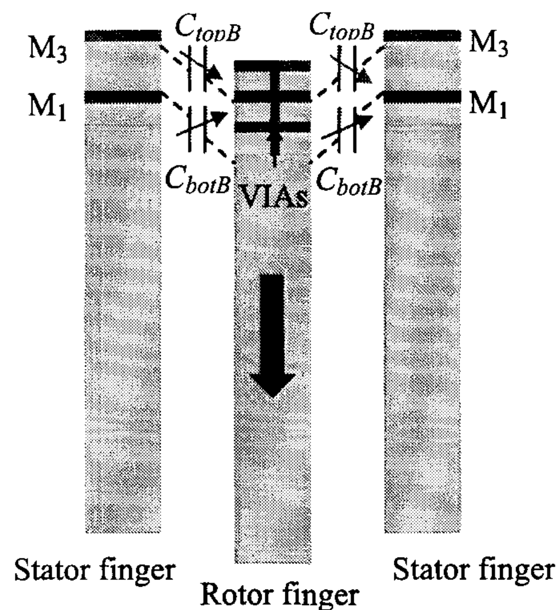

Fig. 2.12. Illustration of the capacitance change when the probe is subject to external force that results in the downward motion of the rotor comb finger.

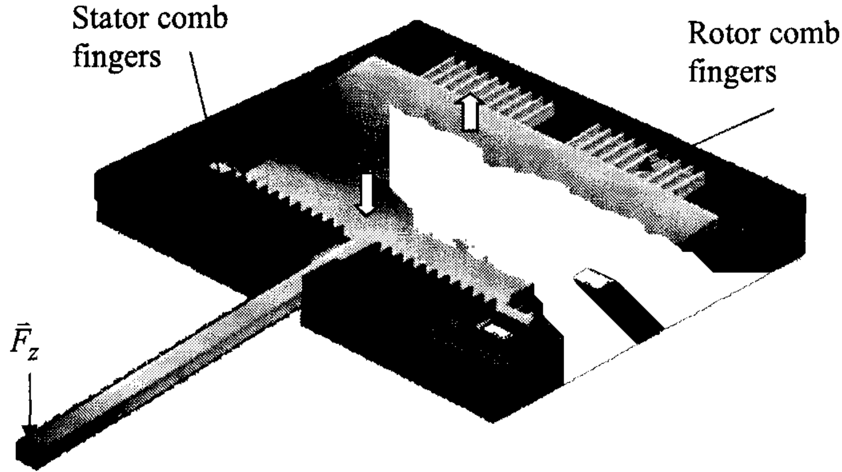

Fig. 2.13. Illustration of the sensing structure motion upon a downward force applied to the probe tip.

Electrical equivalent circuit for the common-centroid configuration of the sensing capacitors is shown in Fig. 2.14. The equivalent circuit in Fig. 2.14 can be further simplified as shown in Fig. 2.15 where $C_{11} = C_{topA} + C_{botC}$, $C_{12} = C_{botA} + C_{topC}$, $C_{21} = C_{botD} + C_{topB}$, and $C_{22} = C_{topD} + C_{botB}$. Referring to Fig. 2.15 and by considering the half-bridge capacitive sensing and ignoring the parasitic effect, the output voltage, V_{o1} is given by [54]

$$V_{o1} = \frac{\tau}{k_\phi}\frac{d}{dz}\left\{\frac{C_{11} - C_{12}}{C_{11} + C_{12}}\right\}, \tag{2-22}$$

where τ is the moment of force applied perpendicular to the axis of the torsional beam and is given by

$$\tau = \left(W_{BTM} + L_{prb}\right)\vec{F}_z. \tag{2-23}$$

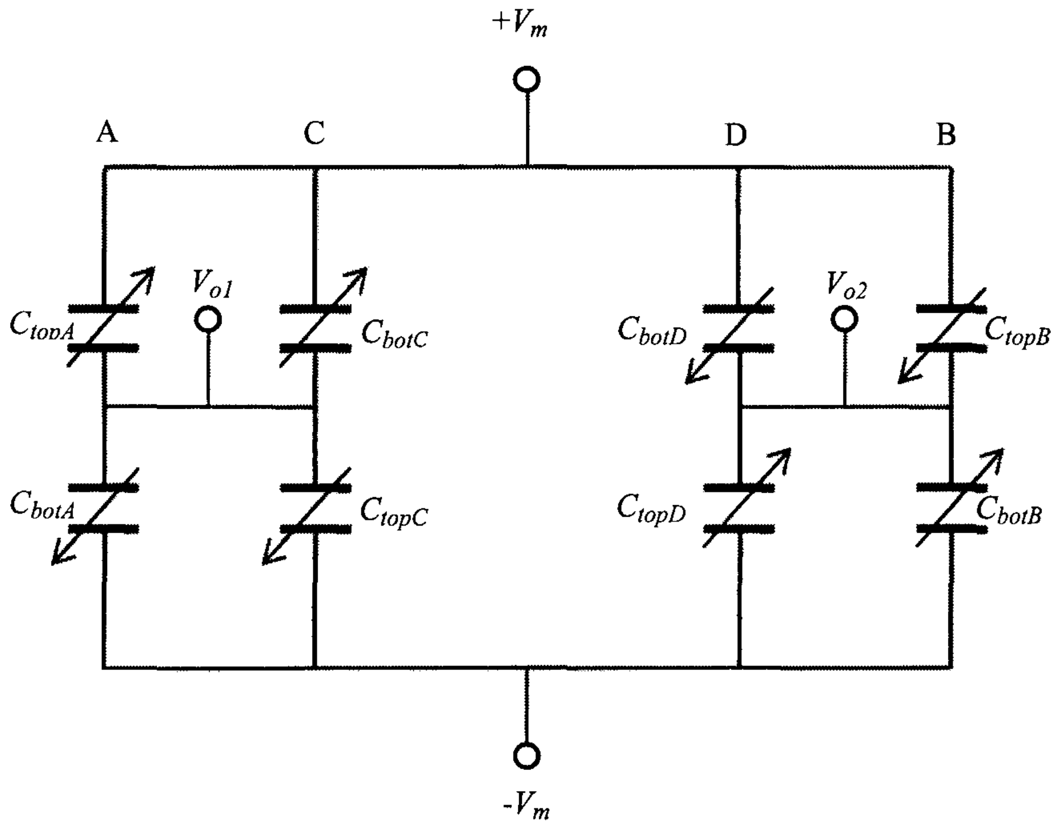

Fig. 2.14. Electrical equivalent circuit for the common-centroid configuration of the sensing capacitors.

The torsional spring constant, k_ϕ in Eqn. (2-22) is found to be 0.002 Nm/rad using the following equation [55]

$$k_\phi = \frac{4c_2 G H_{PM} W_{TB}^3}{L_{TB} W_{BTM}}. \tag{2-24}$$

From Eqn. (2-24), $G = 5.12 \times 10^{10}$ Pa is the shear modulus while c_2 is determined as 0.313 from the aspect ratio of the torsional beam $H_{PM}/W_{TB} = 11.25$ [56].

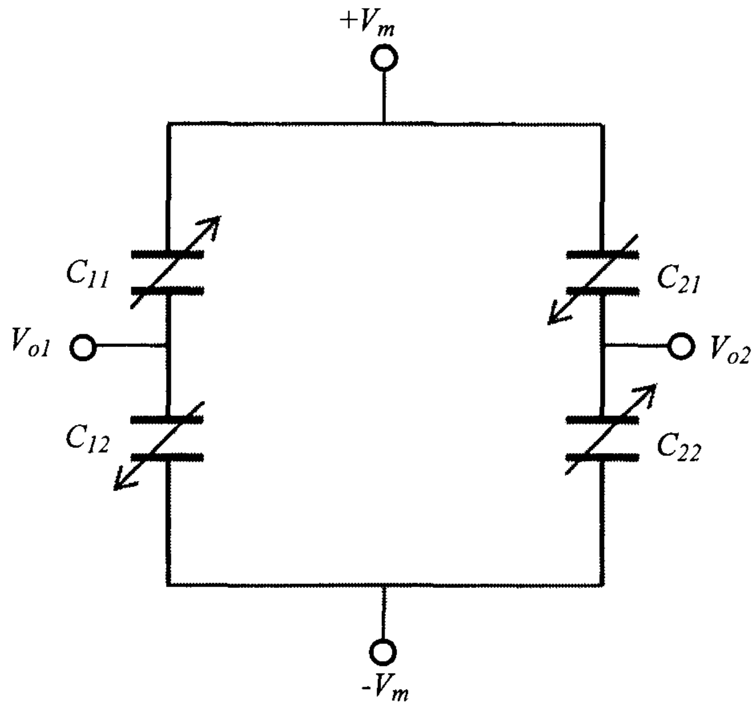

Fig. 2.15. Simplified equivalent circuit of the sensor.

Eqn. (2-25) gives the noise floor of the sensor in N/ √Hz [57]. The noise floor of the sensor determines the minimum force detectable by the sensor. The Brownian noise of the sensor, f_m is produced by the Brownian motion or the random movement of particles suspended in a gas, while f_e is the electrical noise from the interface circuit. The input-referred circuit noise from the interface circuit, V_e is found to be 4 aF/√Hz when referred to MS3110 universal capacitive readout circuit datasheet from Irvine Sensors [58].

$$f_n = \sqrt{f_m^2 + f_e^2} = \sqrt{f_m^2 + \left(\frac{V_e}{S}\right)^2} \quad \text{N/}\sqrt{\text{Hz}}, \qquad (2\text{-}25)$$

$$f_m = \sqrt{4k_B T b}\ , \quad (2\text{-}26)$$

$$b = \frac{\mu A_{eff}}{g}\ . \quad (2\text{-}27)$$

Referring to Eqn. (2-25) to Eqn. (2-27), the Brownian noise of the sensor, f_m is found to be 2.75×10^{-13} N/√Hz. $k_B = 1.38\times10^{-23}$ J/K is the Boltzman's constant and b is the Couette's film damping, which is calculated as 4.69×10^{-6} Kg-s using Eqn. (2-27). From Eqn. (2-27), μ is the viscosity of the air (18.27×10^{-6} Kg/ms) while the effective common area of the sensor, A_{eff} is calculated to be 7.66×10^{-7} m^2.

The sensitivity, S of the sensor is found to be 0.0201 fF/nN prior to amplification. The sensitivity value is obtained through CoventorWare simulation. Theoretical calculation is unable to solve the inhomogeneous media surrounding Metal 1 (M1) and Metal 2 (M2) layers. Due to the complexity of the capacitance arrangement in the sensing structure, the fringing effects are also ignored. Using Eqn. (2-25), the electrical noise, f_e is found to be 5×10^{-16} N/√Hz and the total noise floor of the sensor, f_n is determined as 2.75×10^{-13} N/√Hz. The minimum detectable force, f_{min} by the sensor is therefore calculated to be 8.7 pN. The next section will discuss on the results obtained from the CoventorWare FEA software such as the total capacitance produced by the sensor and the z-displacement of the sensor structure when an external force is applied perpendicular to the sensor surface.

2.2.1 Simulation Results

Nano-Newton force sensor simulation mainly utilizes CoventorWare FEA software to estimate the side wall capacitance change of the comb fingers caused by the external force applied perpendicular to the probe tip. Electro-mechanical simulation result as shown in Fig. 2.16 illustrates that the external force applied perpendicular to the probe from 1 nN to 1mN at the probe tip has resulted in capacitance change with a sensitivity of 0.02 fF/nN. The sensitivity of the sensor is used to determine the electrical noise in Eqn. (2-25).

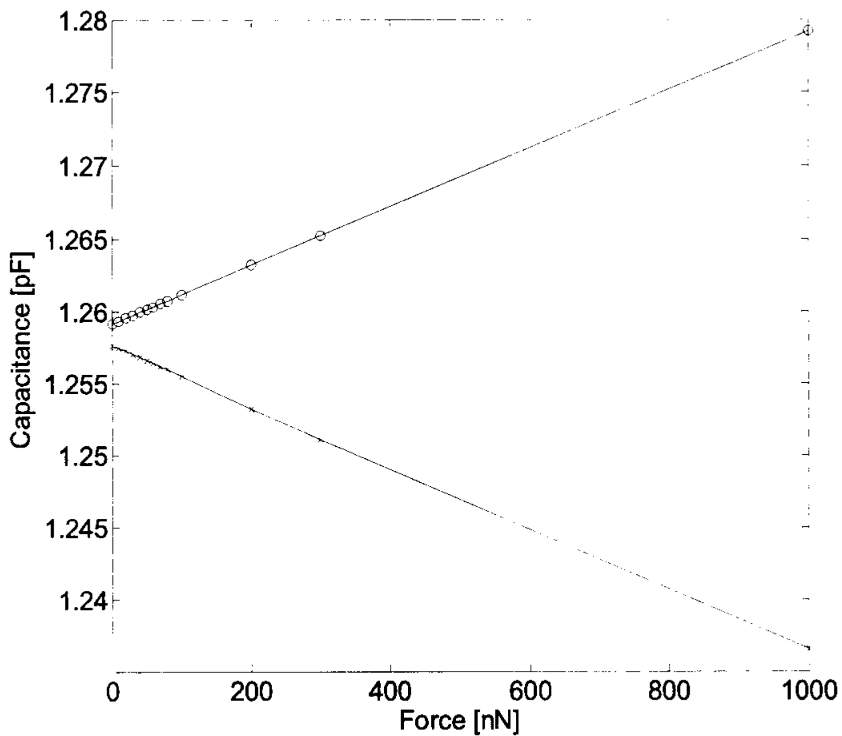

Fig. 2.16. CoventorWare simulation result of capacitance as the function of the out-of-plane force from 1nN to 1 mN.

From the simulation results, a linear response for both the displacement and capacitance change are observed as shown in Fig. 2.16 and Fig. 2.17. External force of 1 mN has resulted in 0.527 μm in z-displacement at sensing finger end and a capacitance change of 13.9 fF has been simulated with the same force excitation as shown in Fig. 2.17.

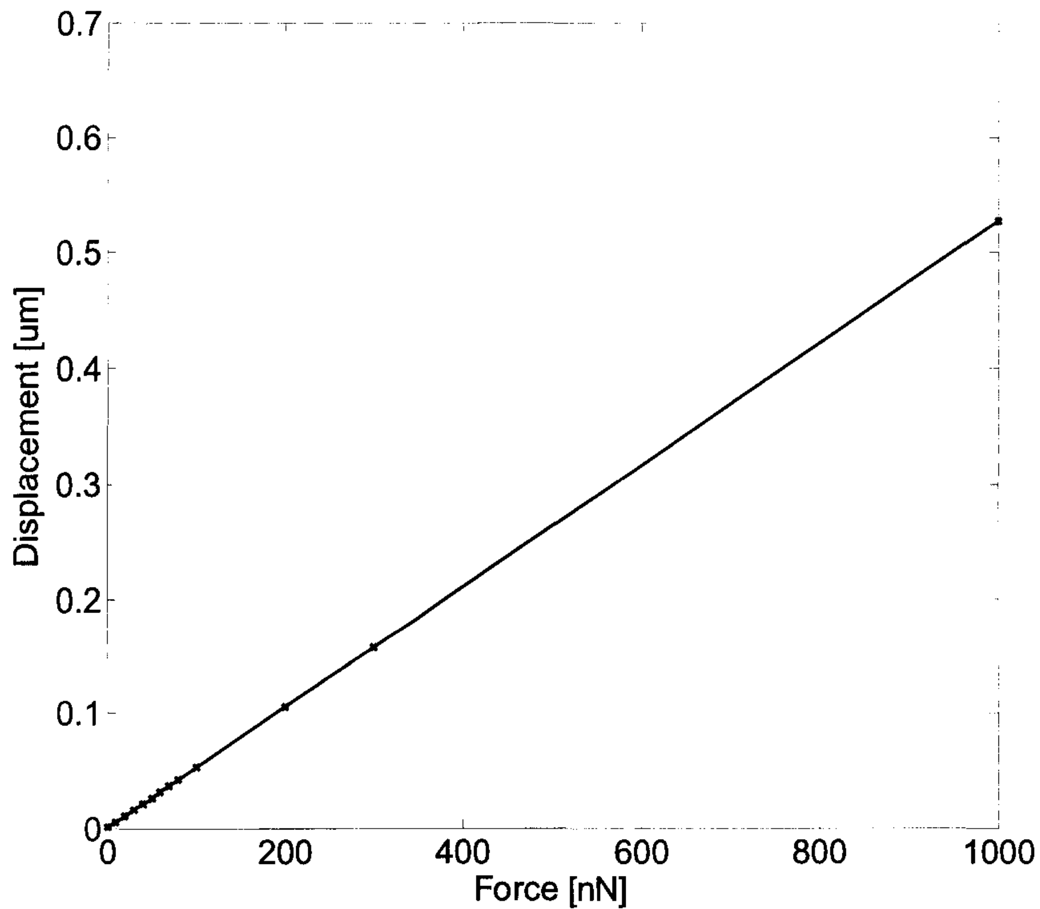

Fig. 2.17. CoventorWare simulation result of displacement as the function of the out-of-plane force from 1 nN to 1 mN.

CoventorWare software is also been used to investigate the resonant frequencies of the force sensor. The modal simulation result can be used to predict the dominant motion of the sensor within the desired operating frequency. The first resonant frequency or mode 1 is found to occur at 1.22 kHz with out-of-plane (z-axis) rotation. The second mode occurs at 2.3 kHz, which shows a rotation of the sensor around x-y-axis, while the third resonant occurs at 3 kHz that indicate a motion along the x-axis. From the simulation result, the sensor is found to operate safely in out-of-plane motion at operating frequencies of below the first resonant frequency of 1.22 kHz. CoventorWare modal simulation is illustrated in Fig. 2.18.

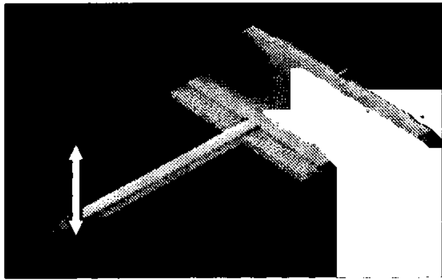

Mode 1 (out-of-plane)

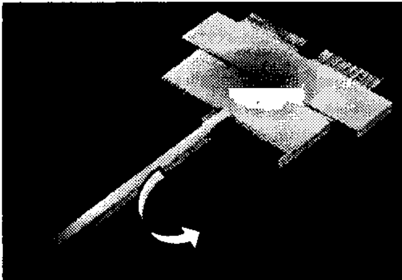

Mode 2 (twisting)

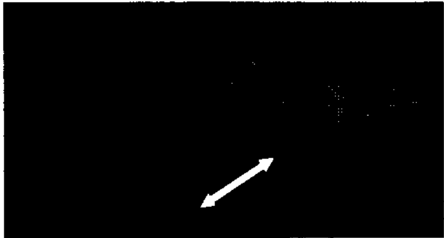

Mode 3 (in-plane, sliding)

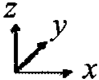

Fig. 2.18. CoventorWare modal simulation to estimate the resonant frequencies of the force sensor. (*This figure is presented in color; the black and white reproduction may not be accurate representation*).

2.2.2 Conclusion

A capacitive CMOS-MEMS force sensor capable of nano-Newton measurement has been successfully designed, and simulated. The sensor produces a sensitivity of 0.02 fF/nN. The stiffness coefficient of the torsional spring is calculated to be 0.002 Nm/rad. The resonant frequency of the sensor structure is found to be 1.6 kHz by theoretical calculation and 1.22 kHz by CoventorWare FEA simulation. The mechanical noise of the system is found to be 2.75×10^{-13} N/√Hz, while the electrical noise is 5.0×10^{-16} N/√Hz. The total noise by considering the electrical input-referred noise of 4 aF/√Hz from the MS3110 universal capacitive readout board is calculated as 2.75×10^{-13} N/√Hz, which result in a minimum detection force of 8.7 pN. The unique out-of-plane sensing mechanism allows sensing of forces applied perpendicular to the sensor plane. The device robustness enabled by the inclusion of SCS as sensor structure allows for reliable deployment in force measurement. The wide force measurement range of nN to mN makes the force sensor suitable for many biomedical applications that operate at frequency of lower than 1 kHz.

CHAPTER THREE

OBSERVER-BASED CONTROLLER DESIGN OF A CMOS-MEMS NANO-NEWTON FORCE SENSOR

This chapter reports the observer-based controller design specifically for the CMOS-MEMS nano-Newton sensor. An actuator system is integrated with the sensor system to provide a controlling action for structure twisting problem. An observer-based controller is used for feedback control and Luenberger observer design. Input-state and input-output linearization techniques are used for the controller linearization, while exact-error linearization method is used to obtain a linear observer canonical form. Luenberger observer is utilized for the states estimation. Section 3.1 discusses the operating principles of the CMOS-MEMS nano-Newton force sensor followed by the description on the problem existed with the current force sensor and the requirement of an integrated actuator system. Section 3.2 explains the mass-spring-damper model that represents the actuator system and the parameters used in the system equation of motion. A state-space representation of the actuator system is used for conveniences. Section 3.3 elaborates the input-states followed by the second feedback linearization techniques known as the input-output linearization methods for comparison purposes. Section 3.4 explains the nonlinear observer design using exact error linearization techniques while Section 3.5 elaborates the observer-based controller design. Section 3.6 presents the simulation results of the observer-based controller system. Finally Section 3.7 concludes and discusses the results obtained from the observer-based controller simulation.

3.1 Sensor Actuator Design

A 3D model of the force sensor system that include the sensing and actuating elements is illustrated Fig. 3.1. The structure has the overall dimension of approximately 1.7 mm × 1.0 mm with the thickness of approximately 40 μm. Single crystal silicon (SCS) is included underneath the CMOS stacks consisting of multiple layers of silicon dioxide (SiO_2), polysilicon, and aluminum (Al) for robust device structures. In the actuator comb drives, SCS is also used as electrode material. A micro probe with a dimension of 1100 μm × 50 μm is attached to the proof mass for force pick-up when an external force is applied to the probe tip perpendicular to the sensor surface. The displacement between the rotor (movable structure) and stator (fixed structure) comb drives is converted into capacitance change, which is processed by the integrated or external circuitry.

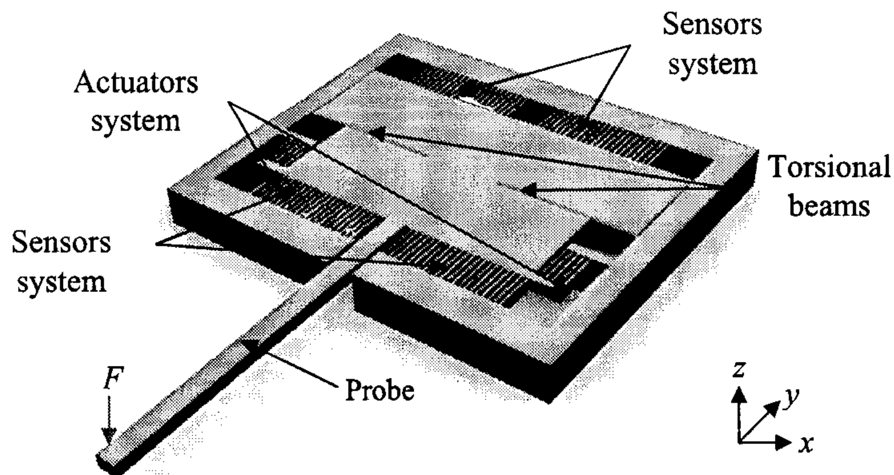

Fig. 3.1. 3D model of the CMOS-MEMS nano-Newton force sensor.

For the sensor element, sidewall and fringe capacitance formed between metal layers on neighboring rotor and stator comb drives are exploited for out-of-plane displacement and force sensing. The structures are anchored to the substrate using a pair of thin SCS torsional beam of dimension 365 μm × 4 μm. In a normal operation, external force perpendicular to the probe tip induces a tilting moment or torque about the torsional beam as shown in Fig. 3.2. Fig. 3.3 illustrates the rotor finger motion due to the external force using one set of the sensing comb finger. This motion results in the change of common area between the stator and rotor fingers, which contributes to the opposite change of the sidewall capacitances, C_{top} and C_{bot}. The output voltage from the sidewall capacitance change is given in [53]. The details of the sensor geometry and materials are listed in [53].

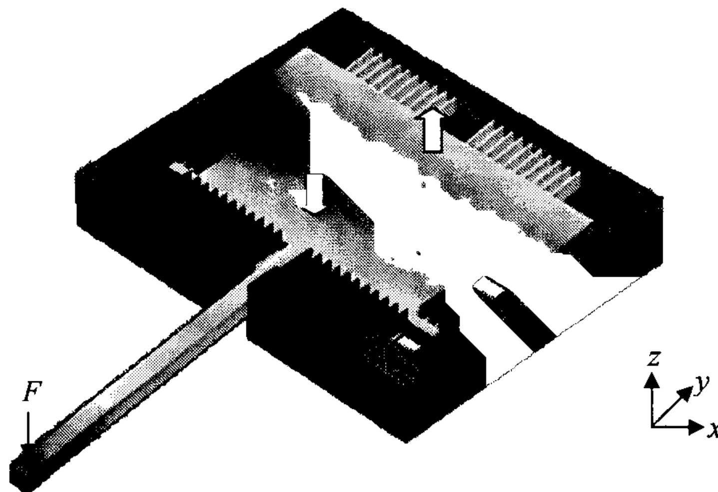

Fig. 3.2. Tilting motion due to force perpendicular to the probe tip.

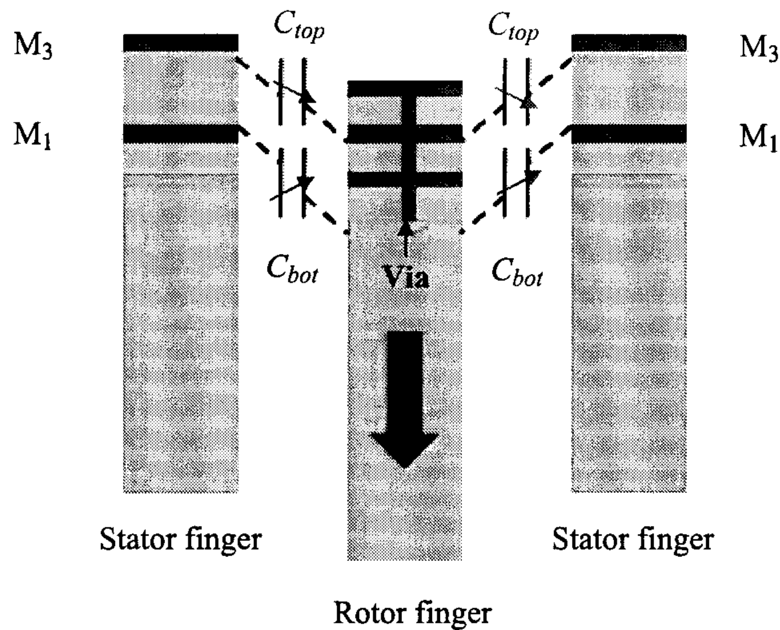

Fig. 3.3. Illustration of the capacitance change of the sensor when the probe tip is subjected to an external force which results in the downward motion of the rotor finger.

Under certain circumstances, the sensor may unexpectedly experience a twist in the *x-y* plane due to undesired in-plane excitations as shown in Fig. 3.4. These forces drive the sensor's rotor fingers toward its neighboring stator fingers, which result in non-uniform sensing gap between them. As a result, measurement errors occur. The twisting motions may also result in crashing between both fingers when the gap is less than 1/3 of the default gap of 3 μm due to the electrostatic pull-in effect.To limit the undesired in-plane twisting mode of the sensor, two sets of the actuators system each consisting of a 4-pair comb finger with a dimension of 100 μm × 5 μm are attached to both sides of the structure as illustrated earlier in Fig. 3.1. These actuators operate independently. When

the driving voltage is applied, they generate electrostatic force to counter the twisting motion; one set in the clockwise direction, and the other set in the anti-clockwise direction. For each actuator, the displacement change, denoted as *p(t)*, of a rotor finger under the twisting in-plane motion is displayed in Fig. 3.5 [59].

The relationship between the instant capacitance change C_{right} and the displacement change *p(t)* is given by

$$C_{right} = \frac{\varepsilon A_a}{p}, \tag{3-1}$$

where ε is the permittivity of the air, and A_a represents the effective area of the neighboring actuator fingers. Time-division sensing and actuating topology is used for force feedback.

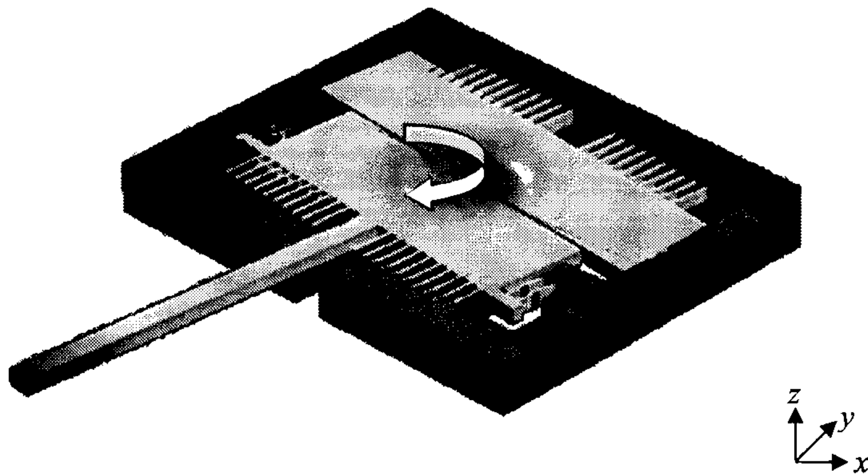

Fig. 3.4. Undesired in-plane twisting motion.

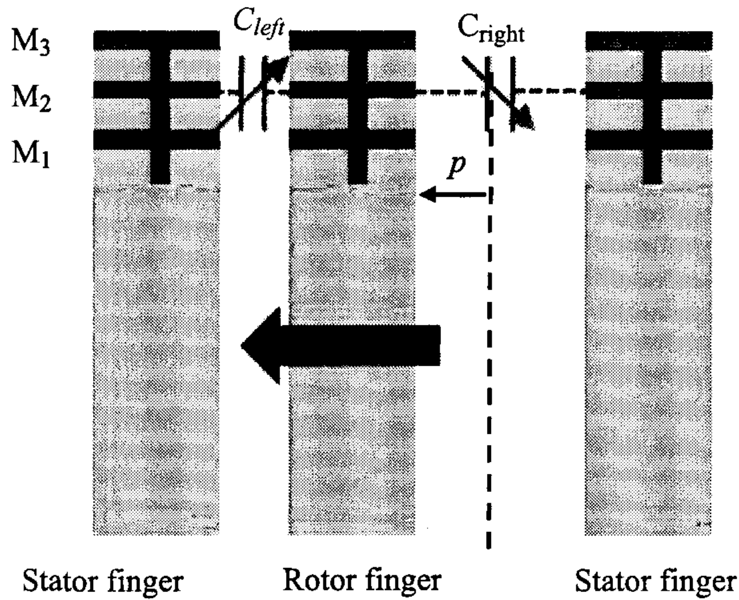

Fig. 3.5. Illustration of the actuator rotor finger lateral motion toward the stator finger due to twisting in-plane force.

In the sensing cycle, the position of the rotor fingers of the feedback comb drives will be determined by sampling the capacitance $C_{right}(t)$. The measured displacement *p(t)* will also reflect the position of the proof mass and thus the probe position. In the actuating cycle, the applied control voltage *V(t)*, will result in electrostatic force, denoted as $F(t)$, that stabilizes the rotor finger according to

$$F = \frac{C_{right}}{2p} V^2, \tag{3-2}$$

where the control voltage *V(t)* is determined by the nonlinear observer-based controller to be developed in the sequel. The development of this work focuses on the controller and observer design. Time-multiplexing system and sampling process will not be addressed.

3.2 Actuator Model

A CMOS-MEMS nano-Newton actuator system can be approximated as a second order mass-spring-damper system. The mass-spring-damper equivalent diagram for a pair of actuator finger system is presented in Fig. 3.6. The lump-parameter model of the system is given by

$$M_a\ddot{p}(t)+b_a\dot{p}(t)+k_a p(t)=F(p,t) \tag{3-3}$$

where $p(t)$ is the displacement of a rotor finger reference to a stator finger, and $F(t)$ is the electrostatic force to counter the twisting motion. The parameters and their values used in Eqn. (3-3) are presented in Table 3.1. The spring stiffness coefficient, k_a of the two beams in parallel is given by [51]

$$k_a=\frac{EhW_{TB}^3}{2L_{TB}^3}, \tag{3-4}$$

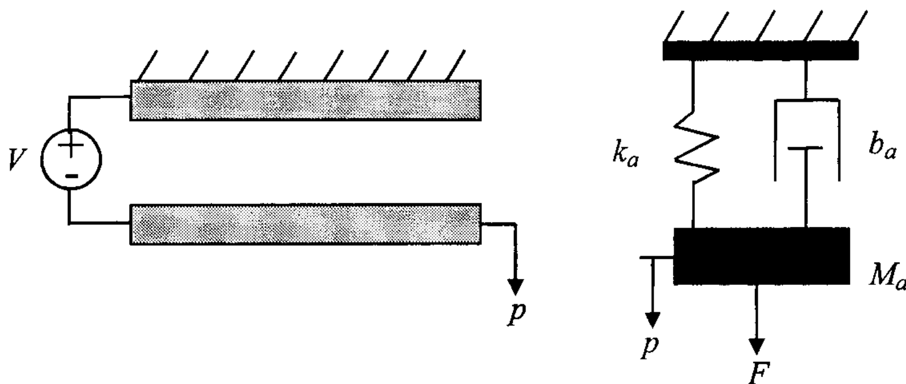

Fig. 3.6. Equivalent diagram for a pair of actuator finger.

Table 3.1

Actuator Parameters and Constants

Symbol	Description	Value
A_a	Finger sensing area	3.567×10^{-9} m^2
N_a	Number of fingers	8
M_a	Proof mass weight	5.91×10^{-10} kg
k_a	Spring stiffness	3.87 N/m
b_a	Squeeze damping coefficient	8.898×10^{-8} Ns
h	Thickness of the structure	40 μm
E	Silicon Young' s modulus	165 GPa
μ	Viscosity of the air	18.27×10^{-6} Pas
W_{TB}	Width of the beam	4 μm
L_{TB}	Length of the beam	365 μm
W_f	Width of the finger	4 μm

and the squeeze film damping between the fingers and substrate , b_a is

$$b_a = \frac{7.2 N_a \mu h W_f^3}{g^3}. \tag{3-5}$$

Let $x_1(t) = p(t)$ and $x_2(t) = \dot{p}(t)$ be the displacement and the velocity of a rotor finger, respectively. Define the control input as the square of the applied voltage, $u(t) \triangleq V^2(t)$, and choose the rotor finger displacement as the output measurement. Using Eqn. (3-1) to Eqn. (3-5), the model in Eqn. (3-3) can be written in state-space form as

$$x_1 \triangleq p, \tag{3-6}$$

$$x_2 \triangleq \dot{x}_1 = \dot{p}\,, \tag{3-7}$$

$$\dot{x}_2 = \ddot{p} = -\frac{k_a}{M_a}x_1 - \frac{b_a}{M_a}x_2 + \frac{1}{2}\frac{\varepsilon A_a}{x_1^2}V^2\,, \tag{3-8}$$

$$\triangleq -\frac{k_a}{M_a}x_1 - \frac{b_a}{M_a}x_2 + \frac{1}{2}\frac{\varepsilon A_a}{x_1^2}u\,. \tag{3-9}$$

Eqn. (3-6) to Eqn. (3-9) can be expressed in a more compact form as

$$\begin{bmatrix}\dot{x}_1\\ \dot{x}_2\end{bmatrix} = \underbrace{\begin{bmatrix} x_2 \\ -\frac{k_a}{M_a}x_1 - \frac{b_a}{M_a}x_2\end{bmatrix}}_{f(x)} + \underbrace{\begin{bmatrix} 0 \\ \frac{1}{2}\frac{\varepsilon A_a}{M_a x_1^2}\end{bmatrix}}_{g(x)} u\,,$$

$$\triangleq f(x) + g(x)u\,, \tag{3-10}$$

with the output measurement given by

$$y = p = h(x) = x_1\,. \tag{3-11}$$

It is seen that the term g(x), the coefficient of *u(t)* in Eqn. (3-10), is nonlinear, although the system matrix and the output matrix are in a linear form. Since the overall system is nonlinear, the well known linear control theory cannot be applied directly. In this thesis, the use of the nonlinear state-feedback linearization technique to solve the nonlinear control problem will be chosen. It is well-known in control theory that most state-feedback controllers require the information of all the state variables for feedback implementation for all $t \le 0$. In our case, we know the values of the displacement $x_1(t)$ from the capacitance measurement in Eqn. (3-1). However, the value of the velocity $x_2(t)$ is not measured and is unknown. In order to estimate the unknown state $x_2(t)$, we may differentiate $x_1(t)$ to obtain $x_2(t) = \dot{x}_1(t)$. But it is well known that time

differentiation creates noise and is not desirable. Therefore, an observer can be used to estimate $x_2(t)$. The linearized linear equation in the z-domain can then be used to design a full-order or reduced-order observer to generate the desired estimate utilizing the celebrated Luenberger observer theory [60, 64].

From the discussions above, we have to solve the following two problems:

- Controller design using the nonlinear state-feedback linearization technique;
- Design of observer-based control system.

3.3 Feedback Linearization of the Nonlinear Actuator System - Controller Design

This section discusses two feedback linearization techniques, namely the input-state and input-output linearization techniques. A linearized system is required prior to actuator controller design. Two linearization methods have been chosen for a comparison purpose [63].

3.3.1 Input-State Linearization

The objective of the input-state linearization is to linearize the mapping from the input u to the state x. Once linearized, numerous linear control methods, such as pole placement and Linear Quadratic Regulator (LQR), can be used to design a controller for the resulting linear system. A nonlinear system such as presented in Eqn. (3-10) is said to be input-state linearizable if and only if it meets the controllability and involutivity conditions [61]. If the nonlinear system is input-state linearizable, then a transformation (diffeomorphism) exists between the x-coordinates in the nonlinear system and the z-coordinates in the linear system. The input-state linearization process for the actuator system presented in Section 3.2 is summarized in the following steps:

Step 1: (Controllability and Involutivity tests)

Controllability and involutivity tests will determine whether the system presented in Eqn. (3-10) is input-state linearizable.

Recall that an nth-order linear time invariant (LTI) system $\dot{x}(t) = Ax(t) + Bu(t)$ is controllable if and only if

$$Rank\begin{bmatrix} B & AB & A^2B & \cdots & A^{n-1}B \end{bmatrix} = n,$$

For a nonlinear system to be controllable, it must also satisfy a controllability condition. For the second-order nonlinear actuator system described by Eqn. (3-10) and Eqn. (3-11), the rank of its controllability matrix must be equal to $n = 2$. As defined in [61], the rank of the controllability matrix for the actuator system can be calculated as follows:

$$rank\begin{bmatrix} g(x) & ad_f^1 g(x) \end{bmatrix} = \begin{bmatrix} g(x) & [f,g] \end{bmatrix},$$

where

$$[f,g] = \left[\frac{\partial g}{\partial x} f(x) - \frac{\partial f}{\partial x} g(x)\right],$$

in which $[f,g]$ is the Lie bracket. Hence

$$rank\begin{bmatrix} g(x) & ad_f^1 g(x) \end{bmatrix} = \begin{bmatrix} 0 & -\frac{1}{2}\frac{\varepsilon A_a}{M_a x_1^2} \\ \frac{1}{2}\frac{\varepsilon A_a}{M_a x_1^2} & -\frac{1}{2}\frac{\varepsilon A_a x_2}{M_a x_1^3} + \frac{1}{2}\frac{\varepsilon A_a b_a}{M_a^2 x_1^2} \end{bmatrix} = 2$$

which shows that the system is controllable.

Next, as defined in [61] and [62], for the system in Eqn. (3-10) with $n = 2$, the distribution is said to be involutive if and only if

$$rank\left[g(x)\right] = rank\left[g(x) \quad [g(x), g(x)]\right]. \tag{3-12}$$

Since

$$[g(x), g(x)] = 0,$$

Eqn. (3-12) trivially becomes

$$rank\left[g(x) \quad [g(x), g(x)]\right] = rank\left[g(x)\right],$$

and is involutive. From the controllable and involutive tests, it is found that the nonlinear system described by Eqn. (3-10) is input-state linearizable. Therefore, a transformation (diffeomorphism) $z = T(x)$ exists between the x-coordinates in the nonlinear system and the z-coordinates in the linear system as shown in Step 2 below.

<u>Step 2</u>: (Determine $T_1(x)$ and $z = T(x)$)

The transformation matrix can be obtained by letting

$$T_1(x) = x_1. \tag{3-13}$$

Using Eqn. (3-13), the second component $T_2(x)$ of the transformation matrix is found by

$$T_2(x) = L_f T_1(x) = \frac{\partial T_1}{\partial x} f(x) = \begin{bmatrix} \frac{\partial T_1}{\partial x_1} & \frac{\partial T_1}{\partial x_2} \end{bmatrix} f(x)$$

$$T_2(x) = \begin{bmatrix} 1 & 0 \end{bmatrix} \begin{bmatrix} x_2 \\ -\frac{k_a}{M_a} x_1 - \frac{b_a}{M_a} x_2 \end{bmatrix} = x_2. \tag{3-14}$$

The state transformation which transforms the x-coordinates into the z-coordinates is therefore given by

$$z = T(x) = \begin{bmatrix} T_1(x) \\ T_2(x) \end{bmatrix} = \begin{bmatrix} x_1 \\ x_2 \end{bmatrix}. \tag{3-15}$$

We remark that the transformation given by Eqn. (3-15) is trivial but is not obvious without calculations. For convenience, we prefer to investigate the controller and observer-based control system designs in the z-domain in the sequel. Eqn. (3-15) yields

$$\dot{z}_1 = \dot{x}_1 = x_2 = z_2, \tag{3-16}$$

$$\dot{z}_2 = \dot{x}_2 = \underbrace{-\frac{k_a}{M_a}x_1 - \frac{b_a}{M_a}x_2}_{\alpha(x)} + \underbrace{\frac{1}{2}\frac{\varepsilon A_a}{M_a x_1^2}}_{\beta(x)}u$$

$$\triangleq \alpha(x) + \beta(x)u, \tag{3-17}$$

where

$$\alpha(x) \triangleq -\frac{k_a}{M_a}x_1 - \frac{b_a}{M_a}x_2, \tag{3-18}$$

$$\beta(x) \triangleq \frac{1}{2}\frac{\varepsilon A_a}{M_a x_1^2}. \tag{3-19}$$

Let the control $u(t)$ be defined by

$$u = \beta^{-1}(x)\left[-\alpha(x) + v\right], \tag{3-20}$$

where v(t) is a new *transformed input*. The control law given by Eqn. (3-20) is called the *linearizing feedback control law*, and $\alpha(x)$ is a nonlinearity cancelling factor.

Substituting Eqn. (3-20) into Eqn. (3-17) renders a linear equation

$$\dot{z}_2 = v. \tag{3-21}$$

To complete the Step 1 design, Eqn. (3-16) and Eqn. (3-21) can be combined and expressed in a compact form as

$$\dot{z} = \begin{bmatrix} 0 & 1 \\ 0 & 0 \end{bmatrix} z + \begin{bmatrix} 0 \\ 1 \end{bmatrix} v \triangleq A_c z + B_c v, \tag{3-22}$$

which is a linear system in the z-domain rendered by the linearizing feedback control law of Eqn. (3-20).

Step 3: (Controller design in z-domain)

A regulator control law for the transformed input $v(t)$ in the z-coordinates can be set as

$$v = -Kz(t)$$
$$= -\begin{bmatrix} K_1 & K_2 \end{bmatrix} \begin{bmatrix} x_1 \\ x_2 \end{bmatrix}, \tag{3-23}$$

where K is the controller gain matrix to be determined such that $A_c - B_c K$ is Hurwitz, that is, every eigenvalue of $A_c - B_c K$ has strictly negative real part; the K matrix can be obtained using any convenient design method, such as pole placement and LQR.

Substituting Eqn. (3-23) into Eqn. (3-20) yields the linearizing feedback control law in the x-domain

$$u = \left(\frac{1}{2} \frac{\varepsilon A_a}{M_a x_1^2} \right)^{-1} \left[\frac{k_a}{M_a} x_1 + \frac{b_a}{M_a} x_2 - \begin{pmatrix} K_1 & K_2 \end{pmatrix} \begin{pmatrix} x_1 \\ x_2 \end{pmatrix} \right], \tag{3-24}$$

that will provide a control action to drive the twisting sensor's structure back to its original position. Substituting Eqn. (3-24) into Eqn. (3-10) yields the overall closed-loop nonlinear control system as

$$\begin{bmatrix} \dot{x}_1 \\ \dot{x}_2 \end{bmatrix} = \begin{bmatrix} x_2 \\ -\frac{k_a}{M_a}x_1 - \frac{b_a}{M_a}x_2 \end{bmatrix} + \begin{bmatrix} 0 \\ \frac{1}{2}\frac{\varepsilon A_a}{M_a x_1^2} \end{bmatrix} \left(\frac{1}{2}\frac{\varepsilon A_a}{M_a x_1^2} \right)^{-1} \left[-\begin{bmatrix} K_1 & K_2 \end{bmatrix} \begin{bmatrix} x_1 \\ x_2 \end{bmatrix} + \frac{k_a}{M_a}x_1 + \frac{b_a}{M_a}x_2 \right] \tag{3-25}$$

$$y = x_1 . \tag{3-26}$$

3.3.2 Input-Output Linearization

The objective of input-output linearization is to find the linear mapping from the input u to the output y. The procedure of input-output linearization consists of taking the time derivatives of the output $y(t)$ until the input $u(t)$ appears. A nonlinear system such as presented in Eqn. (3-10) is input-output linearizable if the relative degree, ρ of the system is equal to the order of the system, n. It is well known that, for a fully linearizable system with $\rho = n$, input-output linearization and input-state yields the same results [61].

The relative degree ρ of a nonlinear system is defined as the number of differentiations of the output required to obtain the input-output map. The input-output linearization process for the actuator system presented in Section 3.1 can be summarized as follows:

Taking the time derivative of the output $y(t)$ twice and using Eqn (3-10) yields

$$\dot{y} = \dot{x}_1 = x_2 , \tag{3-27}$$

$$\ddot{y} = \dot{x}_2 = -\frac{k_a}{M_a}x_1 - \frac{b_a}{M_a}x_2 + \frac{1}{2}\frac{\varepsilon A_a}{M_a x_1^2}u . \tag{3-28}$$

Eqn. (3-28) shows that the relative degree is $\rho = n = 2$, and the transformation has the form

$$z = T(x) = \begin{bmatrix} y \\ \dot{y} \end{bmatrix} = \begin{bmatrix} x_1 \\ x_2 \end{bmatrix}, \quad (3\text{-}29)$$

which is identical to Eq. (3-15) as expected. Using the same regulator control law for the transformed input *v(t)* given by Eq. (3-23) and the linearizing feedback control law given by Eqn (3-24), the overall closed-loop nonlinear control system is identical to that described by Eqn. (3-25) and Eqn. (3-26) and will not repeated here.

3.4 Nonlinear Observer Design Using Lie Algebraic Exact Error Linearization

This section addresses the design of two observers [65]:

- Exact Error Linearization Observer or Normal Form Observer;
- Luenberger Observer.

To start, the nano-Newton actuator system given by Eqn. (3-10) and Eqn. (3-11) are repeated in this section and renumbered for convenience as follows:

$$\begin{bmatrix} \dot{x}_1 \\ \dot{x}_2 \end{bmatrix} = \begin{bmatrix} x_2 \\ -\frac{k_a}{M_a} x_1 - \frac{b_a}{M_a} x_2 \end{bmatrix} + \begin{bmatrix} 0 \\ \frac{1}{2} \frac{\varepsilon A_a}{M_a x_1^2} \end{bmatrix} u, \quad (3\text{-}30)$$

and

$$y = p = h(x) = x_1. \quad (3\text{-}31)$$

Exact Error Linearization Observer

Referring to the nonlinear system in (3-30) and (3-31), the problem of designing an exact error linearization observer is to find a diffeomorphism

$$z_o = T_o(x), \; T_o(0) = 0, \quad (3\text{-}32)$$

such that after the coordinate transformation, the new state-space realization has the observer normal form

$$\underbrace{\begin{bmatrix} \dot{z}_{1o} \\ \dot{z}_{2o} \end{bmatrix}}_{\dot{z}_o} = \underbrace{\begin{bmatrix} 0 & 0 \\ 1 & 0 \end{bmatrix}}_{A_o} \underbrace{\begin{bmatrix} z_{1o} \\ z_{2o} \end{bmatrix}}_{z_o} + \underbrace{\begin{bmatrix} -\frac{k_a}{M_a} y + \frac{\varepsilon A_a}{2M_a y^2} u \\ -\frac{b_a}{M_a} y \end{bmatrix}}_{\gamma(y,u)} \tag{3-33}$$

$$y = z_{2o}, \tag{3-34}$$

or in a compact form

$$\dot{z}_o = A_o z_o + \gamma(y,u), \tag{3-35}$$

$$y = \begin{bmatrix} 0 & 1 \end{bmatrix} z_o \triangleq C_o z_o, \tag{3-36}$$

We note that $[A_o, C_o]$ is an observable pair, that is,

$$\operatorname{rank}\begin{bmatrix} C_o^T & A_o^T C_o^T \end{bmatrix} = 2. \tag{3-37}$$

Under the new coordinate system, an observer can be constructed as

$$\dot{\hat{z}}_o = \underbrace{\left(A_o - LC_0\right)}_{A_{ocl}} \hat{z}_o + \gamma(y,u) + Ly, \tag{3-38}$$

where the gain matrix $L = \begin{bmatrix} L_1 & L_2 \end{bmatrix}^T$ is determined such that $A_{ocl} = A_o - LC_0$ is Hurwitz. Defining the estimation error as $\tilde{z}_o \triangleq z_o - \hat{z}_o$, it can be shown through an error analysis that

$$\dot{\tilde{z}}_o = A_{ocl} \tilde{z}_o. \tag{3-39}$$

Since A_{ocl} is Hurwitz, it follows that the estimation error $\tilde{z}_o \to 0$ as $t \to \infty$.

Finally, with the transformation $\mathbf{z}_o = \mathbf{T}_o(\mathbf{x})$, the observer given by (3-38) can be expressed in the original x-coordinates as

$$\dot{\hat{x}} = \left(\frac{\partial T_o(\hat{x})}{\partial \hat{x}}\right)^{-1} \left[A_{ocl}T_o(\hat{x}) + \gamma(y,u) + Ly\right], \tag{3-40}$$

which is required for the implementation of an observer-based control system.

Now, returning to (3-38), the exact error linearization observer problem is solvable for the 2nd-order system described by Eqn. (3-30) and Eqn. (3-31) if and only if [62]

(i) $rank\left(\frac{\partial}{\partial x}\begin{bmatrix} h(x) \\ L_f h(x) \end{bmatrix}\right) = n$,

(ii) the unique vector field solution $\tau(\mathbf{x})$ of

$$\frac{\partial}{\partial x}\begin{bmatrix} h(x) \\ L_f h(x) \end{bmatrix} \tau(x) = \begin{bmatrix} 0 \\ 1 \end{bmatrix},$$

is such that

$$\left[\tau, ad_f^1 \tau\right] = 0.$$

For the nano-Newton force actuator sensor system with $n = 2$, we have, from condition (i),

$$rank\left(\frac{\partial}{\partial x}\begin{bmatrix} h(x) \\ L_f h(x) \end{bmatrix}\right) = rank\left(\frac{\partial}{\partial x}\begin{bmatrix} x_1 \\ x_2 \end{bmatrix}\right) = rank\begin{bmatrix} 1 & 0 \\ 0 & 1 \end{bmatrix} = 2,$$

and from condition (ii),

$$\begin{bmatrix} 0 \\ 1 \end{bmatrix} = \frac{\partial}{\partial x}\begin{bmatrix} h(x) \\ L_f h(x) \end{bmatrix} \tau(x) = \frac{\partial}{\partial x}\begin{bmatrix} x_1 \\ x_2 \end{bmatrix} \tau(x) = \begin{bmatrix} 1 & 0 \\ 0 & 1 \end{bmatrix} \tau(x),$$

which yields

$$\tau(x) = \begin{bmatrix} 0 \\ 1 \end{bmatrix},$$

$$\left[\tau, ad_f^1 \tau\right] = \left[\tau, [f, \tau]\right] = 0.$$

Hence, both conditions (i) and (ii) are satisfied, and we can construct the diffeomorphism by solving the partial differential equation (PDE) [62]:

$$\frac{\partial F}{\partial z_o} = \left[\tau(x) \quad -ad_f \tau(x)\right]_{x=F(z_o)} = \begin{bmatrix} 0 & 1 \\ 1 & -\dfrac{b_a}{m_a} \end{bmatrix}, \tag{3-41}$$

where $F(z_o) \triangleq T_o^{-1}(z_o)$. Note that, in general, it is not an easy task to solve for $\mathbf{F}(\mathbf{z}_o)$ from (3-41), even for a low order system. Fortunately, the right side of (3-41) is a constant matrix and the PDE has a simple solution given by

$$x = F(x) = T_o^{-1}(x) = \begin{bmatrix} z_{o2} \\ z_{o1} - \dfrac{b_a}{M_a} z_{o2} \end{bmatrix}. \tag{3-42}$$

The inverse of (3-42) is given by

$$z_o = T_o(x) = \begin{bmatrix} \dfrac{b_a}{M_a} x_1 + x_2 \\ x_1 \end{bmatrix}. \tag{3-43}$$

Eqn. (3-43) yields

$$\hat{z}_o = T_o(\hat{x}) = \begin{bmatrix} \dfrac{b_a}{M_a} \hat{x}_1 + \hat{x}_2 \\ \hat{x}_1 \end{bmatrix}. \tag{3-44}$$

Finally, Eqn (3-40) becomes

$$\dot{\hat{x}} = \left(\frac{\partial T_o(\hat{x})}{\partial \hat{x}} \right)^{-1} \left[A_{ocl} T_o(\hat{x}) + \gamma(y,u) + Ly \right]. \tag{3-45}$$

This completes the design of the exact error linearization or normal form observer.

Luenberger Observer Design

Consider again the system of Eqn. (3-30) and Eqn. (3-31). Note that $g(x)$ is a function of x_1 where $x_1 = y$ is the known measurement, it can expressed as a known function $g(x) = g(y)$. Since the pair $[A, C]$ is observable, a full-order (2nd-order) Luenberger observer can be constructed readily as

$$\dot{\hat{x}} = (A - LC)\hat{x} + g(y)u + Ly, \tag{3-46}$$

where $L = [L_1 \quad L_2]^T$ is the constant gain matrix to be determined such that $(A - LC)$ is Hurwitz. It may be mentioned that the design of a reduced-order observer or 1st-order observer in this case is also possible, but will not be considered here. A straightforward analysis of the estimation error $\tilde{x} \triangleq x - \hat{x}$ yields

$$\dot{\tilde{x}} = (A - LC)\tilde{x}, \tag{3-47}$$

which shows that the estimation error is asymptotically stable, that is, $\lim_{t \to \infty} \hat{x}(t) \to x(t)$.

This completes the design of a Luenberger for the nano-Newton sensor system. Next section will discuss on the obsever-based controller designs, which will summarize the observer-based design using exact-error linearization and using Luenberger observer approach.

3.5 Observer-Based Controller Designs

This section presents two observer-based controller designs using the exact error linearization and Luenberger observer formulations.

(i) Observer-based controller using the exact error linearization approach

The observer-based control system for the nano-Newton force sensor actuator system is given by, from Eqn. (3-25) and Eqn. (3-45),

$$\dot{x} = f(x) + \frac{g(x)}{g(y)}\left[-\begin{bmatrix} K_1 & K_2 \end{bmatrix} \begin{bmatrix} \hat{x}_1 \\ x_2 \end{bmatrix} + \frac{k_a}{M_a}\hat{x}_1 + \frac{b_a}{M_a}\hat{x}_2 \right] \tag{3-48}$$

$$\dot{\hat{x}} = \left(\frac{\partial T_o(\hat{x})}{\partial \hat{x}} \right)^{-1} \left[A_{ocl} T_o(\hat{x}) + \gamma(y,u) + Ly \right] \tag{3-49}$$

(ii) Observer-based controller using the Luenberger observer approach

The observer-based control system for the nano-Newton force sensor actuator system is given by, from Eqn. (3-25) and Eqn. (3-46),

$$\dot{x} = f(x) + \frac{g(x)}{g(y)}\left[-\begin{bmatrix} K_1 & K_2 \end{bmatrix} \begin{bmatrix} \hat{x}_1 \\ x_2 \end{bmatrix} + \frac{k_a}{M_a}\hat{x}_1 + \frac{b_a}{M_a}\hat{x}_2 \right] \tag{3-50}$$

$$\dot{\hat{x}} = (A - LC)\hat{x} + g(y)u + Ly \tag{3-51}$$

A block diagram with the observer in the feedback path is as shown in Fig. 3.7. Fig. 3.7 illustrates the complete observer-based controller design, which covers the nonlinear system block, the observer system block, and the linearize system controller block.

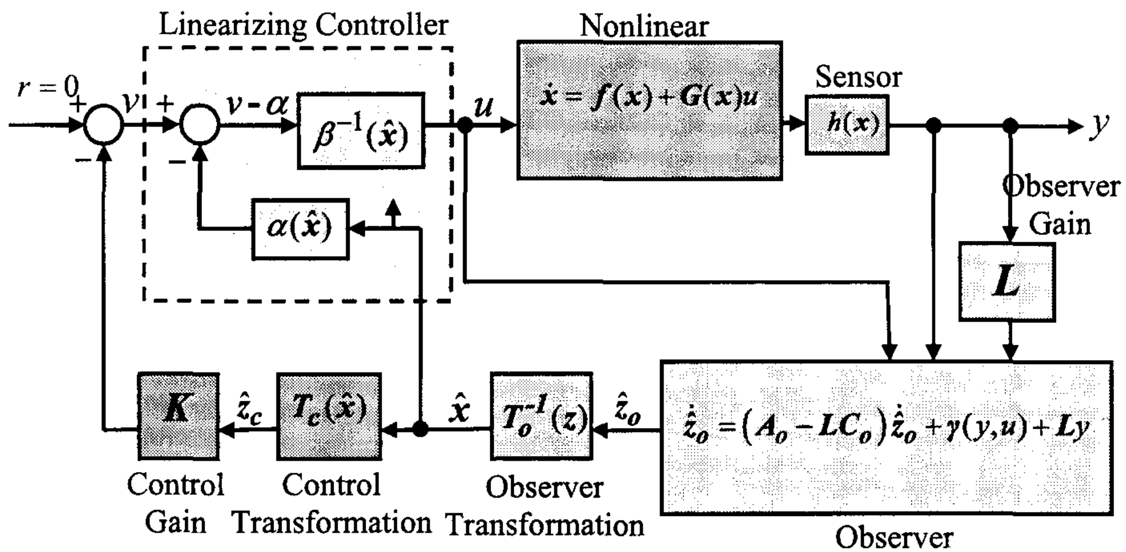

Fig. 3.7. The schematic diagram of a nonlinear observer-based controller system.

3.6 Observer-Based Controller Simulation Results

This section discusses the simulation results of the observer-based controller for the nano-Newton actuator system. A poles placement method is applied to obtain the controller and observer gain matrix, *K* and *L*. Since the device requires a response time of less than 10 ms for the external force excitation of approximately 100 Hz or below, care must be taken when choosing the pole locations such that the transient responses are satisfied with the requirement. By trial and error, it is found that by placing the controller and observer poles at {-370, -420}, and {-480, -530}, respectively, have produced satisfactory performances. The resulting controller and observer gains resulted from the selected poles are summarized in Table 3.2. The simulation result which shows the

performance of the observer-based controller with the displacement initial position of 0.2 μm is shown in Fig. 3.8 and Fig. 3.9.

For simulation purposes, the rotor finger is assumed to start at these initial displacements and the objective of the controller is to pull the rotor finger back to the zero position in less than 10 ms. Fig. 3.8 illustrates the response of the estimated state $\hat{x}_1(t)$ and $\hat{x}_2(t)$ converging to the real states $x_1(t)$ and $x_2(t)$, respectively. The control voltage signal used to regulate the rotor displacement is shown in Fig. 3.8. From Fig. 3.9, it can be seen that the control action takes less 1.5 V in less than 10 ms to drive the rotor displacement back to zero position as desired. To observe the overall performance of the actuator, four different initial displacements of the rotor finger of $x_1(0) = 0.1$ μm, $x_1(0) = 0.4$ μm, $x_1(0) = 0.6$ μm, and $x_1(0) = 0.8$ μm as shown in Fig. 3.10 have been chosen. Overall performance shows that both estimated states converge to the original states in less than 20 ms.

Table 3.2

Resulting Controller and Observer Gains

Controller Gain, K	Observer Gain, L
$K_1 = 1.55 \times 10^5$	$L_1 = 1010$
$K_2 = 790$	$L_2 = 2.54 \times 10^5$

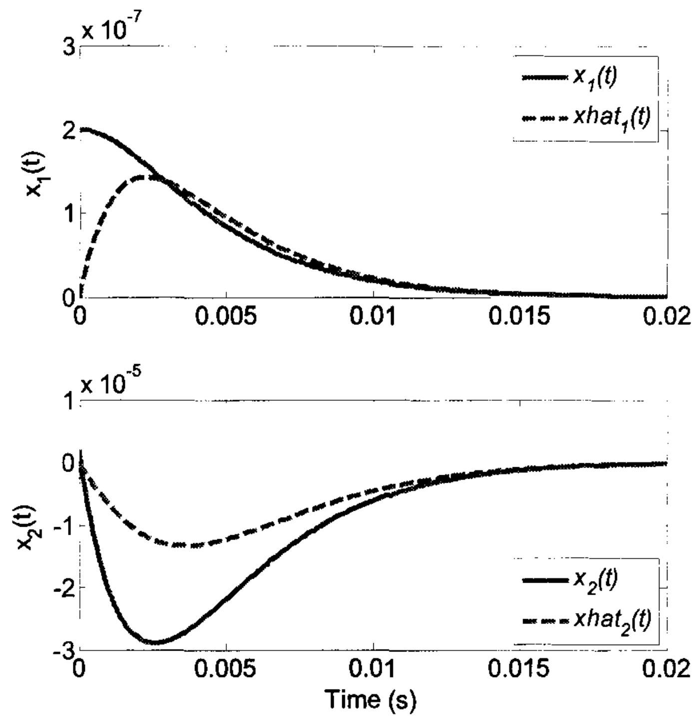

Fig. 3.8. Simulation of the observer-based controller state estimation response with the displacement initial condition of 0.2 μm.

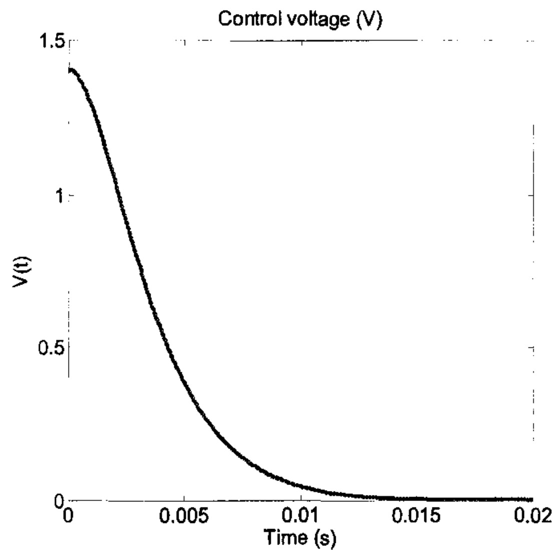

Fig. 3.9. Simulation of the observer-based controller control-input response with the displacement initial condition of 0.2 μm.

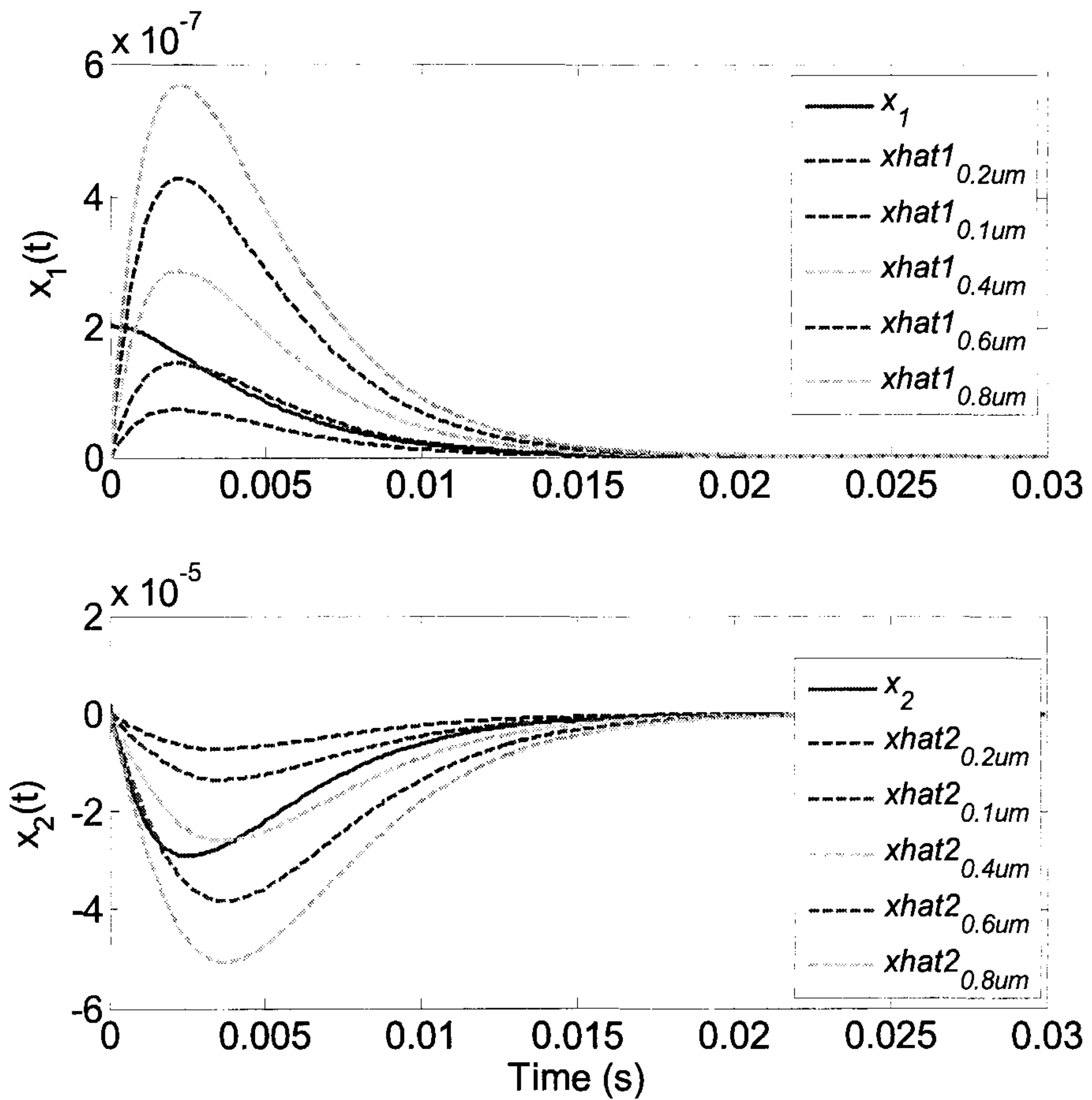

Fig. 3.10. Simulation of the observer-based controller state estimation response with the displacement initial condition of 0.1 μm, 0.2 μm, 0.4 μm, 0.6 μm, and 0.8 μm. (*This figure is presented in color; the black and white reproduction may not be accurate representation*).

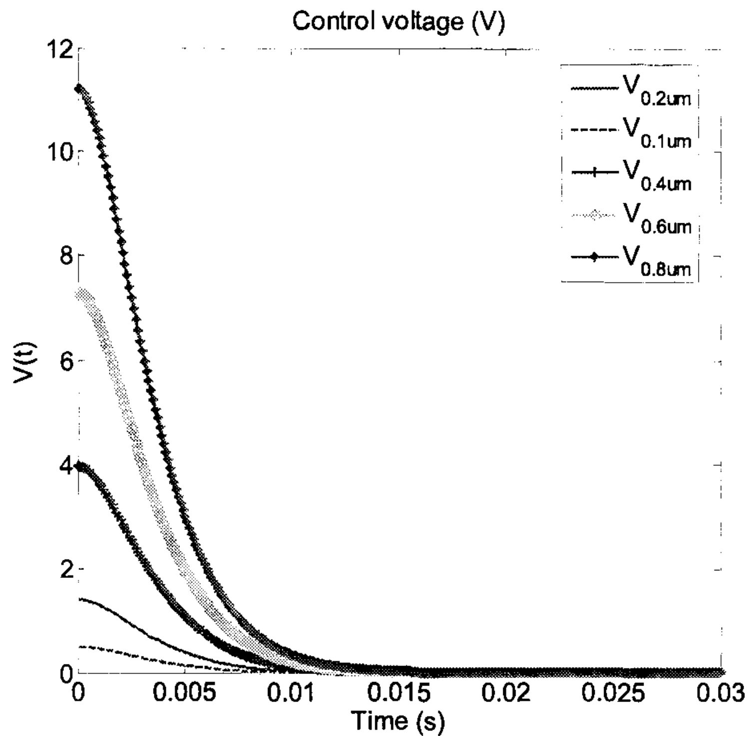

Fig. 3.11. Simulation of the observer-based controller control-input response with the displacement initial condition of 0.1 μm, 0.2 μm, 0.4 μm, 0.6 μm, and 0.8 μm. (*This figure is presented in color; the black and white reproduction may not be accurate representation*).

From Fig. 3.9 and Fig. 3.10, it can be seen that for all the initial displacement used, the estimated states converged nicely and control voltage action in less than 15 ms and 12 V are observed.

3.7 Conclusion

Two observer-based controllers for the nano-Newton actuator system have been designed and simulated. The objective of the actuator system integration within the sensor structure is to resolve sensor structure twisting problem. Two sets of actuator system consists of 4 pairs of comb finger with a dimension of 100 μm x 5 μm are

attached on both sides of the sensor structure. The actuator system is modelled as the second order mass spring damper system with two states, the displacement, x_1 and velocity, x_2 are chosen. Since the actuator is a nonlinear system, prior to the controller design, the system is linearized using the input-state and input-output linearization techniques. Second linearization technique was used for comparison purposed. A nonlinear observer using Lie algebraic exact error linearization method is used for the observer design. An observer is a necessity to estimate the unknown states for state feedback and controller design. By selecting the poles location of {-370, -420} for the controller and {-480, -530} for the observer, system response of approximately 10 ms has been observed, which satisfy the design requirement for the controller to response in less than 10 ms.

CHAPTER FOUR

POST-MICROFABRICATION OF THE CMOS-MEMS SENSORS

This chapter presents the post-CMOS microfabrication processes of the CMOS-MEMS sensors. A customize post-CMOS microfabrication processes have been designed for successful sensors structure release from the substrate. AMI 0.5 μm CMOS technology is used for CMOS fabrication of the sensor through MOSIS. The device layout was designed using Mentor Graphic layout tool. The blue print, which shows the location of the piezoresistive accelerometer, nano-Newton force sensor, electrostatic micromirror, pads, and the test structures are shown in Fig. 4.1. This chapter can be divided into three sections. Section 4.1 and Section 4.2 explain the post-CMOS microfabrication of the piezoresistive accelerometer and nano-Newton force sensor followed by the Section 4.3, which summarizes the post-CMOS microfabrication process and its results. Referring to Fig. 4.1, pad array 1 is used for the connection between the nano-Newton force sensor and piezoresistive accelerometer with the package pad, while pad array 2 is used for the connection between the micromirror with the package pad. Test structure 1, 2, and 3 are used for process monitoring purposes, which was used to estimate SiO_2 etching rate and Metal 3 to Metal 1 distance. Test structures are crucial to avoid over-etching of the CMOS materials. The dummy structures were used to meet AMI 0.5 μm design rules, which require greater than 14 % poly and 30 % metals densities.

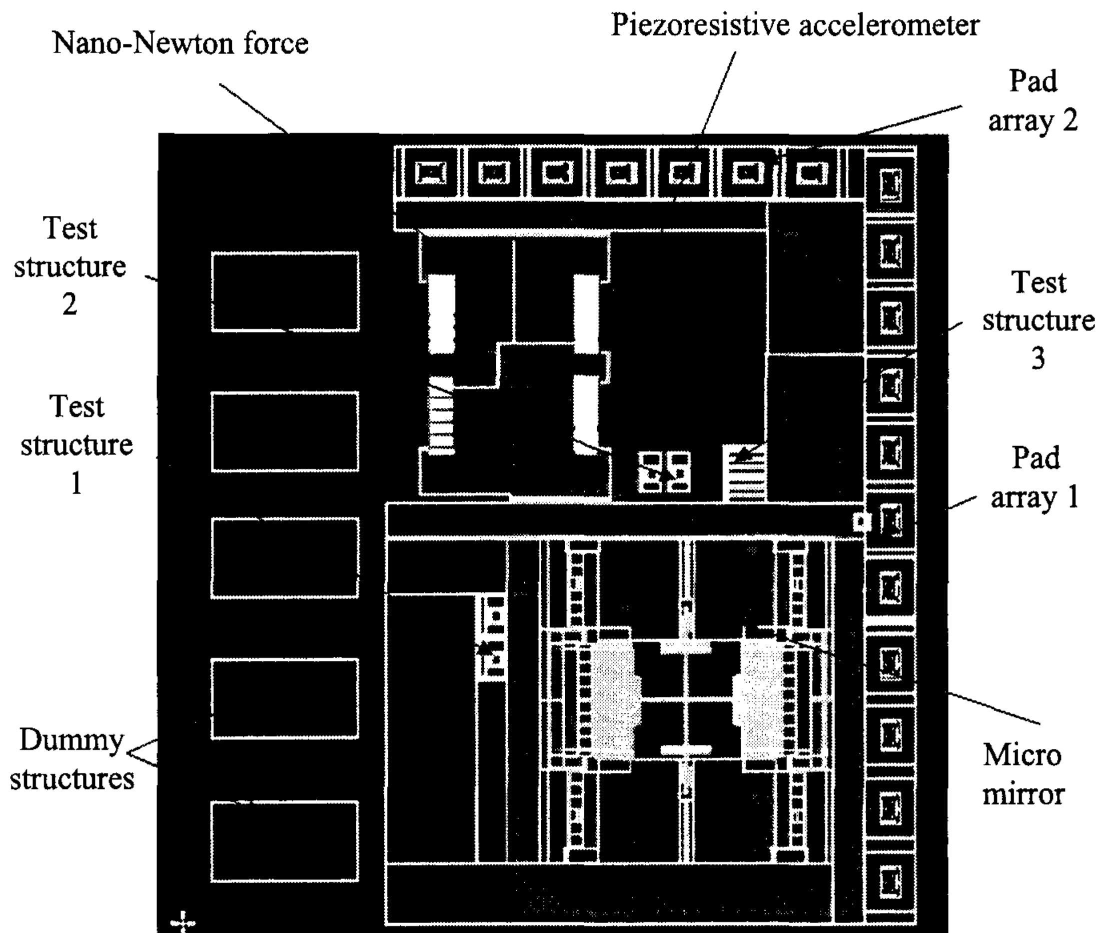

Fig. 4.1. CMOS-MEMS layout showing the location of the sensor drawn using Mentor Graphic layout tool. (*This figure is presented in color; the black and white reproduction may not be an accurate representation*).

The schematic cross-section of the CMOS thin films and their spatial locations for the piezoresistive and nano-Newton force sensors is illustrated in Fig. 4.2. The typical CMOS layer thickness in AMI 0.5 μm technology, which was used in this project, is listed in Table 4.1 [49].

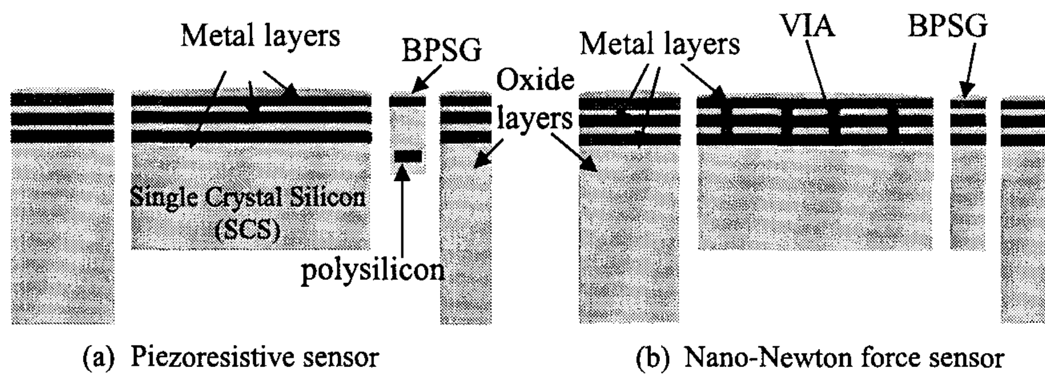

Fig. 4.2. Schematic cross-section of the release sensor showing the CMOS thin films and their relative locations.

Table 4.1

Typical CMOS Layers Thickness

Layer	Thickness (μm)
Single crystal silicon (SCS)	~250
Field oxide under polysilicon	0.4
Field oxide under metal 1	0.375
Gate oxide	0.0135
Metal	0.69
Polysilicon	0.35
VIA size	0.6 μm × 0.6 μm
Boro-phospho-silicate-glass (BPSG)	0.7

Device sample preparation is conducted at the Oakland University cleanroom, while post-CMOS microfabrication processes are conducted at the Lurie nano fabrication facility (LNF), University of Michigan, Ann Arbor.

4.1 Post-CMOS Microfabrication of a CMOS-MEMS Piezoresistive Accelerometer

The post-CMOS process steps of the piezoresistive accelerometer are carefully designed to successfully release the sensor structure. As shown in Fig. 4.3(a), the process starts with the selective application of photoresist at the back-side of the die around the sensor. Next in Fig. 4.3(b), a 4 inch carrier wafer is fully coated with photoresist then placed on the hot-plate at the temperature of 90 ^{o}C for 3 minutes. A portion of photoresist that exists in the middle of the carrier wafer is removed with aceton solution for sample placement. A thin layer of photoresist is then applied to the middle of the carrier wafer, followed by sample placement on the wet photoresist area. Both sample and the 4 inch carrier wafer are baked again for 3 minutes at 90 ^{o}C.

The second step of the post-CMOS process is the back-side bulk single-crystal silicon (SCS) etching to produce proof mass thickness of approximately 40 μm. A deep reactive ion etching (DRIE) is performed using STS plasma etcher to anisotropically etch the silicon substrate to the desired thickness. Optical microscope and Daktek surface profilometer are used to estimate the thickness of the proof mass during the etching process. Fig. 4.4(a) shows the schematic cross-section of the sensor after DRIE process with Fig. 4.4(b) shows the back-side view of the sensor that has been successfully etched to approximately 210 μm depth. The yellowish colour around the sensor shows the

photoresist coated area, which is applied prior to DRIE process. The recipe use to process the sample is listed in Table 4.2. From the back-side etching of the bulk silicon, the silicon etching rate is found to be ~5 μm/min.

The third process is SiO_2 reactive ion etching (RIE), which is performed from the front-side of the device using LAM 9400. Front side RIE process will open the pattern of the bimorphs and proof mass. The process starts by first flipping over the die such that the thin film is now on the front side. Aceton solution is used to remove the die prior to the flip over process. The die is then attached to the 4" carrier wafer using kapton tape and placed on another 6" carrier wafer as illustrated in Fig. 4.5. Few drops of Perfluoropolyether (PFPE) are used to bond the two carrier wafer together. Fig. 4.6(a)

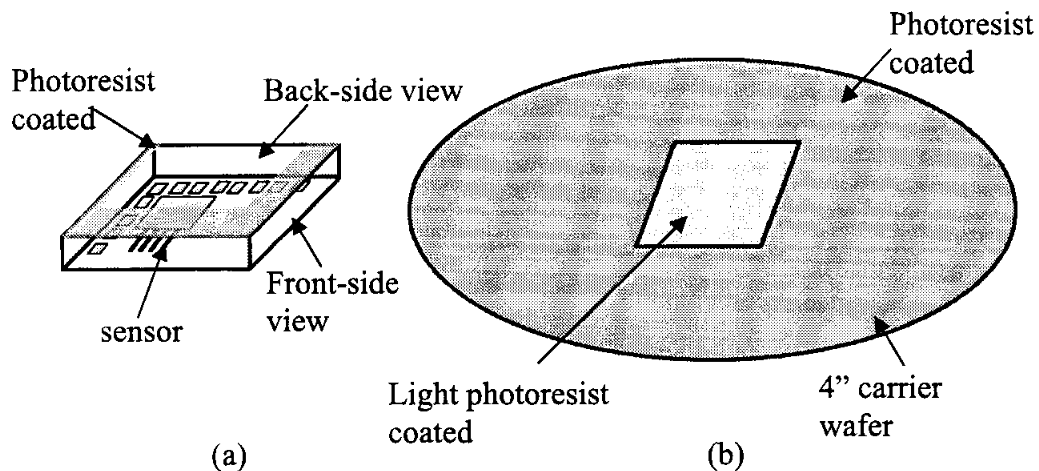

Fig. 4.3. (a) Back-side photoresist coated around the sensor, and (b) 4" carrier wafer coated with photoresist with the center of the wafer cleared for sample placement.

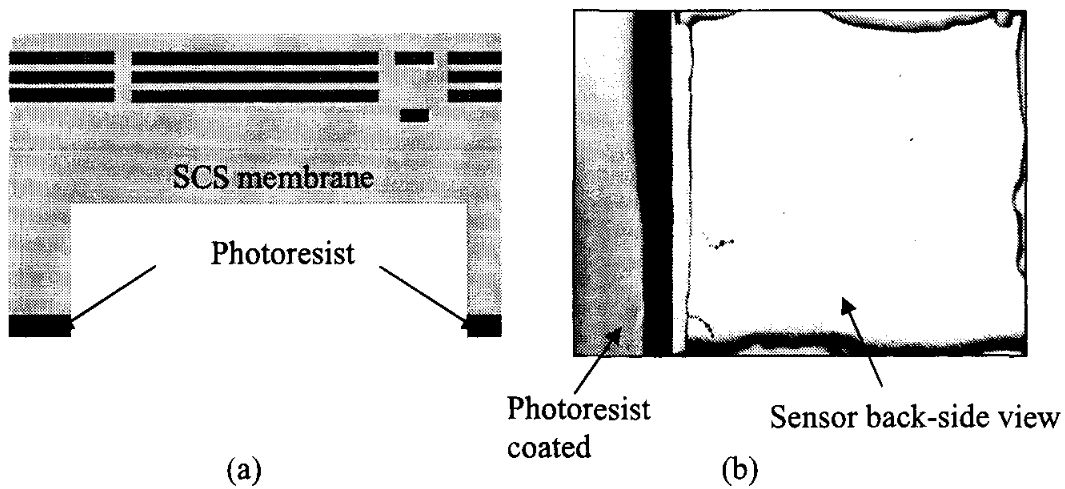

Fig. 4.4. (a) Schematic cross-section of the sensor, and (b) the back-side view of the sensor under optical microscope after DRIE process.

Table 4.2

Anisotropic DRIE Recipe for Back-side Silicon Etching (Recipe: QU1)

	Etch	Passivation	Unit
R.F Power:			
Platen power	200	0	Watt
Coil power	800	600	
Etch time: (Start)	13	7	Min
Gases:			
SF_6	160		Sccm
C_4F_8		85	

shows the schematic cross-section of the sensor after SiO_2 RIE process has completed with the appearance of trenches up to the SCS surface. Fig. 4.6(b) and Fig. 4.6(c) show the front-side view of the sensor during and after the etching process. A white bright colour on the sensor surface as shown in Fig. 4.6(b) indicates that metal 3 layer is exposed and the clearance of BSG material after approximately 10 minutes of etching.

After 40 minutes of etching, a gray colour (silicon colour) appears in the trenches that indicate the completion of SiO_2 etching as displayed in Fig. 4.6 (c). Referring to Fig. 4.6 (b), the test structures to the right of the sensor beam are used to estimate SiO_2 etching rate and to avoid over-etch of the SiO_2 material. The total SiO_2 etching depth is approximately 5 μm. The recipe use for SiO_2 etching is listed in Table 4.3. SiO_2 etching rate is found to be approximately 0.1 μm/min.

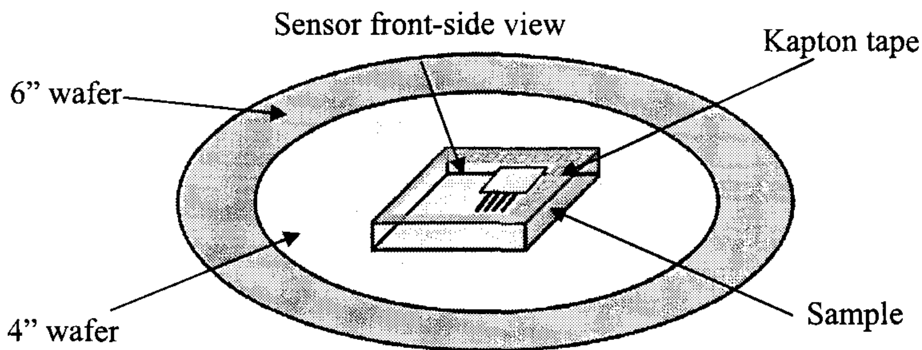

Fig. 4.5. Sample preparation prior to SiO_2 RIE process, which shows a sample on top of 4" and 6" carrier wafers.

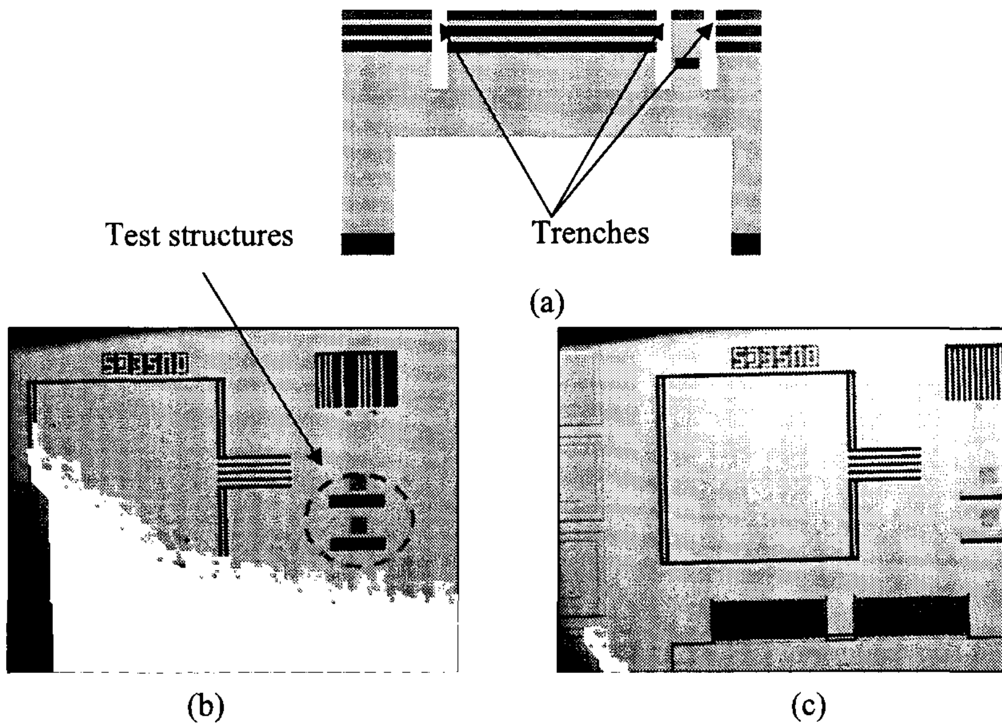

Fig. 4.6. (a) Schematic cross-section of the sensor after SiO_2 RIE, (b) the front-side view of the sensor after metal 3 is exposed, and (c) gray colour in trenches indicates that SiO_2 is fully etched.

Table 4.3

RIE Recipe for Front- Side SiO_2 Etching (Recipe: mnf_oxide1)

	Etch	Unit
Gases:		
SF_6	5	Sccm
C_4F_8	50	
He	50	
Ar	50	

Next step is to perform front-side bulk silicon DRIE process using the etching rate of 5 μm/min obtained from previous backside DRIE of silicon. The thickness of the membrane is approximately 40 μm, which is observed under Daktek and optical microscope during back-side etching. The sample on the 4" carrier wafer is etched for approximately 10 minutes in STS plasma deep silicon etcher using recipe QU1 as listed in Table 4.2. Since the trenches are narrower, more time is required and previous etching rate is no longer accurate. Therefore the test structures on the chip are used as reference. Fig. 4.7(a) illustrates the schematic cross-section of the sensor after the second silicon DRIE process with all the trenches etch-through. The image viewed under the optical microscope as shown in Fig. 4.7(b) shows part of dummy structure close to the bimorph beams has fallen but others still intact to the substrate. Additional 5 more minutes are required to fully etch-through. This happen when all the dummy structures dropped, which indicate that the etched-through process is completed.

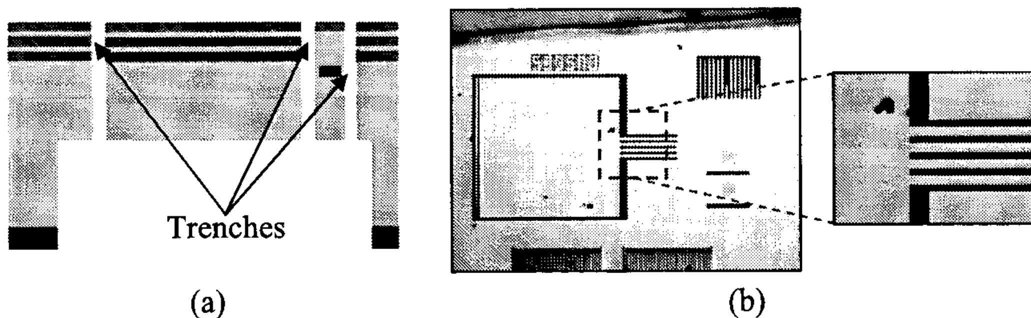

Fig. 4.7. (a) Schematic cross-section of the sensor after silicon DRIE, and (b) image under optical microscope after 10 minutes DRIE process.

The final step is to perform isotropic silicon etching that undercut the silicon underneath the bimorphs, which released the device, as illustrates by the schematic cross-section in Fig. 4.8 (a). The recipe use for silicon isotropic etching is listed in Table 4.4.

During isotropic etching, a small portion of the proof mass and substrate will also be undercut. Due to large proof mass dimension, small undercut under the proof mass will not affect sensor performance. After 20 minutes of etching as shown in Fig. 4.8(b), the test structures start to curl up, which indicate that silicon underneath the thin film is fully etched. Additional 5 more minutes are added to release the device. However, even with all the test structures found to have curled up, the device is still not release. Many un-broken connections from sensor structure to substrate are observed as shown in Fig. 4.8(c). To avoid too much undercut of the proof mass structure, the sample is flipped over for observation. Many un-broken connection between the substrate with sensor proof mass are also observed from back-side of the sensor structure. 5 minutes of back-side

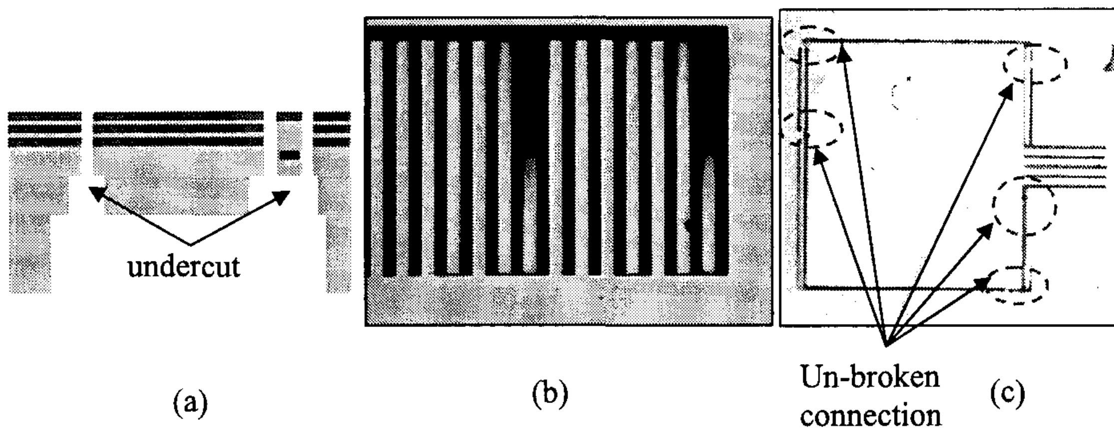

Fig. 4.8. (a) Schematic cross-section of the sensor after isotropic silicon etching, (b) test structure curling after 25 minutes of isotropic etching process, and (c) front-side image under optical microscope after 30 minutes of isotropic etching process.

silicon DRIE is required to finally release sensor proof mass from the substrate as shown in Fig. 4.9. The back-side photoresist is removed by oxygen ashing.

Fig. 4.10 shows a scanning electron microscope (SEM) photograph of the fabricated sensor with inset showing a close-up of the bimorph. The structure curling from Fig. 4.10 is due to the residual stress existing among the CMOS thin films. Residual stress is the stress that remains after the original cause of stresses such as the heat gradient that occur during the fabrication and post-CMOS processing has been removed.

Table 4.4

Front-Side Isotropic Silicon Etching (Recipe: QU_ISO)

	Etch	Passivation	
R.F Power:			
Platen power	50	0	Watt
Coil power	800	0	
Etch time:	5	0	Min
Gases:			
SF_6	160	0	Sccm

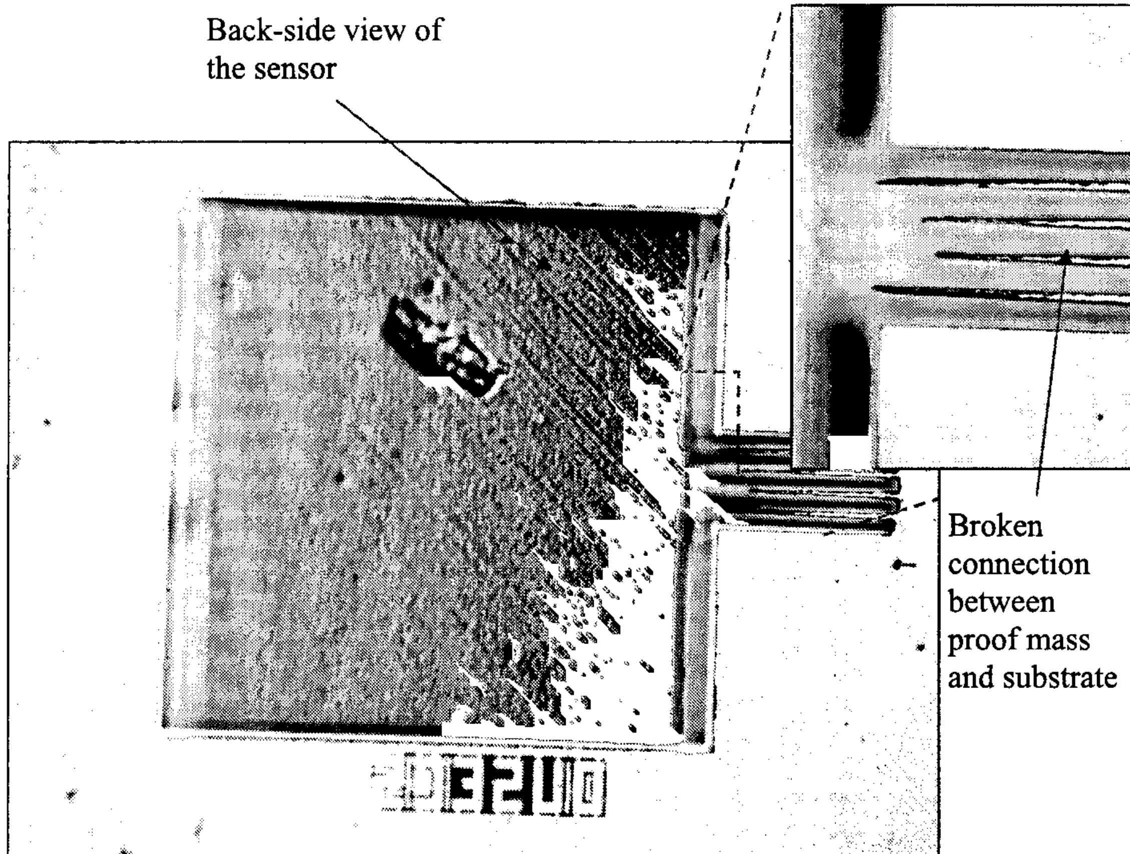

Fig. 4.9. Sensor back-side view under optical microscope with inset showing the close-up of the disconnection between substrate and proof mass bottom after 5 minutes of silicon DRIE process, which releases the structure.

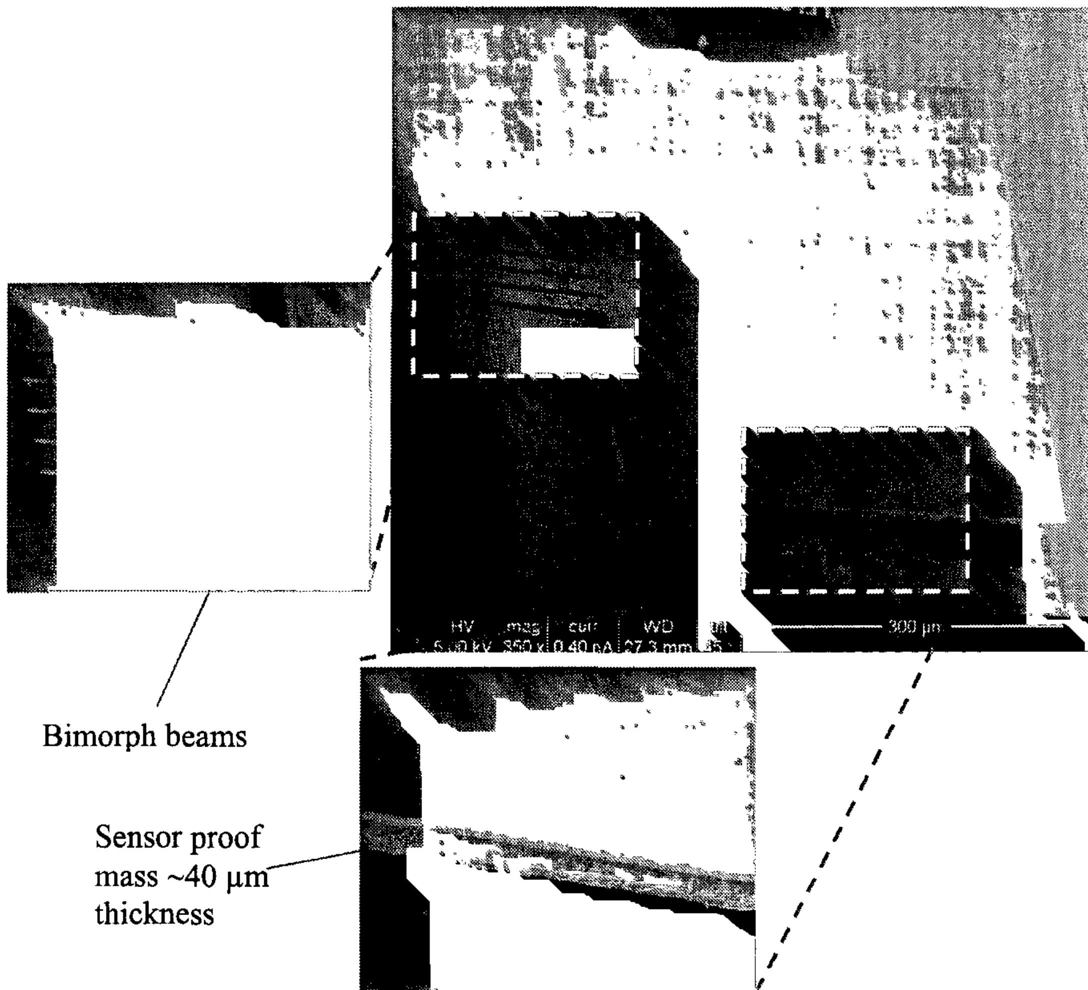

Fig. 4.10. SEM image of the fabricated CMOS-MEMS accelerometer with inset showing the bimorph beams where the piezoresistors are located.

4.2 Post-CMOS Microfabrication of a CMOS-MEMS Nano-Newton Force Sensor

The post-CMOS process steps of the nano-Newton force sensor are similar to the process steps of the piezoresistive accelerometer except the isotropic bulk silicon etching, which is not required in force sensor microfabrication steps and will be explain in the sequel. The process starts with the selective application of photoresist at the back-side of the die around the sensor followed by sample placement on the lightly coated 4 inch carrier wafer area as shown in Fig. 4.11. The carrier wafer is then placed on the hot-plate at the temperature of 90 ^{o}C for 3 minutes.

The second step of the process is to perform back-side silicon DRIE to achieve proof mass thickness of approximately 40 μm. STS plasma deep silicon etcher is used to anisotropically etch the silicon substrate to the desired thickness. Fig. 4.12 illustrates the schematic cross-section of the sensor after DRIE process is completed. Similar process

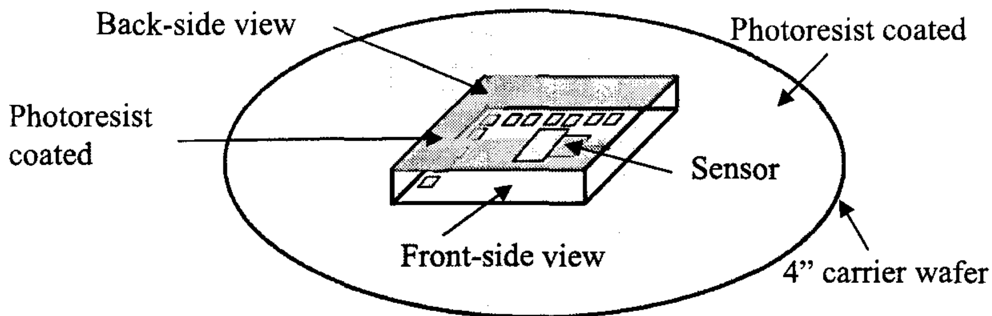

Fig. 4.11. Back-side view of the sample coated with photoresist and placed on the 4" carrier wafer.

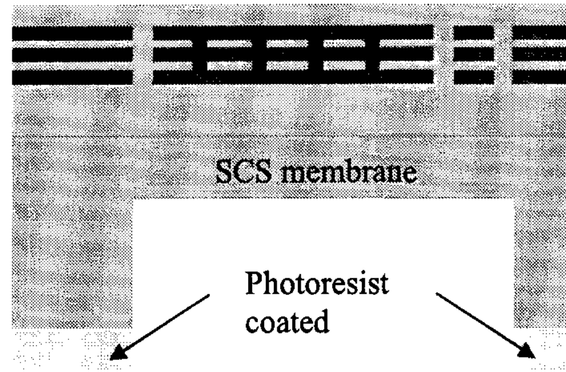

Fig. 4.12. Schematic cross-section of the nano-Newton force sensor after back-side silicon DRIE process.

recipe (QU1) as listed in Table 4.2 is used for this process. Etching time of approximately 45 minutes is required to etch the bulk silicon up to 210 μm deep. Using Daktek and optical microscope, the etching rate of 3 μm/min is observed for the DRIE process.

Next, the sample is removed from the 4 inch carrier wafer using aceton solution then flipped for the front-side processing to take place. The sample is then transferred to a new 4 inch carrier wafer, which is fully coated with photoresist followed by soft baking of the sample at a temperature of 90 °C for approximately 15 minutes. Prior to front-side SiO_2 RIE, the 4" carrier wafer with the sample is glued to a 6" carrier wafer with PFPE. SiO_2 etch recipe is as listed in Table 4.3. Fig. 4.13 shows a schematic cross-section of the sensor after SiO_2 RIE process and the front-side view of the sensor under the optical microscope before SiO_2 RIE. Etching duration of approximately 36 minutes is required to completely etch the BPSG and SiO_2 layers in the trenches.

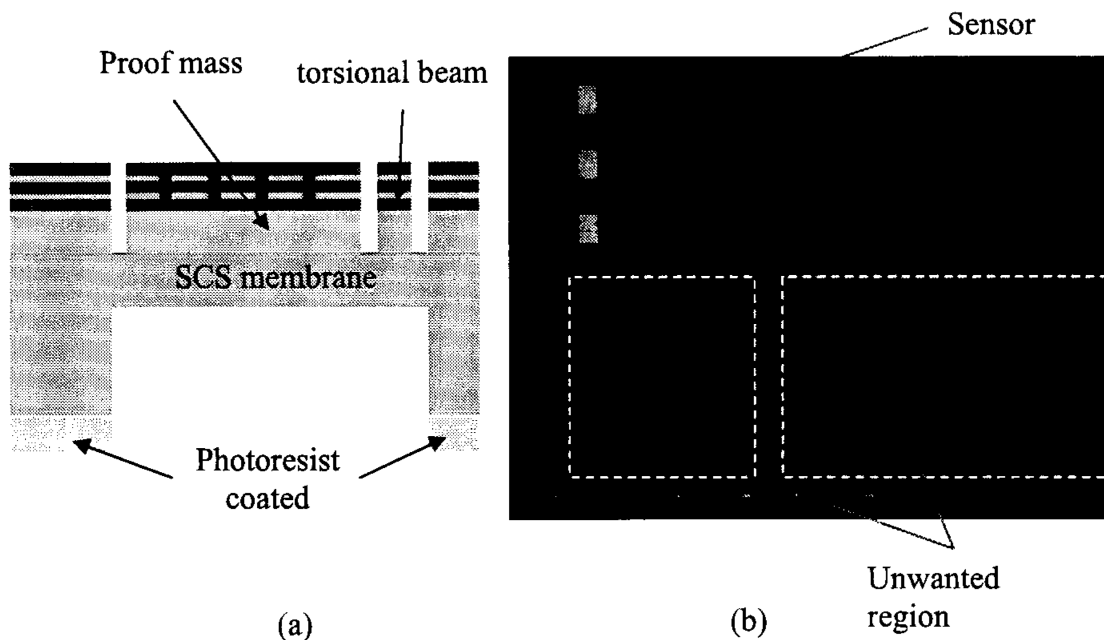

Fig. 4.13. (a) Schematic cross-section of the nano-Newton force sensor after front-side SiO_2 RIE process and (b) the sensor front-side view under the optical microscope.

The final post-CMOS microfabrication step to release the sensor structure from the substrate is to perform front-side anisotropic SCS membrane etch-through using STS plasma deep silicon etcher. Using the recipe listed in Table 4.2, etching duration of approximately 27 minutes are required for the structure to be successfully released. The unwanted region as shown in Fig. 4.13 (b) will automatically fall when the device is fully released. Fig. 4.14 shows a schematic cross-section of the sensor after the sensor is fully released and the SEM pictures of the sensor with the inset showing the close-up view of the sensing comb fingers.

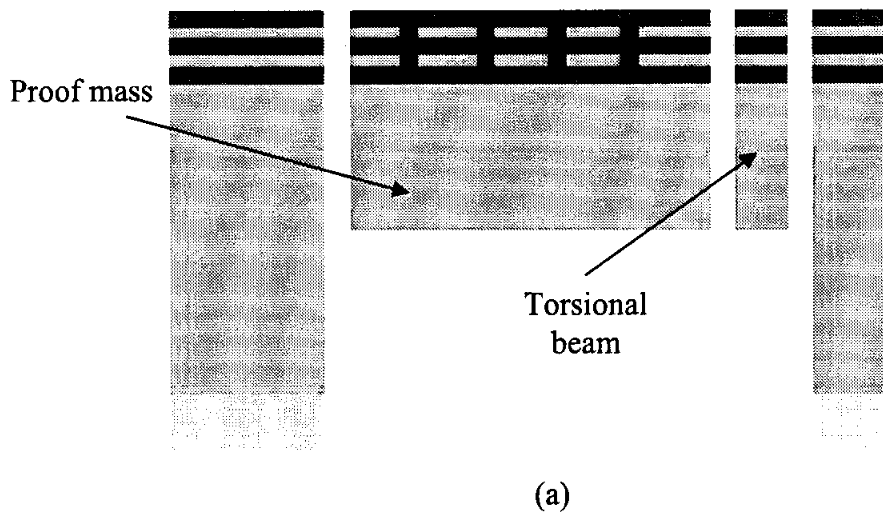

(a)

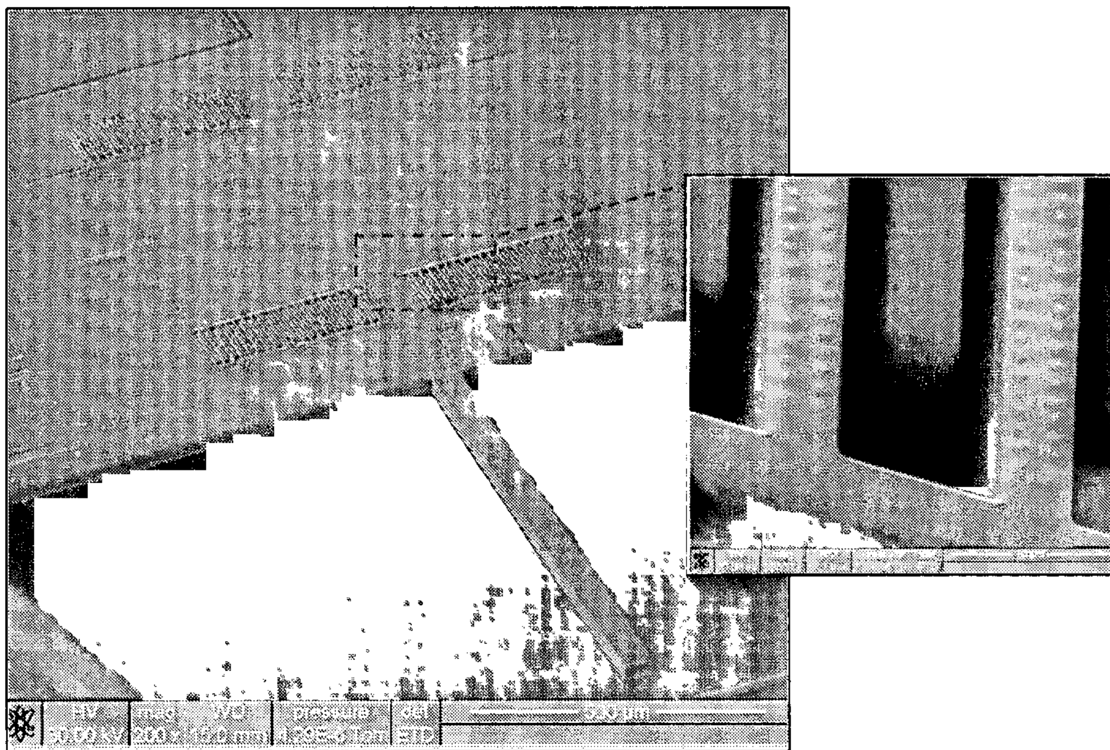

(b)

Fig. 4.14. (a) Schematic cross-section of the nano-Newton force sensor after the sensor is fully released and (b) the SEM picture of the sensor with the inset showing the close-up view of the sensing comb fingers.

4.3 Conclusion

The post-CMOS microfabrication processes of the piezoresistive and nano-Newton force sensor have been designed and successfully implemented to release the device structures. Back-side anisotropic DRIE process using STS deep silicon etcher is used to obtain the desired proof mass thickness of approximately 40 μm. A selective photoresist is been applied around the sensor as the mask for the back-side etching. Plasma RIE using LAM 9400 is utilized for the front-side SiO_2 etching to etch-through approximately 5 μm of SiO_2 material in the trenches. Daktek surface profilometer and optical microscope are used to estimate the etching rate. The availability of the multi-level test structures are helpful to avoid over-etches of the thin film materials. The use of dummy structures to obtain wider gap between the device and the substrate are found to be successful but may introduce some problem as it may stuck between the device and the substrate, which may prevent the device from releasing successfully. Using the back-side DRIE etching rate, the front-side silicon DRIE process time can be estimated to etch-through and disconnect the device from the substrate. An isotropic etching process with no passivation is used to undercut the SCS material underneath the thin film of the bimorph beams, which successfully released the piezoresistive accelerometer structure.

CHAPTER FIVE

DEVICE CHARACTERIZATION

This chapter reports the CMOS-MEMS piezoresistive accelerometer and nano-Newton force sensors device characterization, which is performed after post-CMOS microfabrication. To validate the uniqueness of the sensing mechanism, in this work no conditional circuit is integrated on the chip. Instead, a commercially available amplifier and signal conditioning circuit are used or built for the device test. Prior to device characterization, Section 5.1 elaborates on device packaging followed by characterization setup in Section 5.2. Section 5.3 discusses the piezoresistive accelerometer characterization, which includes accelerometer calibration, resistance measurement, noise measurement, mechanical, off-chip, dynamic, and temperature tests. Section 5.4 explains the nano-Newton force sensor characterization, which covers universal capacitive board calibration, noise measurement, mechanical, off-chip, and dynamic tests. For both devices, their characterization setup and result are explained and discussed.

5.1 Device Packaging

CMOS-MEMS sensors are packaged in a standard ceramic 16 pins dual in-line package (DIP) for ease connection with external circuitry and instruments. Sensors are mounted in the package using silver epoxy, which has to be cured in the oven with a temperature of 65 ^{o}C for approximately 10 minutes. Device pads are connected to the package leads using gold wires. Wire bonding process is conducted using K&S 4123 wire

bonder, which is performed at the University of Michigan wet chemistry lab. The die pin-out and the bonding configuration for both sensors is shown in Fig. B.1 (Appendix B.1).

5.1.1 Packaging of the Piezoresistive Accelerometer

The 16 pins DIP that contains the piezoresistive accelerometer chip is shown in Fig. 5.1. For ease deployment of sensor characterization, the package is assembled on the 16 pins socket together with Kistler type 8692B50 reference accelerometer on the printed circuit board (PCB). The PCB is mounted on the transparent plastic, which is screwed to the shaker pole. The External wires are used for the connection between the sensor and the off-chip amplifier.

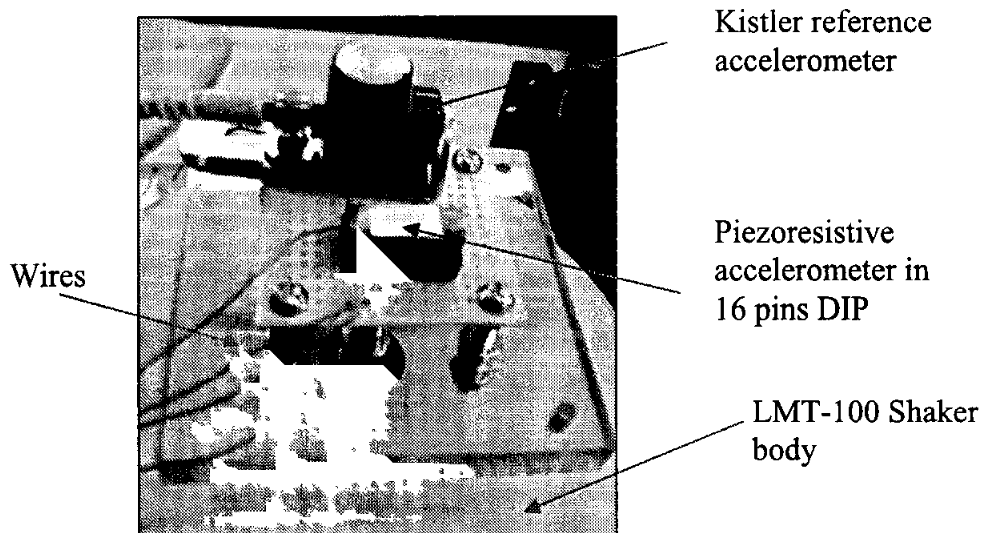

Fig. 5.1. Test board on which the DUT and the reference accelerometer are mounted.

5.1.2 Packaging of the Nano-Newton Force Sensor

A ceramic 16 pins dual in-line package (DIP) with 10 package leads removed is used to package the force sensor for convenient sensor deployment. The sensor chip in package is mounted into the 8 pins socket, which is soldered to the printed circuit board as shown in Fig. 5.2.

5.2 Sensor Characterization Setup

This section explains the equipment and their setup for the piezoresistive accelerometer and nano-Newton force sensor prior to device characterization. The necessity of a dedicated setup is required for each device due to different device operations and working principles. Commercial and in-house amplifier and signal conditioning circuits are used or built for device test.

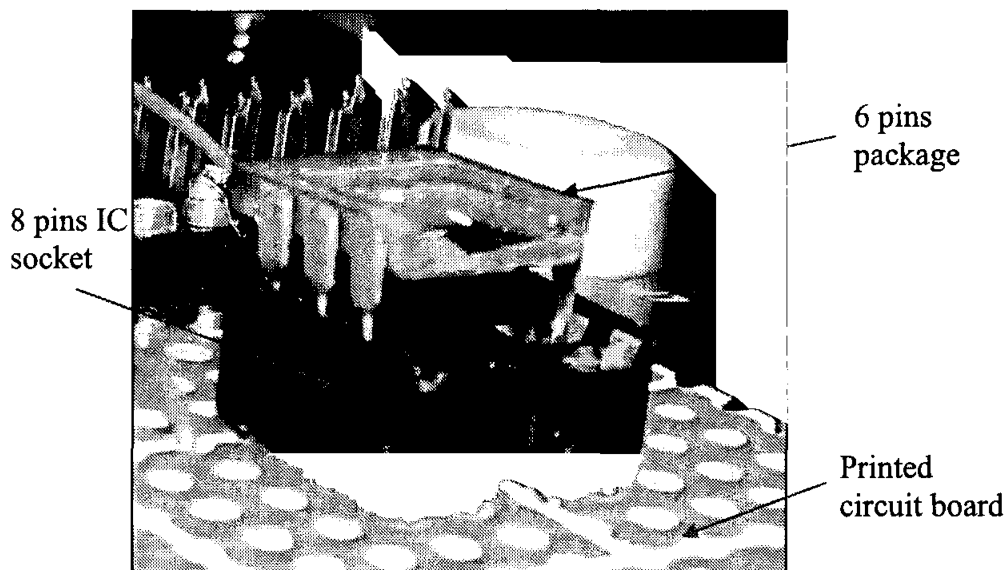

Fig. 5.2. Nano-Newton force sensor chip in a ceramic 6 pins DIP package.

5.2.1 Piezoresistive Accelerometer Characterization Setup

Piezoresistive accelerometer characterization setup utilizes standard instruments such as digital multimeter, Tektronix AFG3021 signal generator, Tektronix TDS2014B oscilloscope, RSR triple power supply, Piezotronics 394C06 hand held shaker, Kistler type 8692B50 commercial accelerometer, Kistler 5004 dual mode amplifier, and HP 2562A dynamic signal analyzer. The setup configures for the piezoresistive accelerometer characterization is shown in Fig. 5.3. Piezotronics 394C06 hand held shaker is used to calibrate Kistler type 8692B50 reference accelerometer at a frequency of ~160 Hz and amplitude of 100 mV for 1g acceleration. The calibrated Kistler accelerometer and the piezoresistive accelerometer in package are both placed on the test board which is screwed to the threaded pole of the shaker as seen in Fig. 5.3. Input signal from Tektronix AFG3021 signal generator is amplified by the Ling's amplifier, which drives the Ling LMT-100 shaker. The gain of the amplifier and the signal generator amplitude are adjusted accordingly to produce the output of 100 mV, ~160 Hz at 1g, which is observed using the oscilloscope. The polysilicon resistors, which are used as the sensing materials are arranged in Wheatstone bridge configuration as shown by the schematic diagram in Fig. 5.4. Fully differential signal produced by the sensor is then amplified by the external off-chip amplifier.

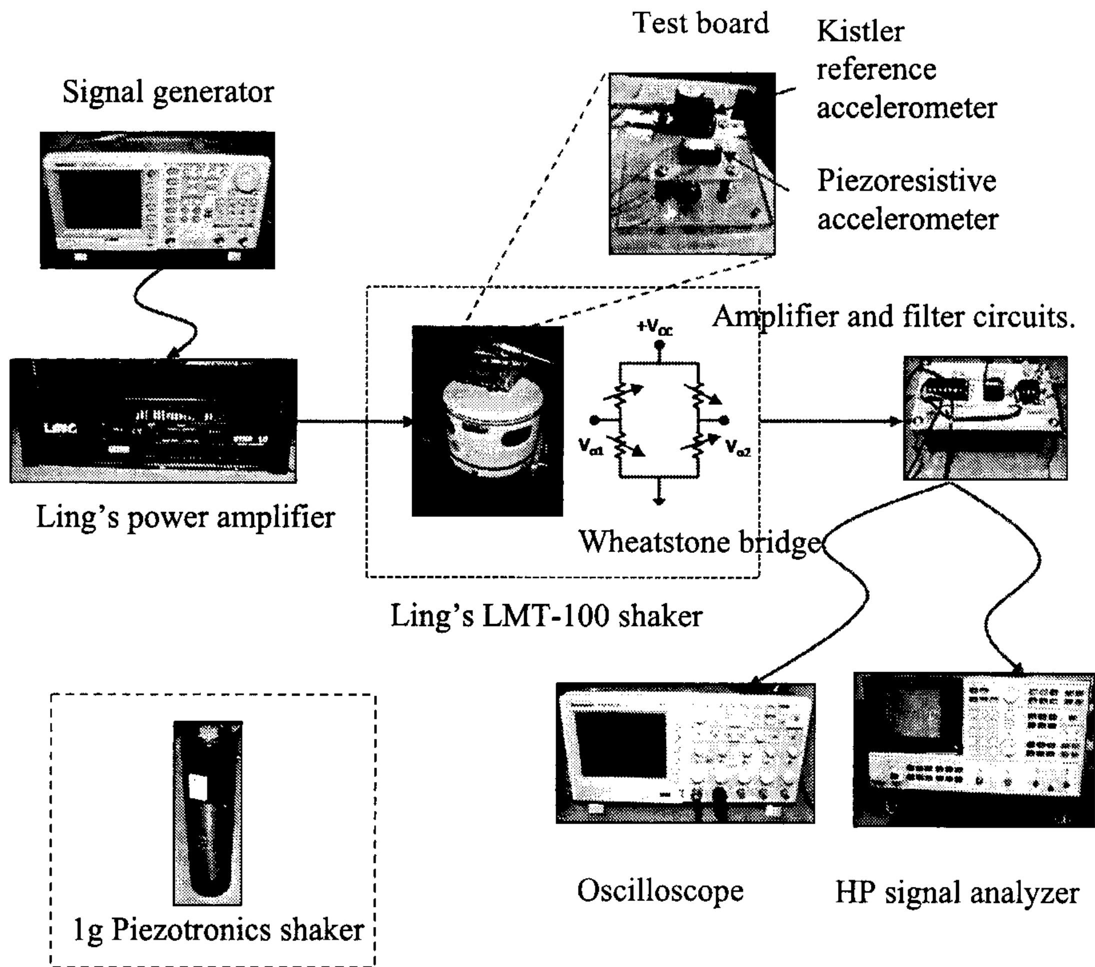

Fig. 5.3. Piezoresistive accelerometer characterization setup.

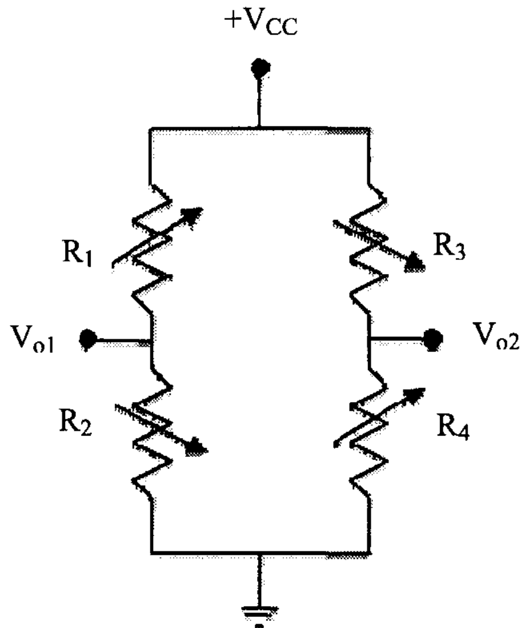

Fig. 5.4. Schematic diagram of the Wheatstone bridge configuration implemented for the piezoresistive accelerometer.

R_1 to R_4 are the longitudinal and transverse polysilicon resistors. The supply voltage, V_{CC} is chosen to be 1.49 V to provide approximately 1.12 mA of supply current to the Wheatstone bridge circuit. The output signal from the Wheatstone bridge is fed to the differential amplifier and filter circuit. The schematic diagram of the amplifier and the filter circuit is shown in Fig. 5.5. The instrumentation amplifier and the band-pass filter circuit have an overall gain of ~52 dB. The transient and frequency response of the sensor can are obtained at the output of the filter circuit, V_{out}, which can be measured using the oscilloscope and HP 2562A dynamic signal analyzer.

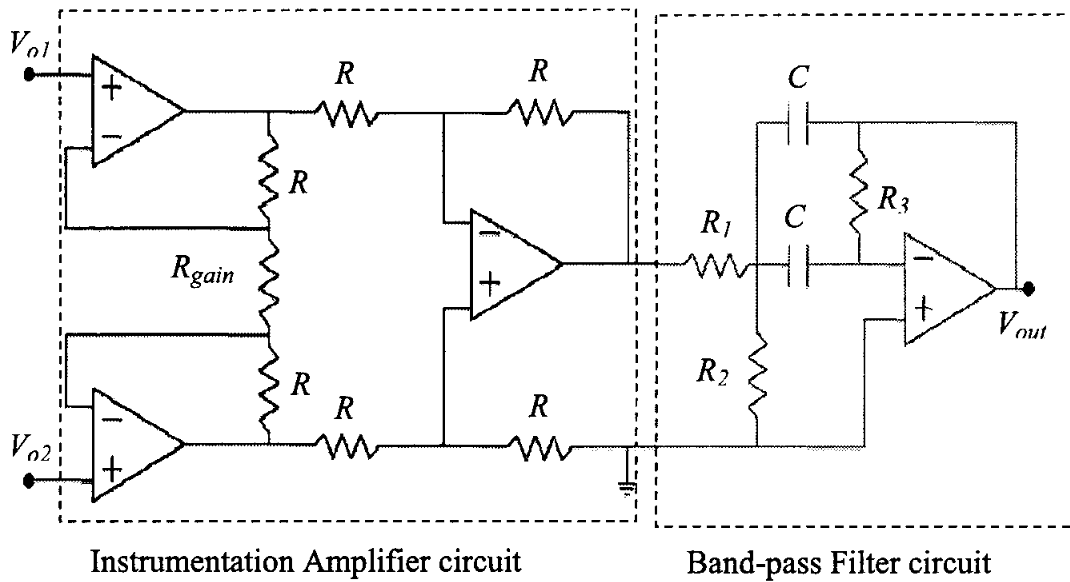

Fig. 5.5. The schematic diagram of the instrumentation amplifier and the high Q band-pass filter circuits.

PUSAT SUMBER MAKLUMAT
UNIVERSITI TEKNOLOGI PETRONAS

The total gain of the circuit is given by

$$A_v = \left(1 + \frac{2R}{R_{gain}}\right)\left(\frac{R_3}{2R_1}\right), \tag{5-1}$$

while the centre frequency and the bandwidth of the band pass filter can be calculated using the following equation.

$$f_o = \frac{1}{2\pi\sqrt{(R_1 \parallel R_2)R_3}} \text{ [Hz]} \tag{5-2}$$

$$BW = \frac{1}{\pi R_3 C} \text{ [Hz]} \tag{5-3}$$

5.2.2 Nano-Newton Force Sensor Characterization Setup

Nano-Newton force sensor characterization setup comprises of a standard instrument such as digital multimeter, Tektronix TDS2014B oscilloscope, RSR triple power supply, Piezotronics 394C06 hand held shaker, Kistler 5004 dual mode amplifier, and HP 2562A dynamic signal analyzer. Moreover, the setup also utilizes a commercial MS3110 universal capacitive readout circuit to sense the capacitance change of the sensor. The setup configures for the nano-Newton force sensor characterization is shown in Fig. 5.6. Piezotronics 394C06 hand held shaker is used to observe the sensor response at 1g acceleration with the frequency of ~160 Hz and amplitude of 100 mV. The schematic diagram of MS3310 universal capacitive readout circuit is given in Appendix B.2, while its functional block diagram and the output voltage equation, V_o is shown in Fig. 5.7 and Eqn. (5-4). The output voltage, V_o, from the capacitive readout circuit is given by

$$V_o = \frac{GAIN \times V2P25 \times 1.14 \times \left(CS2_T - CS1_T\right)}{C_F} + V_{REF}, \qquad (5\text{-}4)$$

where

Gain = 2 or 4V

V2P25 = 2.25 VDC nominal

$CS2_T$ = CS2IN + CS2

$CS1_T$ = CS1IN + CS1

C_F = ≥ 1.5 pF (optimize) and V_{REF} = 2.25 V.

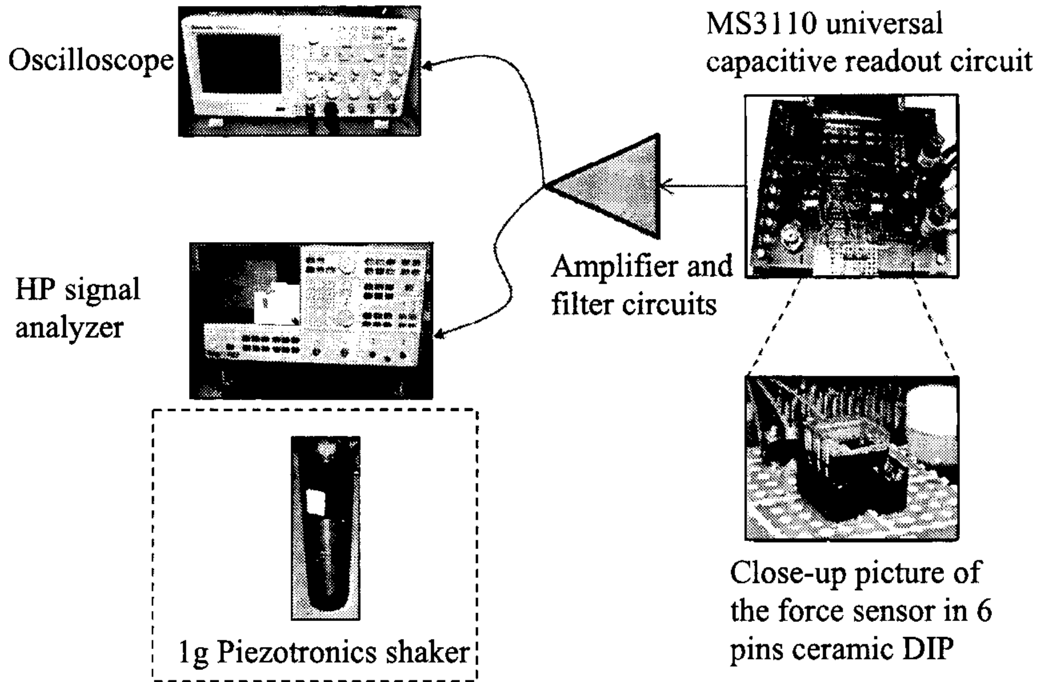

Fig. 5.6. Nano-Newton force sensor characterization setup.

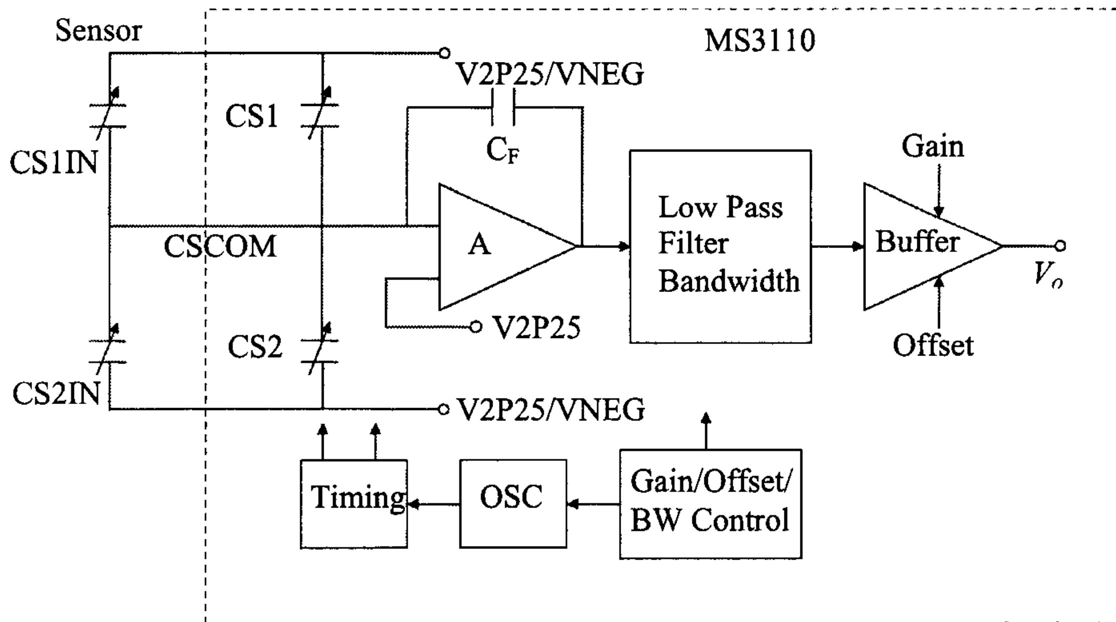

Fig. 5.7. MS3110 universal capacitive circuit schematic diagram.

The output signal, V_o, which is observed at the output of the universal capacitive readout circuit is still found to be very noisy and low in amplitude. To overcome this problem, another external amplifier and a low pass filter circuits are constructed. The schematic diagram of the amplifier and a low pass filter with a total gain of 43 dB is shown in Fig. 5.8. AD 627 an integrated, micropower instrumentation amplifier that delivers rail-to-rail output swing on single and dual (+2.2 V to ±18 V) supplies is used as an amplifier. The dynamic and noise analysis of the sensor are obtained by connecting the output of the filter circuit to the input of the oscilloscope and HP 2562A dynamic signal analyzer. The total gain of the amplifier and the cut-off frequency of the filter are given by

$$V_{out} = \left[V_{IN(+)} - V_{IN(-)} \right] \times \left(5 + 200k\Omega / R_G \right) + V_{REF}, \tag{5-5}$$

$$f_c = \frac{1}{2\pi RC}, \tag{5-6}$$

where R_G is the external gain resistor, which can be connected between pin 1 and pin 8 of the AD 627 instrumentation amplifier. The amplifier gain can be varied easily by varying the external gain resistor, R_G. A single supply of + 15 V DC is used for AD 627 power supply. To further improve the quality of the output signal and to reduce unnecessary external noise interference, the sensor and all its circuitry are placed in the Faraday's cage as shown in Fig. 5.9.

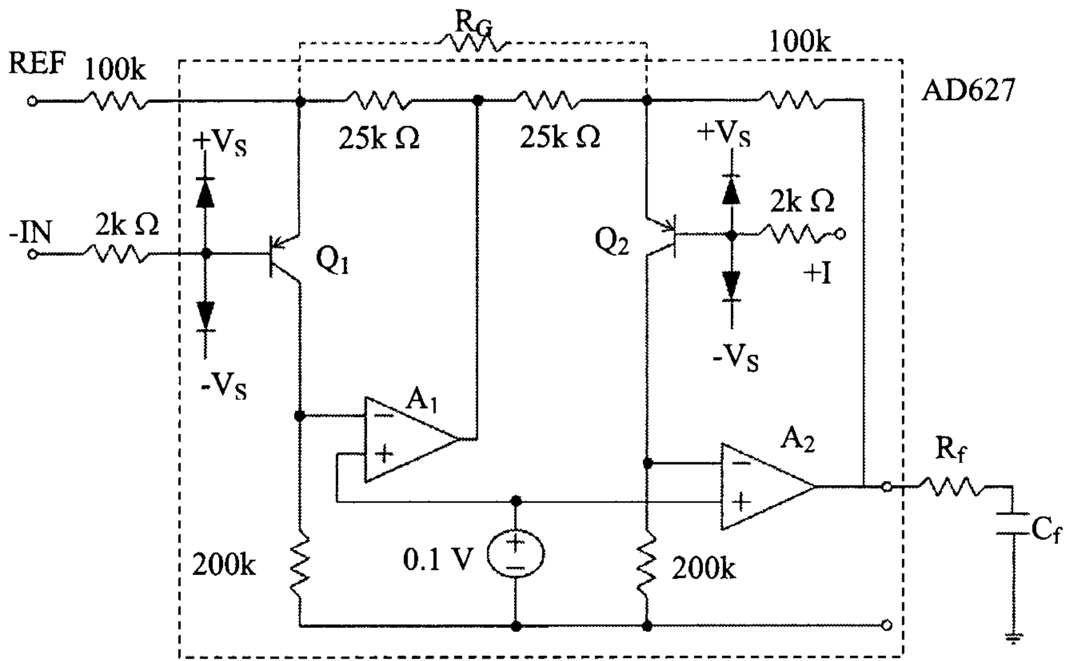

Fig. 5.8. The schematic diagram of the amplifier (AD 627) and low pass filter used for nano-Newton force sensor characterization.

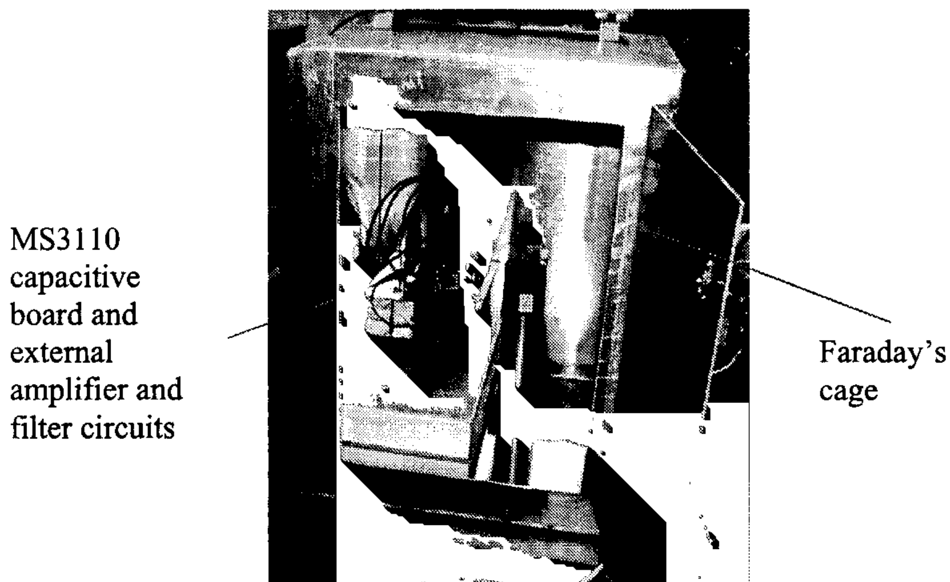

Fig. 5.9. Force sensor and its circuitry in the Faraday's cage.

5.3 Piezoresistive Accelerometer Characterization

This section discusses the piezoresistive accelerometer characterization and their results. Prior to device characterization, Kistler type 8692B50 commercial accelerometer is first calibrated using the Piezotronics 394C06 hand held shaker followed by the poly resistors resistance measurement, the mechanical test to estimate device resonant frequency, off-chip test, sensor noise measurement, the dynamic test for output waveform observation, and the temperature tests. The setup as shown in Fig. 5.3 is used for all the tests except for the temperature test, which is performed in the Blue M laboratory oven.

5.3.1 Kistler Type 8692B50 Accelerometer Calibration

In this work, Kistler type 8692B50 accelerometer is used as the reference accelerometer. For calibration purposes, the reference accelerometer is placed on the Piezotronics 394C06 hand held shaker as shown in Fig. 5.10. Hand held shaker operates at ~160 Hz with the sensitivity of 100 mV/g. The output signal from the Kistler accelerometer is amplified by the Kistler 5004 dual mode amplifier, which can be calibrated to produce the output voltage of ~160 Hz, 100 mV_{p-p} at 1 g as shown in Fig. 5.11. Once the reference accelerometer is calibrated, it is placed on the test board together with the tested piezoresistive accelerometer as shown in Fig. 5.3. The initial acceleration amplitude produced by Ling's LMT-100 shaker will be based on the calibrated value of 100 mV_{p-p} for 1 g acceleration.

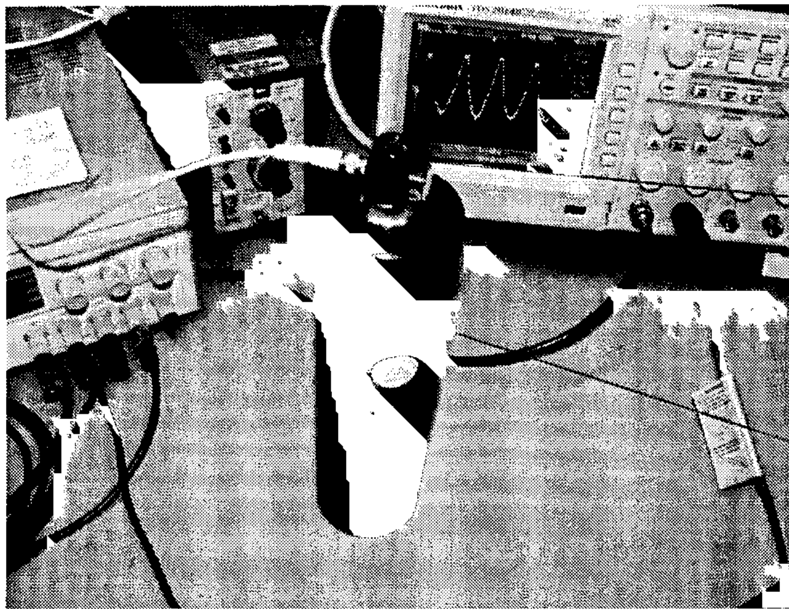

Fig. 5.10. Kistler reference accelerometer on Piezotronics hand held shaker.

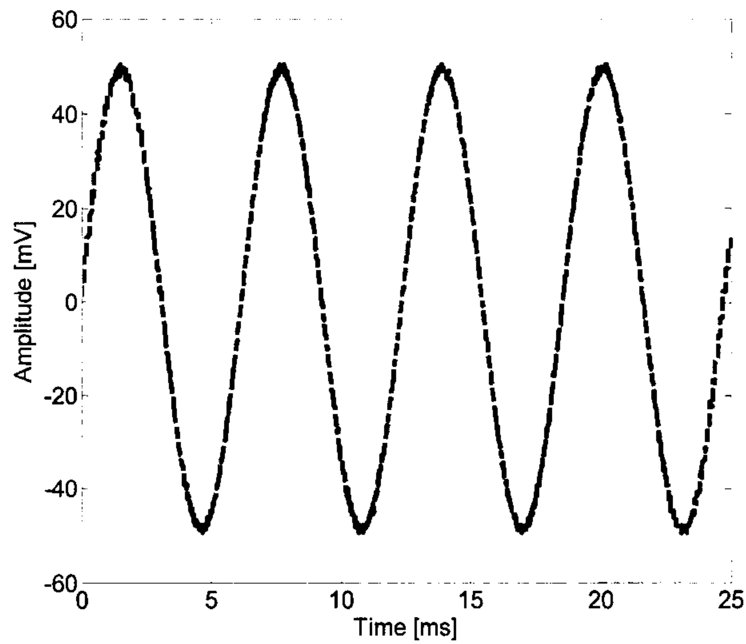

Fig. 5.11. Calibrated reference accelerometer output at 1g acceleration.

5.3.2 Resistance Measurement

The polysilicon resistors embedded in the piezoresistive accelerometer beams are arranged in longitudinal and transverse configuration as shown in the schematic diagram in Fig. 5.12, where the pin numbers used from the 16 DIP are included. The resistance in each beam is measured using a standard voltmeter and its value is listed in Table 5.1. The theoretical value of the polysilicon resistance is calculated at 1.1 kΩ, while ~1.4 kΩ is obtained through measurement. The differences of resistance between the theoretical and measurement value may due to the polysilicon sheet resistance tolerance and signal routing from device to pads.

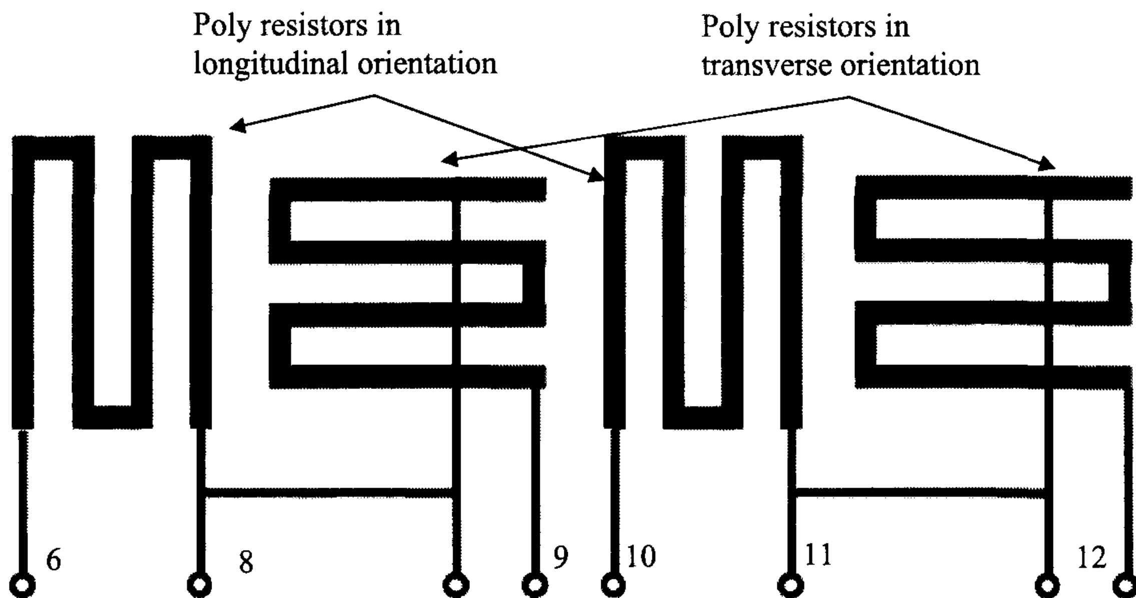

Fig. 5.12. Polysilicon resistors configuration including the 16 DIP pin numbers.

Table 5.1

Actual Polysilicon Resistors Measurement

16 DIP Pin Out	Resistance (kΩ)
6 - 8	1.33
8 - 9	1.36
10 - 11	1.40
11 - 12	1.42

5.3.3 Mechanical Test

The mechanical test for the piezoresistive accelerometer is performed to estimate the resonant frequency of the device. An impulse signal as shown in Fig. 5.13 is applied to the sensor to obtain a frequency sweep. The data is then captured by the oscilloscope and is processed in Matlab using fast Fourier transform (FFT) to obtain the frequency response of the device. The dynamic output frequency response of the sensor is illustrated in Fig. 5.14, which indicates the first resonant frequency of the sensor at ~1.34 kHz. The resonant frequency obtained through experimental method is close to the analytical and FEA methods, which estimate the resonant frequency of the sensor at 1.85 kHz and 1 kHz, respectively. The differences are due to the slight undercut of the silicon proof mass during the post-CMOS microfabrication process.

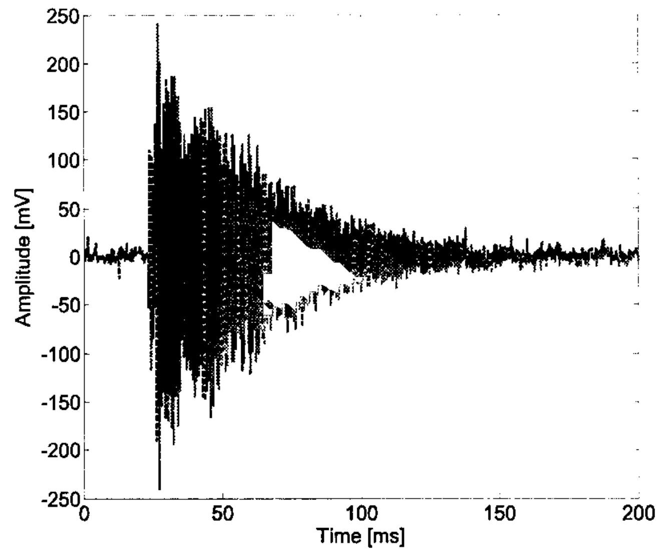

Fig. 5.13. Impulse signal applied to the sensor.

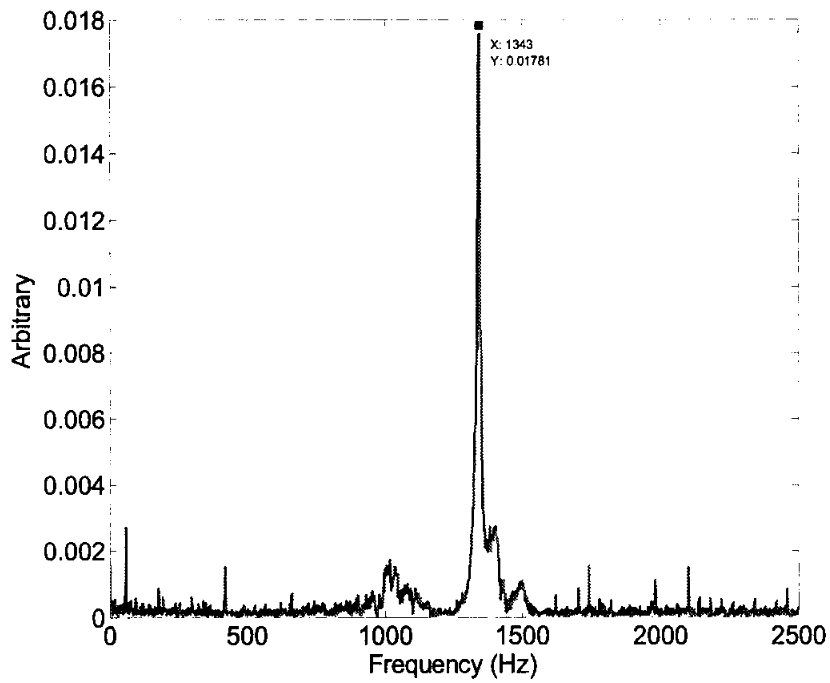

Fig. 5.14. Dynamic frequency response of the sensor with impulse signal.

5.3.4 Off-Chip Circuit Test

Off-Chip circuit test is conducted to evaluate the performance of the instrumentation amplifier and the filter circuits. The picture of this circuit is as shown Fig. 5.3. A dc voltage of ±15 V is used as the supply voltage. To check the performance of the circuit, no sensor is connected at the input. Instead, the input signal of 50 mV in amplitude is supplied by the signal generator. The amplifier and filter circuit have demonstrated an overall gain of approximately 52 dB.

5.3.5 Noise Measurement

The noise floor of the system consists of the mechanical (Brownian) and electrical noise. The noise measurement is required to determine the minimum acceleration detectable by the sensor. The overall noise floor is given by

$$a_n = \sqrt{a_m^2 + a_e^2} = \sqrt{a_m^2 + \left(\frac{V_e}{S}\right)^2}, \text{ [g/}\sqrt{\text{Hz}}\text{]} \quad (5\text{-}7)$$

where a_n, a_m, and a_e are the total noise, mechanical noise, and electrical (circuit) noise. V_e is the input-referred noise in V/√Hz, while S is the sensitivity of the piezoresistive accelerometer. The overall noise floor is measured on HP signal analyzer, which is configured to have a frequency span of 800 Hz and an average of 10 for each frequency. From the test, the overall noise floor is found to be -90 dB V/√Hz or 31.6 μV/√Hz as shown in Fig. 5.15.

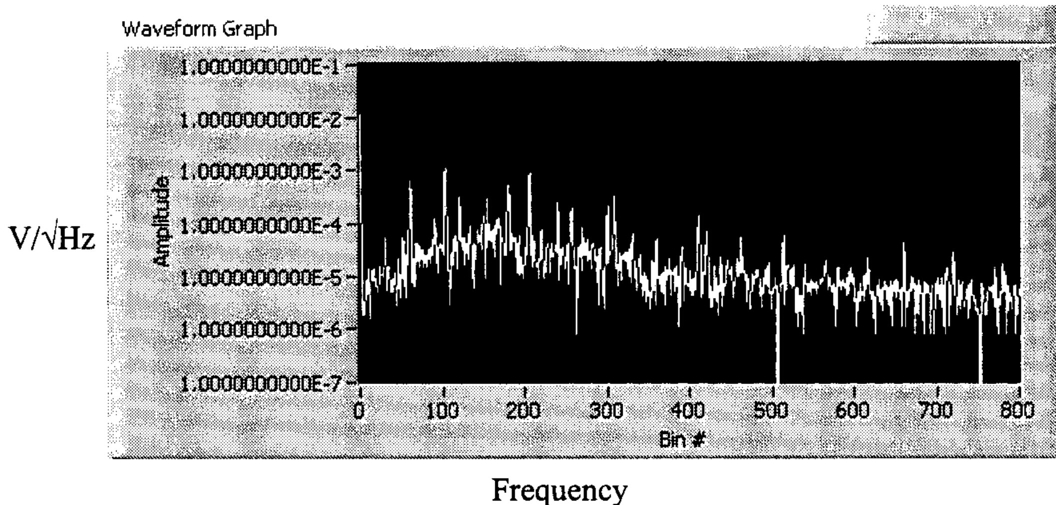

Fig. 5.15. Overall noise of the system including the sensor, the amplifier and the filter circuits.

Using HP signal analyzer as shown in Fig. 5.16, the electrical or circuit noise is found to be -100 dB V/√Hz or 10.0 μV/√Hz, which can be measured from the output of the amplifier circuit with no sensor connected to its input. The sensitivity, S is determined as 0.07 mV/g from the dynamic test in Section 5.3.6. At 52 dB amplification gain, the input-referred noise is calculated as 25.2 nV/√Hz. With a sensitivity of 31 mV/g after amplification, the total noise is found to be 1.03 mg/√Hz and the electrical noise is calculated using Eqn. (5-7) as 0.33 mg/√Hz. With the knowledge of the overall noise and the electrical noise, the mechanical noise is found to be 0.98 mg/√Hz. By selecting the bandwidth of 1 kHz, which is applicable for most applications, the minimum detectable acceleration is calculated as 32 mg using Eqn. (5-8).

$$a_{\min} = a_n \cdot \sqrt{BW} \tag{5-8}$$

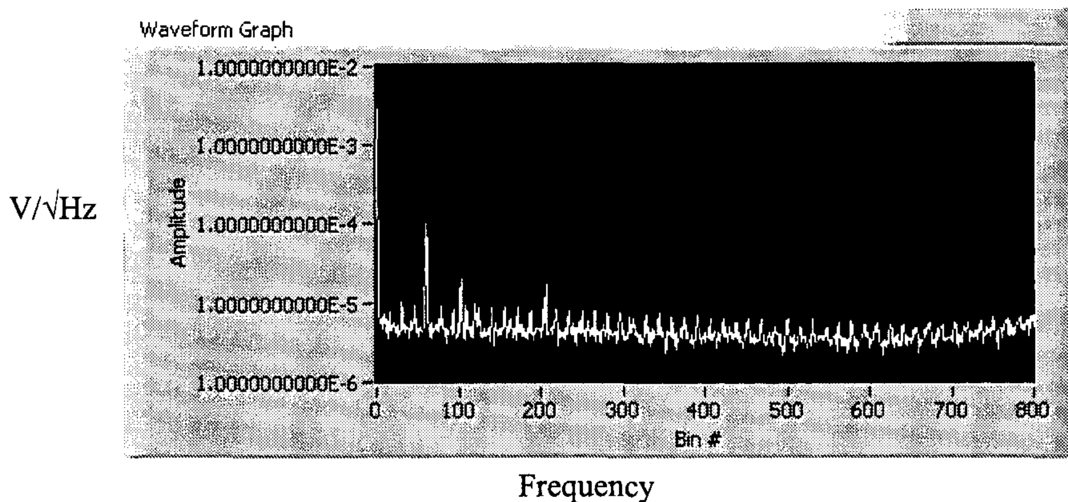

Fig. 5.16. Electrical (circuit) noise of the amplifier and filter circuit measured using HP signal analyzer.

5.3.6 Dynamic Test

The dynamic test for the piezoresistive accelerometer is performed on Ling's LMT-100 shaker, which is capable to produce acceleration up to 100g. The dynamic test setup is as shown in Fig. 5.3 and Fig. 5.17. Fig. 5.17 shows the device under test with the complete equipment wiring connection. The test is conducted for waveform observation for the acceleration from 1g to 7g. As explained in Section 5.3.1, prior to the test, the reference accelerometer is calibrated at ~160 Hz, 100 $mV_{p\text{-}p}$ for 1g acceleration. The input signals of 100 mVp-p to 700 mVp-p are being provided by the signal generator. Necessary gain tuning of the shaker power amplifier during initial measurement is required to obtain exactly 100 $mV_{p\text{-}p}$ of reference accelerometer output voltage.

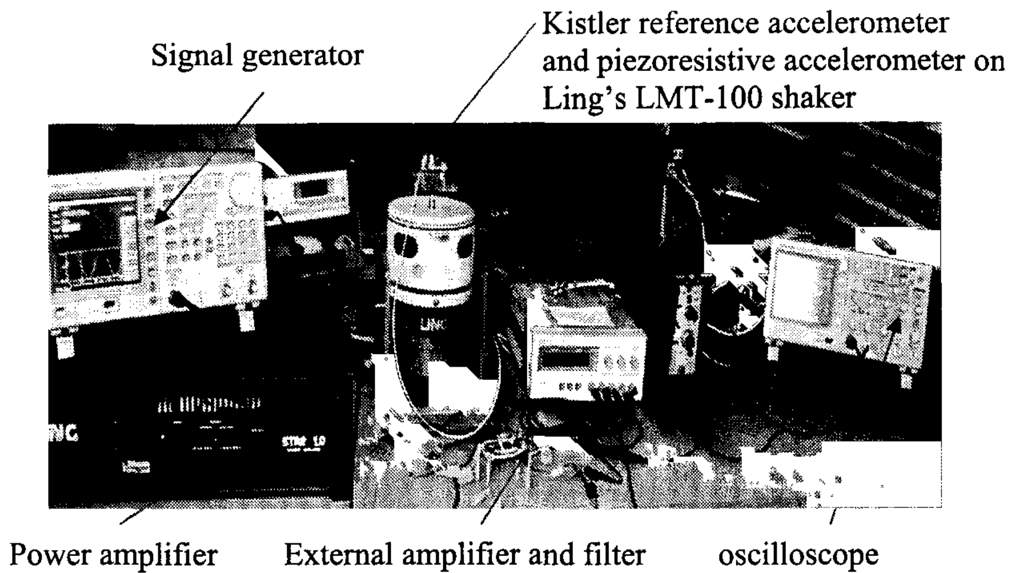

Fig. 5.17. A complete wiring connection of the characterization equipment for piezoresistive accelerometer dynamic test.

With a 3g acceleration applied to the piezoresistive accelerometer, and with the amplification gain of 52 db, the output waveforms of approximately 96 mV_{p-p} is observed as shown in Fig. 5.18. The response of the reference accelerometer is found to be approximately 300 mV_{p-p} at 3g acceleration. Another linear responses of the designed accelerometer with a 52 dB amplifier gain and accelerations from 1g to 7g is shown in Fig. 5.19. From Fig. 5.19, the sensitivity of the accelerometer after amplification is calculated to be approximately 30.7 mV/g and approximately 0.077 mV/g prior to amplification.

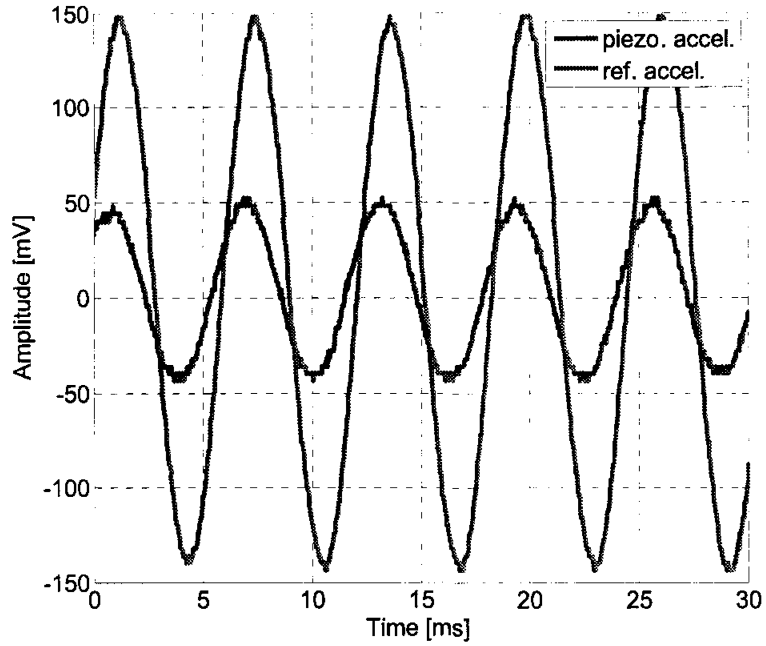

Fig. 5.18. Piezoresistive and reference accelerometers response to 3g acceleration.

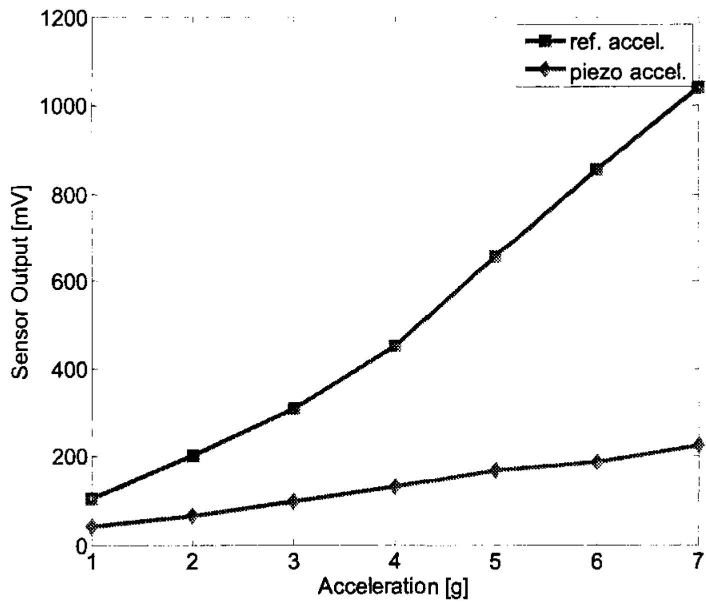

Fig. 5.19. Linear responses of the accelerometer with accelerations from 1g to 7g.

5.3.7 Temperature Test

This section describes the estimation of a temperature coefficient resistance (TCR), α [K^{-1}] of the polysilicon resistor, which is used as the sensing material in the piezoresistive accelerometer. The temperature coefficient is the relative change of a resistance property when the temperature is changed by 1 Kelvin. By knowing the TCR of the polysilicon resistor, the changes of the resistance due to temperature variation can be predicted and compensated. The relationship between the resistance change and TCR is given by

$$R_T = R_{T0}\left(1+\alpha\Delta T\right), \tag{5-9}$$

where R_T is the resistance at temperature T, R_{T0} is the resistance at the reference temperature, and ΔT is the temperature different between T and T_0. To estimate the TCR of the polysilicon resistor, the sensor with its package is placed in the Blue M laboratory oven. At room temperature of approximately 22 °C, the resistance is measured as 1.470 kΩ. The temperature is then gradually increased in the step of 20 °C until 104 °C. Fig. 5.20 and Fig. 5.21 show the resistance change in the sensor due to temperature variations. From this test, the TCR is found to be 2.1×10^{-3} K^{-1} compared to 5.85×10^{-3} K^{-1} that is used during the device design in Chapter Two.

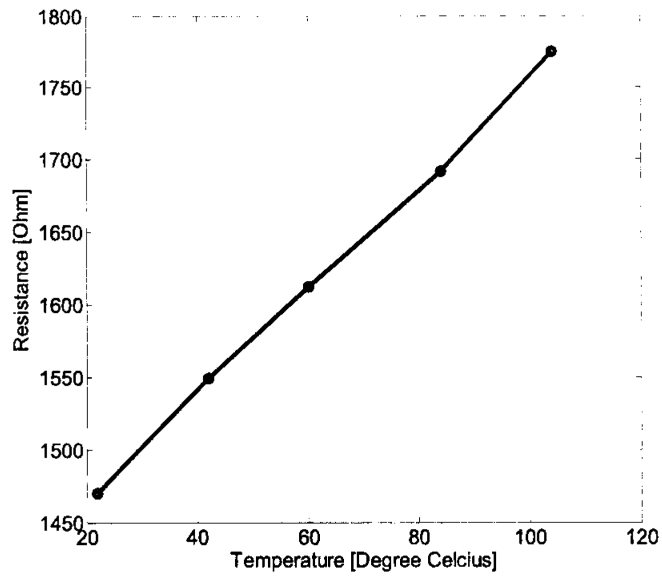

Fig. 5.20. Linear resistance change with temperature from 22°C to 104°C.

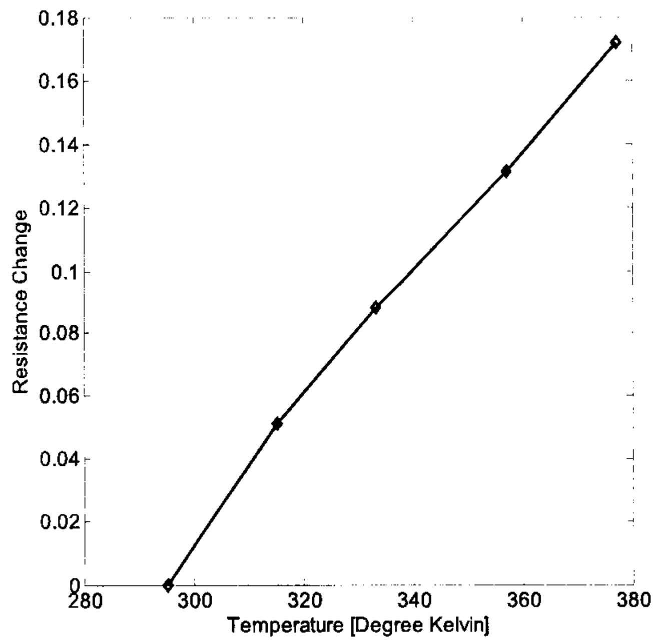

Fig. 5.21. Resistance change with temperature from 295°K to 377°K.

5.3.8 Conclusion

A CMOS-MEMS piezoresistive accelerometer is successfully characterized. The accelerometer is packaged in a standard 16 pins ceramic. Off-chip instrumentation amplifier and a filter circuits have been constructed to amplify and filter the output signal. Resistance measurement, mechanical, off-chip, dynamic, noise, and temperature tests have been conducted for sensor characterization. The resistance of each polysilicon resistor is measured to be approximately 1.4 kΩ. From mechanical test using impulse signal, the resonant frequency of the sensor is found to be approximately 1.34 kHz compared to 1.85 kHz and 1.00 kHz from theoretical calculation and FEA simulation. Through off-chip test, the external amplifier gain is measured as 52 dB. The dynamic test for the acceleration from 1g to 7g is performed on LMT-100 shaker. Sensor's resolution of 30.7 mV/g after amplification and 0.077 mV/g prior to amplification are obtained from the dynamic test. Noise measurement is conducted to analyze sensor performance such as the minimum detectable acceleration by the accelerometer.

Noise signal is measured on HP 2562A dynamic signal analyzer. The overall noise floor is found to be -90 dB V/√Hz (31.6 μV/√Hz) or 1.03 mg/√Hz. The electrical noise is measured as -100 dB V/√Hz (10.0 μV/√Hz) or 0.33 mg/√Hz with no sensor connected to its input. From noise measurement, the mechanical noise is estimated to be 0.98 mg/√Hz. From noise analysis, the minimum detectable acceleration is calculated to be 32.0 mg.

Finally, temperature test is conducted to estimate the temperature coefficient resistance (TCR) of the sensor. The temperature is raised from 20 °C to 104 °C. From the

plot of resistance change versus temperature, the TCR is calculated to be 2.1×10^{-3} K^{-1} compared to 5.85×10^{-3} K^{-1}, which is used during sensor design. Major device performances are obtained from theoretical and experimental and are summarized in Table 5.2. The differences between theoretical and experimental values are due to several factors such as the tolerance of material properties and undercut of the proof mass during post-CMOS microfabrication, which reduce slightly the sensitivity of the sensor.

Table 5.2.

Performance Summary of the Piezoresistive Accelerometer

Parameters	Unit	Designed Value	Tested Value
Polysilicon resistor	kΩ	1.1	1.4
Resonant frequency	kHz	1.00	1.34
Sensitivity prior to amplification	mV/g	91	0.077
Power Consumption	mW	1.00	1.67
Noise floor	mg/√Hz	0.00028	1.03
TCR	K^{-1}	5.85×10^{-3}	2.1×10^{-3}
Minimum detectable acceleration	-	8.74 μg	32.0 mg

5.4 Nano-Newton Force Sensor Characterization

This section discusses the nano-Newton force sensor characterization. Capacitive sensing is performed utilizing MS3110 universal capacitive readout circuit as explained in Section 5.2.3. Additional external instrumentation amplifier and filter with amplification gain of 46 dB is used to further amplify the output waveform. For cleaner output signal, the sensor and its circuitry are placed in the Faraday's cage. The characterization process covers the configuration of the MS3110 universal capacitive readout circuit, the mechanical test for resonant frequency estimation, off-chip external amplifier test for amplification gain determination, noise test analysis to estimate the minimum detectable sensing force, and dynamic test to observe the sensor response to external 1g excitation provided by Piezotronics hand held shaker.

5.4.1 MS3110 Universal Capacitive Board Calibration

MS3310 universal capacitive board reference capacitors, feedback capacitor, gain, and low pass filter cut-off frequency are calibrated prior to sensing measurement. Referring to Appendix B.2, MS3110 board is designed to operate at +5 VDC. Using MS3110 dedicated software, initially; MS3110 chip is required to be reset by pressing the 'CHPRST' button. Using 'Voltage reference trim', the reference bias voltage at pin V2P25 is adjusted to 2.25 V + 0.01 V. The biasing current is set by varying the 'Current reference trim' to be approximately 10 μA, which can be measured across jumper J9. The last biasing setting is the oscillator frequency, which can be tuned by using the 'Oscillator trim' and is measured at pin 1 of J3. The oscillator frequency is set to be approximately 2.25 V, 100 kHz ± 5 kHz as shown in Fig. 5.22. Next step is the gain setting of the

MS3110 amplifier. To verify that the board is working properly, the output buffer gain is set to 2, IAMP feedback capacitance, CF to 5.130 pF, IAMP balance capacitance, CS1 and CS2 to 0 pF. The output voltage, V_{OUT} at pin TP5 is measured to be 2.25 V as calculated using Eqn. (5-4). The balance capacitance, CS1 and CS2 have to be varied prior to capacitive measurement so that the output voltage, V_{OUT} at TP5 is always below 2.25 V to avoid saturation.

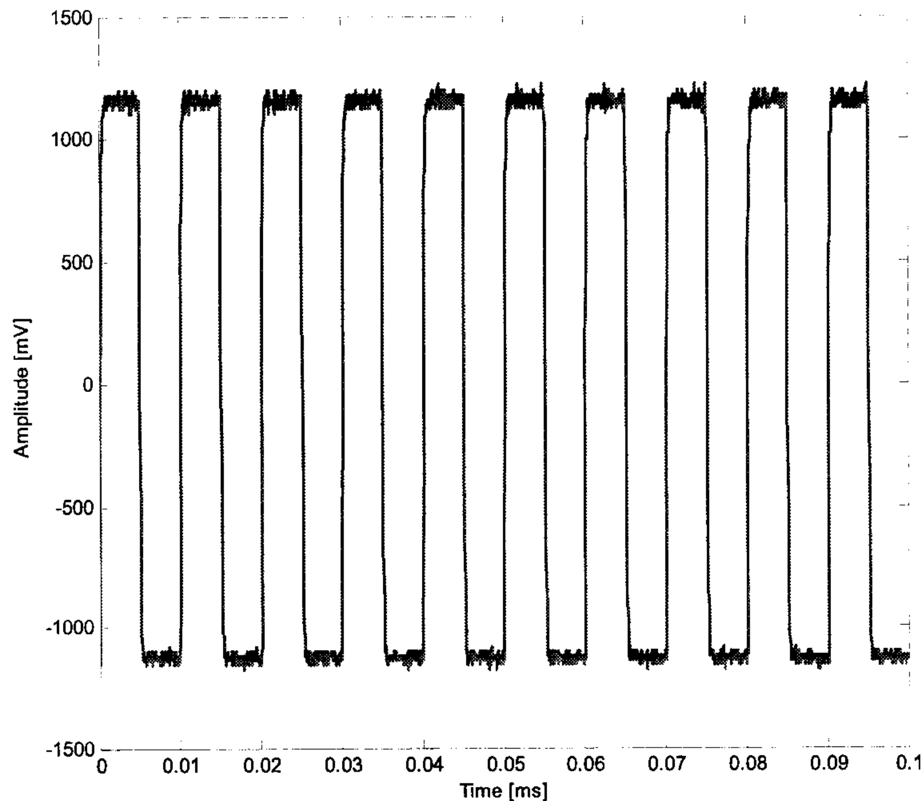

Fig. 5.22. MS3110 board oscillator frequency.

5.4.2 Mechanical Test

Mechanical test for the nano-Newton force sensor is performed to estimate the resonant frequency of the device. An impulse signal as shown in Fig. 5.23 is applied to the sensor to obtain a frequency sweep. The data captured by the oscilloscope is processed in Matlab, which convert the time domain signal to the frequency domain signal using fast Fourier transform (FFT). The dynamic output frequency response of the sensor is illustrated in Fig. 5.24, which indicates the resonant frequency of the sensor at approximately 1.0 kHz.

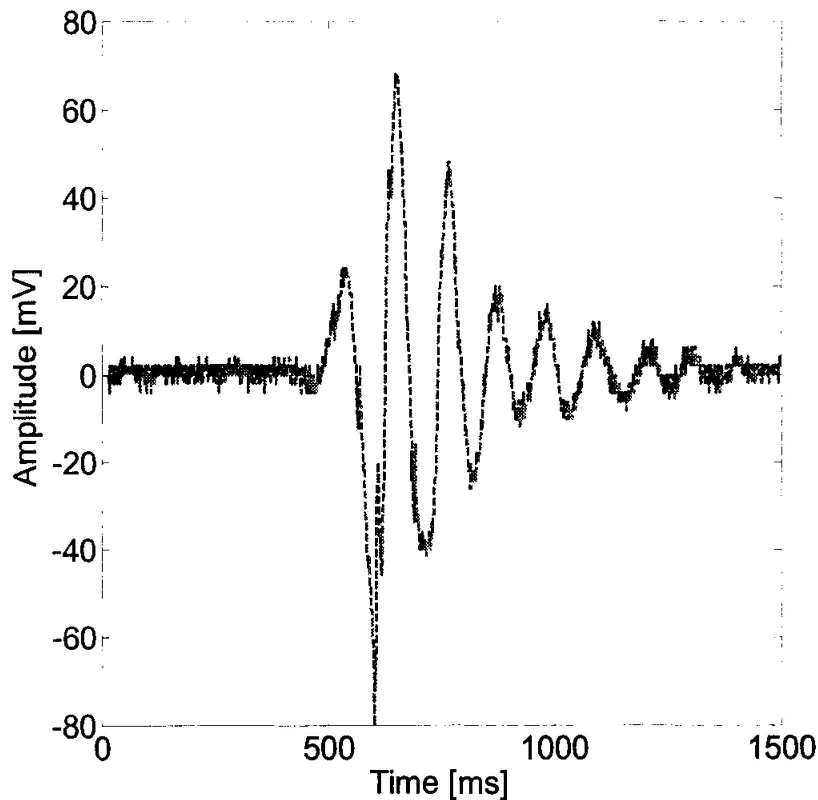

Fig. 5.23. Impulse signal applied to the sensor.

The resonant frequency which was obtained through experimental method at 1.0 kHz is closed to the analytical and FEA methods, which estimate the resonant frequency of the sensor at 1.6 kHz and 1.22 kHz. The differences are due to the actual thickness variation and slight undercut of the single-crystal silicon (SCS) proof mass during the post-CMOS microfabrication process.

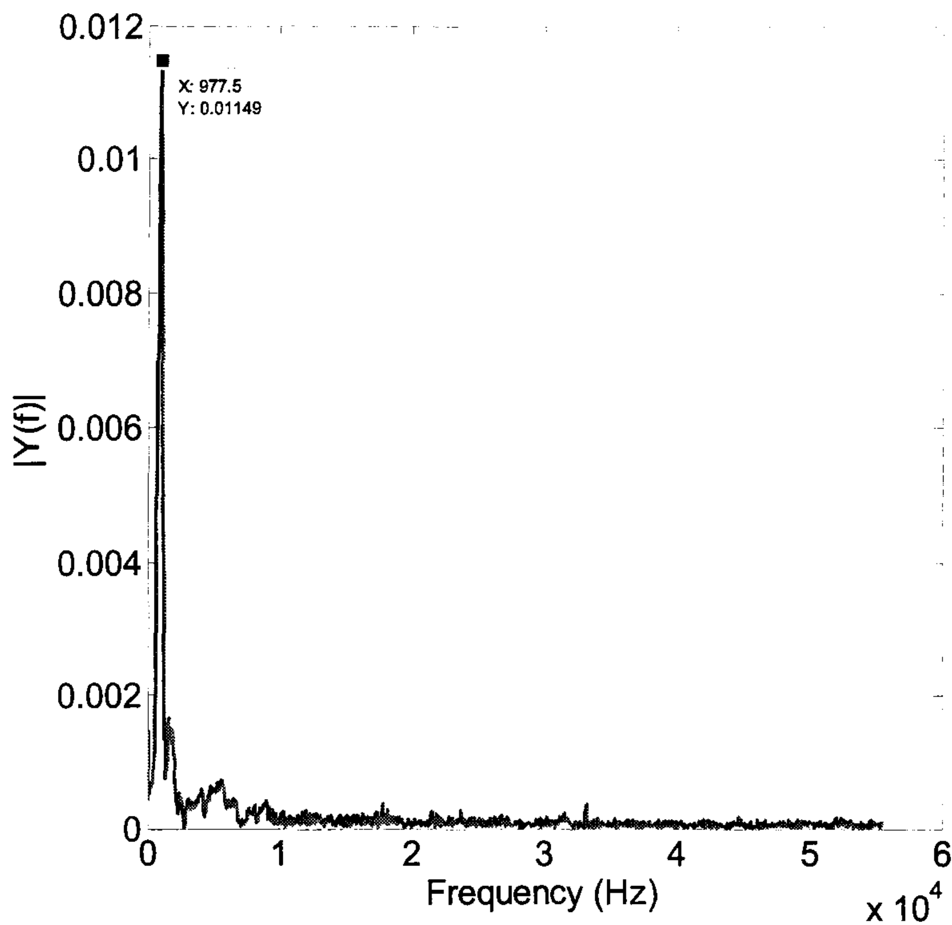

Fig. 5.24. Dynamic frequency response of the sensor with impulse signal.

5.4.3 Off-Chip Circuit Test

Off-Chip circuit test is conducted to obtain the performance of the instrumentation amplifier and the filter circuits as shown in Fig. 5.25. A dc voltage of ±15 V is used as the power supply for the AD 627 amplifier integrated circuit (IC), while a 5 V DC is used for the voltage divider circuit at the second amplifier input for offset cancelation purposes. To check the performance of the circuit, no sensor is connected at the input. Instead, the input signal of 12.5 mV in amplitude is supplied by the signal generator. The amplifier gain is found be approximately46 dB with the low pass filter cut-off frequency of 2.0 kHz.

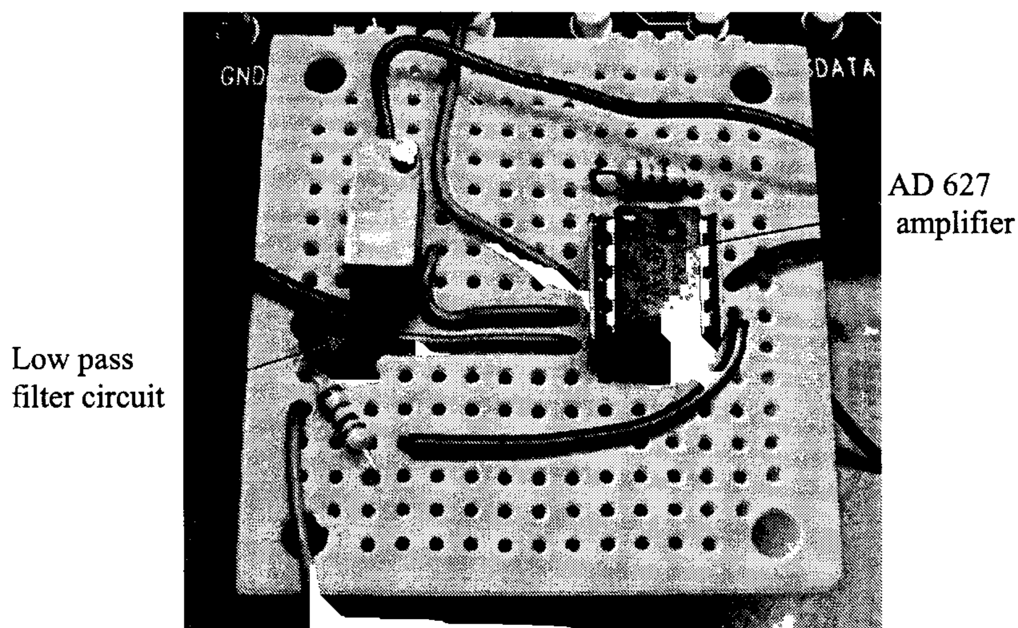

Fig. 5.25. External amplifier and filter circuits.

5.4.4 Dynamic Test

The dynamic test for the nano-Newton force sensor is performed on the Kistler 1g hand held shaker. The test setup is as shown in Fig. 5.26, which shows the complete equipment wiring connection and the DUT on the shaker. The test conducted is for sensor waveform observation at 1g acceleration. Similar to the piezoresistive accelerometer setup, Kistler's hand held shaker operates at ~160 Hz, for 1g acceleration. Capacitive change produces by the sensor is sensed by the MS3110 capacitive readout circuit and the output signal is further amplified and filtered by the 46 dB gain, 2 kHz cut-off frequency of the AD 627 external amplifier and a low pass filter circuits.

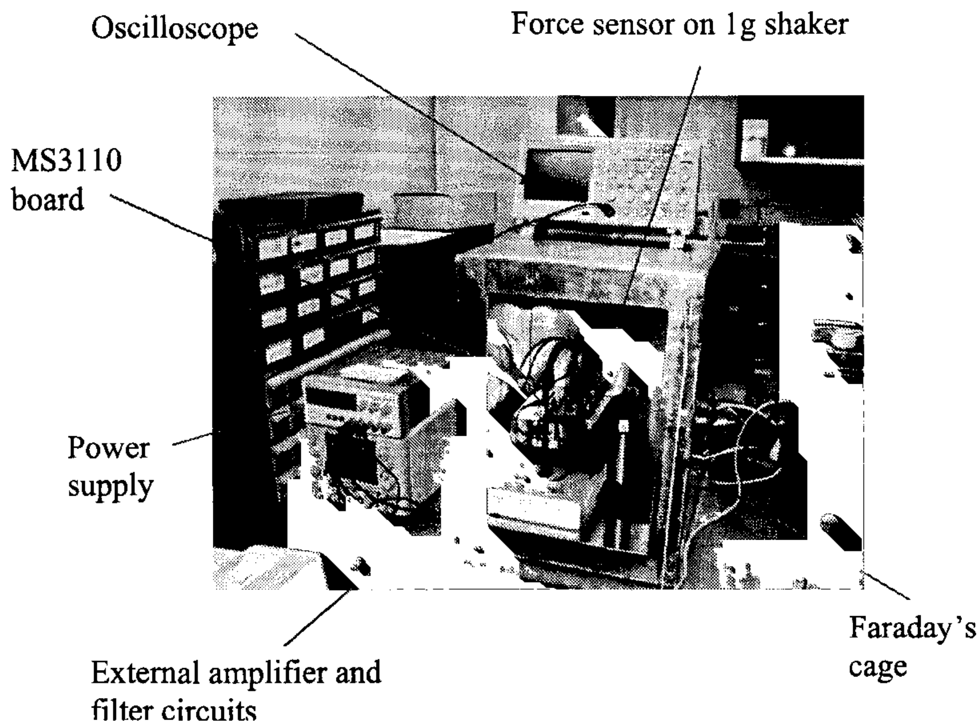

Fig. 5.26. A complete wiring connection of the characterization equipment for the nano-Newton force sensor dynamic test.

A necessary tuning is required for the CS1 and CS2 balance capacitors to avoid the output signal from saturated. As shown in Fig. 5.27, at 1g acceleration, the output waveform of approximately 1.6 V_{p-p} is observed on the oscilloscope. To check on whether the output signal actually comes from the sensor and not from coupling effects, the sensor is removed from its socket and a 1g acceleration is applied using handheld shaker to the sensor's printed circuit board. The output of this response is shown in Fig. 5.28, which clearly shows no output from the amplifier circuit as observed on the oscilloscope.

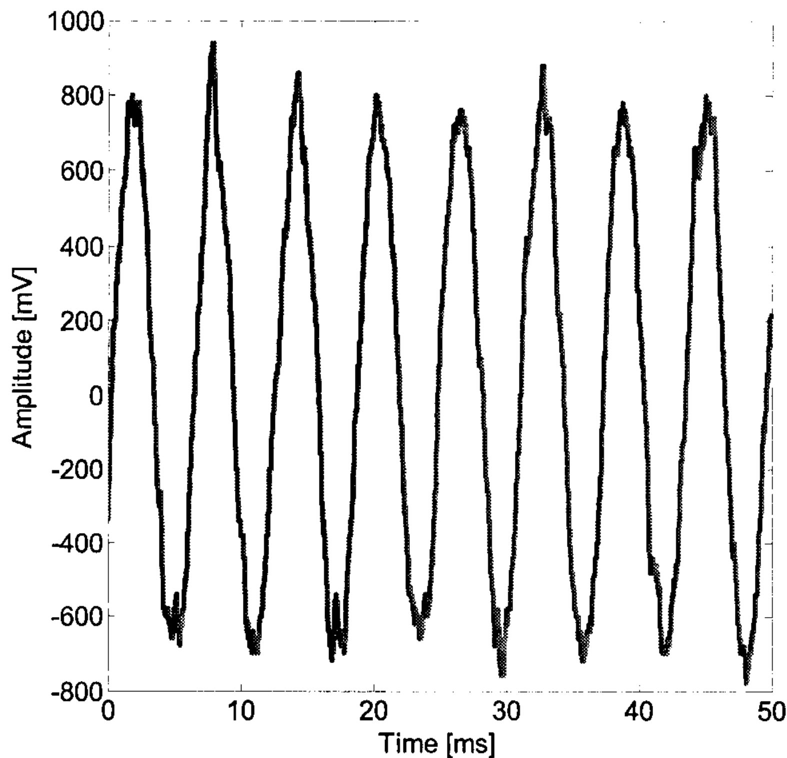

Fig. 5.27. Nano-Newton force sensor response to 1g acceleration.

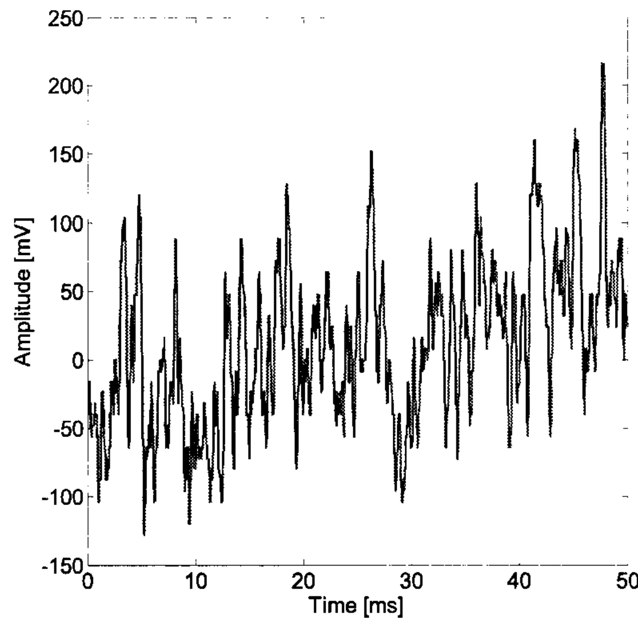

Fig. 5.28. Response of the amplifier and filter circuits with no sensor input.

5.4.5 Noise Measurement

Noise analysis for the nano-Newton force sensor is conducted on HP 2562A dynamic signal analyzer. As explained in Section 5.3.5, the overall noise floor consists of the mechanical and the electrical (circuit) noises. With the signal analyzer frequency span set to 800 Hz and the average of 10 for each frequency, the overall noise floor is found to be approximately -60 dB V/√Hz or 1.0 mV/√Hz as shown in Fig. 5.29.

The electrical or circuit noise is found to be -75 dB V/√Hz or 0.18 mV/√Hz, which can be measured from the output of the amplifier circuit when no sensor is connected to the input. The sensitivity prior to amplification, S is determined as 8 mV/g from the dynamic test.

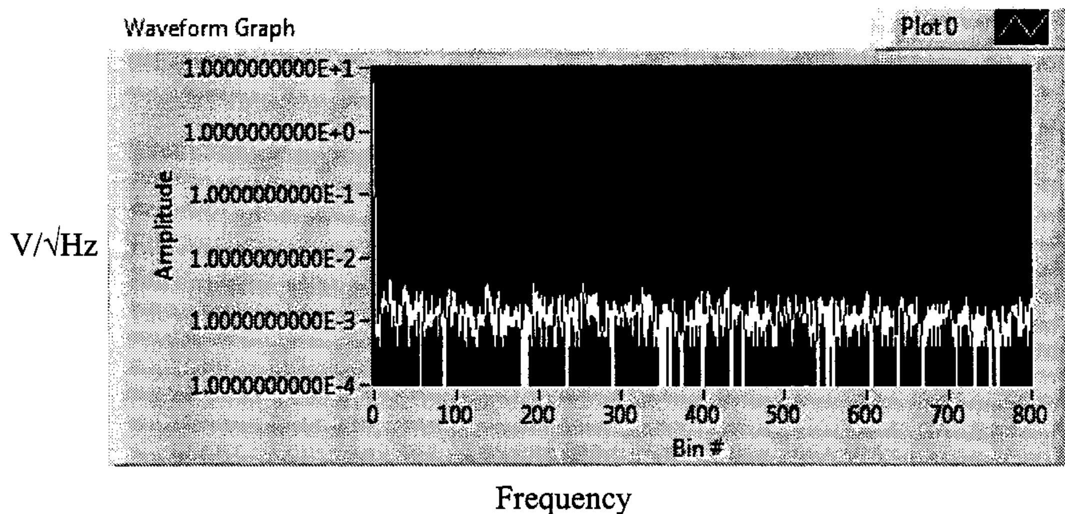

Fig. 5.29. Overall noise of the system, which consists of the sensor and amplifier and filter circuits.

At 46 dB gain of off-chip amplifier, the electrical input-referred noise is calculated as 0.89 mV/√Hz. With a sensitivity of 1.6 V/g after amplification, the total noise is 0.63 mg/√Hz. Using the sensitivity, which was previously determined, the electrical noise is calculated using Eqn. (5-7) as 0.11 mg/√Hz. From the overall noise and electrical noise analysis, the mechanical noise is therefore calculated as 0.62 mg/√Hz. Choosing the bandwidth of 1 kHz, the minimum detectable acceleration is found to be 19.8 mg. At 1g, the point force calculated at sensor center of mass is 449 nN.

5.4.6 Conclusion

A CMOS-MEMS nano-Newton force sensor is successfully characterized. The force sensor is packaged in a standard 16 pins ceramic DIP with 10 package leads removed for ease sensor deployment. MS3110 universal capacitive readout circuit is used

for half-bridge capacitive sensing. External amplifier (AD 627) and a low pass filter are utilized to further amplify and filter the output signal from MS3110 board. To improve the quality of the output signal and for noise suppression, force sensor and its circuitries are placed in the Faraday's cage. Mechanical, off-chip, dynamic, and noise tests have been performed for sensor characterization. From the mechanical test using impulse signal, the resonant frequency of the sensor is found to be approximately 1.0 kHz compared to 1.6 kHz and 1.22 kHz from the theoretical calculation and FEA simulation. Through off-chip test, the external amplifier gain is found to be 46 dB with the low pass filter cut-off frequency of 2.0 kHz. The dynamic test is performed at 1g on Kistler's hand held shaker. The resolution of 1.6 V/g and 8 mV/g prior to amplification are obtained from the dynamic test. Finally noise measurement is conducted to estimate sensor performance such as the minimum detectable force by the sensor. Noise signal is measured on HP 2562A dynamic signal analyzer. From this analysis, the overall noise floor is found to be -60 dB V/√Hz (1.0 mV/√Hz) or 0.63 mg/√Hz. The electrical noise is measured as -75 dB V/√Hz (0.18 mV/√Hz) or 0.11 mg/√Hz with no sensor connected to its input. From previous analysis, the mechanical noise is estimated to be 0.62 mg/√Hz. From noise analysis, the minimum detectable acceleration is calculated to be 19.8 mg. The major device performance is summarized in Table 5.3.

Table 5.3.

Performance Summary of the Nano-Newton Force Sensor.

Parameters	Unit	Designed Value	Tested Value
Resonant frequency	kHz	1.60	1.00
Sensitivity	-	0.02 fF/nN	8 mV/g
Noise floor	-	0.275 pN/√Hz	0.63 mg/√Hz
Min detectable force	-	8.7 pN	19.8 mg 449 nN (at 1g)

CHAPTER SIX

CONCLUSIONS AND SUGGESTIONS FOR FUTURE RESEARCH

6.1 Overall Conclusions

Two new CMOS-MEMS devices; a piezoresistive accelerometer with large proof mass and a nano-Newton force sensor have been successfully designed, fabricated, and characterized. Both devices are fabricated using AMI (ON Semiconductor) 0.5 μm CMOS technology through MOSIS. Device design utilizes dedicated software such as Matlab, CoventorWare, and Mentor Graphic layout editor. A customized post-CMOS microfabrication process for device release is conducted at Lurie Nano Fabrication Facility (LNF), University of Michigan, Ann Arbor. Device characterizations are performed at Oakland University MEMS/NEMS research lab to investigate device performance.

A piezoresistive accelerometer is suitable for low g applications with out-of-plane sensing ranges from 1g to 10g. Common issues associated with most of the CMOS-MEMS thin film accelerometers such as structural curling and low sensitivity have been solved by incorporating SCS as the proof mass. The four bimorph beams attached to the sensor structure has significantly improved sensor stability by allowing sorely the out-of-plane motion (*z*-axis) of the proof mass for larger piezoresistive effect while minimizing in-plane (*x*, *y*-axis) motions. Multiple CMOS metal layers permit flexible on-chip sensor element wiring for full Wheatstone bridge configuration, which further increase sensor sensitivity. Using DRIE post-CMOS microfabrication process, the single-crystal silicon

substrate (device proof mass) is anisotropically etched up to approximately 40 μm thickness during back-side processing. Daktek surface profilometer is used to estimate the proof mass thickness. The front-side RIE processing of the chip is employed to remove the BPSG and the silicon dioxide (SiO_2) layers in the trenches followed by the anisotropic and isotropic DRIE to successfully release the sensor structure. Post-CMOS processes require careful parameter tuning such as etching and passivation rate, R.F power, and etching time for a successful device release. With a nominal sheet resistance, ρ_s of 26.1 Ω/□ from AMI 0.5 μm CMOS technology, each polysilicon resistor exhibits a resistance of approximately 1.4 kΩ. From device characterization, the resonant frequency of the accelerometer is found to be 1.34 kHz. With a 52 dB external amplifier gain, the accelerometer resolution is 30.1 mV/g after amplification and 0.077 mV/g prior to amplification. Noise analysis is conducted to estimate the minimum detectable acceleration. The total noise floor of the system is 1.03 mg/√Hz with the electrical noise is estimated at 0.33 mg/√Hz and the mechanical noise at 0.98 mg/√Hz. The minimum detectable acceleration is therefore calculated to be 32 mg. Finally the TCR of the accelerometer is found to be 2.1×10^{-3} K^{-1} from the temperature analysis.

A capacitive CMOS-MEMS force sensor capable of nano-Newton measurement is also fabricated. The unique out-of-plane sensing mechanism allows sensing of forces applied perpendicular to the sensor plane. The device robustness is enabled by the inclusion of SCS as sensor structure. This will allow for a reliable deployment in force measurement. The wide force measurement range of nN to mN makes the force sensor suitable for many biomedical applications. Using similar post-CMOS microfabrication

process as the accelerometer, initially a DRIE is used to anisotropically etch the silicon substrate up to approximately 40 μm thickness. The front-side RIE processing of the chip is then performed to remove the BPSG and the silicon dioxide (SiO_2) layers in the trenches followed by the anisotropic DRIE to successfully release the sensor structure. From device characterization, the resonant frequency of the force sensor is found to be 1.0 kHz. With a 46 dB external amplifier gain, the force sensor resolution is 1.6 V/g after amplification and 8 mV/g prior to amplification. Noise analysis is conducted to estimate the minimum detectable force. The total noise floor is 0.63 mg/√Hz with the electrical noise is estimated at 0.11 mg/√Hz and mechanical noise at 0.62 mg/√Hz. The minimum detectable acceleration is calculated to be 19.8 mg. At 1g acceleration, the point force calculated at sensor center of mass is 449 nN.

An observer-based controller for the nano-Newton actuator system is also designed and simulated to provide a control of the sensor structure. The sensor features an out-of-plane force measurement in *z*-direction. However, due to the structure of the device and thin beams, unpredictable in-plane movements in the *x-y* plane can cause undesirable measurement error or even damage the sensor in severe cases. This research proposes a solution to the problem by incorporating observer-based controller to regulate the in-plane movements during the measurement process. A nonlinear controller is designed using input-state and input-output feedback linearization techniques. Based on the observation, the input-output feedback linearization offers easier linearization process compared to the input-state method. The state estimation which is required for on-line, real-time feedback control is implemented by the nonlinear exact error linearization technique. Simulation result shows that the observer-based controller implementation for

the nano-Newton actuator system performed exceedingly well and effectively by providing fast controlling action in less than 10 ms. This approach for stabilizing the sensor measurement is found to be practical and effective.

6.2 Suggestions for Future Research

A new low-cost, maskless, and easy post-CMOS microfabrication of the CMOS-MEMS devices have been successfully demonstrated as discussed in previous section. The future research involves the following suggestions to improve sensor performance and reliability:

- The monolithic integration of the on-chip amplifier and filter circuits for better signal conditioning while minimizing the parasitic effect, the electrical noise, and the external noises;
- Proper sensor location during layout design for easy post-CMOS microfabrication processing;
- The integration of actuator system in force sensor structure for control implementation to solve any undesired in-plane twisting motion;
- Proper sensor packaging for ease sensor deployment;

APPENDIX A

MICROELECTROMECHANICAL THEORY

A.1 Pure Bending of a Transversely Loaded Beam

Fig. A.1 shows a small section of the beam that bent due to the application of a transverse load [51]. The positive direction of z is in downward direction. M_o is the applied moment, while the radius of curvature is R_C. A differential angular $d\theta$ is assumed to have an axial length dx when not bent. The dashed arc in the middle of the beam is called the neutral axis.

The length of the dashed segment at position z is given by

$$dL = \left(R_C - z\right) d\theta, \tag{A-1}$$

and when the beam is not bending, at the position of the neutral axis, the length corresponding to that segment is equal to dx, the differential length and is given by

$$dx = R_C d\theta, \tag{A-2}$$

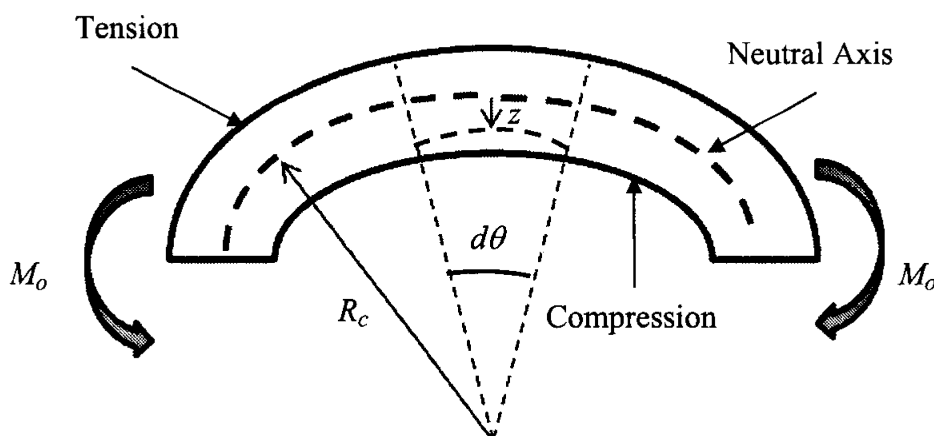

Fig. A.1. A segment of a beam in pure bending.

and the different in axial length is

$$\delta = (R_c - z)d\theta - R_c d\theta = -zd\theta . \tag{A-3}$$

From Eqn. (A-2) and Eqn. (A-3), the axial strain and stress is therefore given by

$$\varepsilon_x = -\frac{zd\theta}{R_c d\theta} = -\frac{z}{R_c}, \text{ and } \sigma_x = -\frac{zE}{R_c}, \tag{A-4}$$

where E is the Young's modulus of the material. Using Eqn. (A-4), the total internal bending moment, M can be derived as

$$M = -\int_{-H/2}^{H/2} \frac{EWz^2}{R_c} dz = -\left(\frac{1}{12}WH^3\right)\frac{E}{R_c}, \tag{A-5}$$

where W and H are the width and thickness of the beam. In another form Eqn. (A-6) can be represented as

$$\frac{1}{R_c} = -\frac{12M}{WH^3E} = -\frac{M}{EI}, \tag{A-6}$$

where I is the moment of inertia.

A.2 Differential Equation for Beam Bending

An example of the bending cantilever is shown in Fig. A.2. The increment of beam length, ds along the neutral axis is related to dx and is given by

$$ds = \frac{dx}{\cos\theta}. \tag{A-7}$$

The slope of the beam from the neutral axis is

$$\frac{dw}{dx} = \tan\theta \tag{A-8}$$

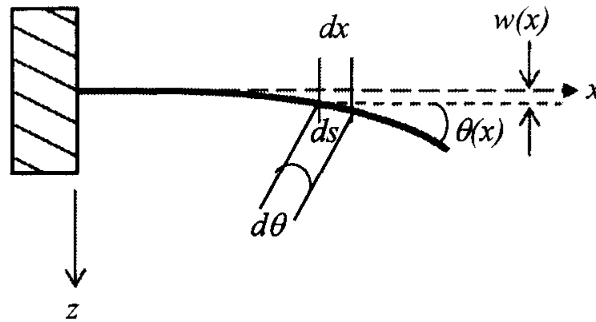

Fig. A.2. A bent cantilever beam.

while the relationship between ds and the incremental subtended angle $d\theta$ is given by

$$ds = R_c d\theta. \tag{A-9}$$

Since the angle generated by most of the MEMS devices are small, we can assume that $ds \approx dx$. Eqn. (A-8) and Eqn. (A-9) can therefore be assumed as

$$\frac{d\theta}{dx} \approx \frac{1}{R_c}, \tag{A-10}$$

and

$$\theta \approx \frac{dw}{dx}. \tag{A-11}$$

Differentiate Eqn. (A-11) twice and substitute Eqn. (A-10) into the result of Eqn. (A-11) yields

$$\frac{1}{R_c} = \frac{d^2 w}{dx^2}. \tag{A-12}$$

Using Eqn. (A-6) obtains from Section A.1, yield the differential equation for a small-angle bending beams:

$$\frac{d^2w}{dx^2} = -\frac{M}{EI}. \qquad \text{(A-13)}$$

The internal moment at any position x within the beam is $M = -F(L - x)$. Using Eqn. (A-13), this leads to the second-order differential equation of

$$\frac{d^2w}{dx^2} = \frac{F}{EI}(L - x) \qquad \text{(A-14)}$$

APPENDIX B

CHIP DIAGRAM AND INSTRUMENT SPECIFICATION

B1 Chip pin-out connection and its labels that include the on-chip wiring connection

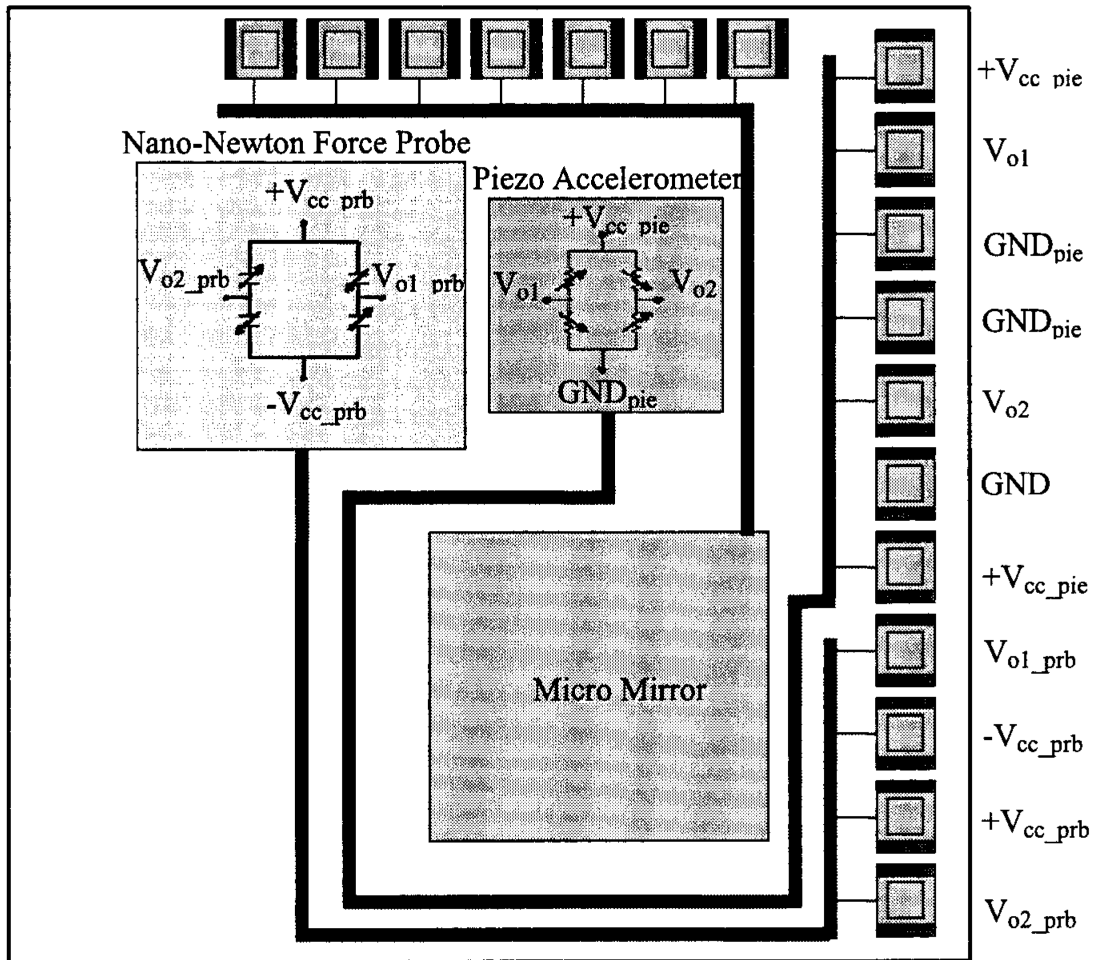

Fig. B.1. The schematic diagram of the chip pin-out connection.

B.2 MS3110 Universal Capacitive Readout schematic diagram

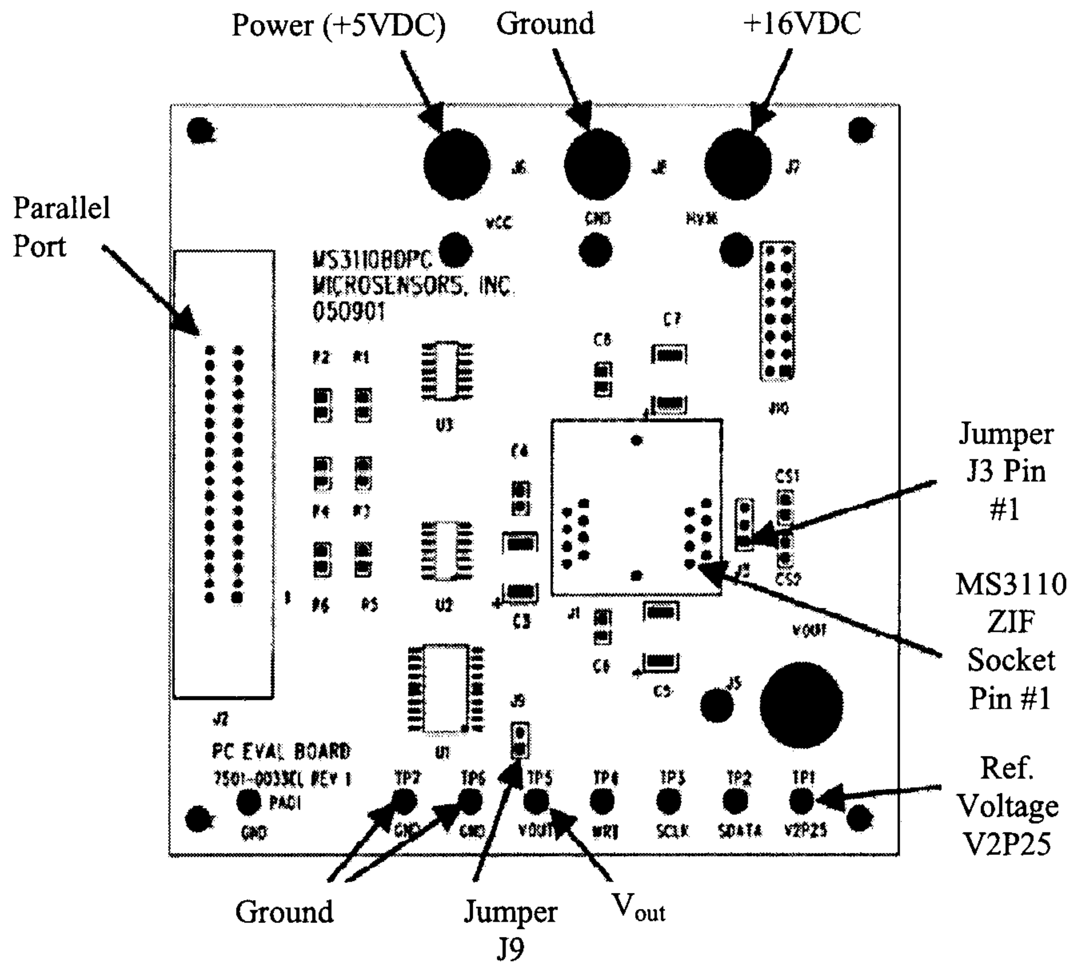

Fig. B.2. The schematic diagram of the MS3110 universal capacitive readout circuit.

REFERENCES

[1] Charles S. Smith, "Piezoresistance Effect in Germanium and Silicon", *Physical Review*, Vol. 94, No. 1, 1954.

[2] Harvey C. Nathanson, William E. Newell, Robert A. Wickstrom, and John Ransford Davis Jr., "The Resonant Gate Transistor", *IEEE Transaction On Electron Devices*, Vol. ED-14, No. 3, March 1967.

[3] Chang Liu, *Foundation of MEMS*, Pearson Education, Inc, New Jersey, 2006.

[4] K. E. Petersen, "Fabrication of an Integrated, planar Silicon ink-jet Structure", *IEEE Transaction on Electron Devices*, Issue 12, Dec 1979, pp. 1918-1920.

[5] Long-Sheng Fan, Yu-Chong Tai, and R.S. Muller, "IC-Processed Electrostatic Micro-Motors", *International Electron Devices Meeting*, IEDM '88, 1988, pp. 666-669.

[6] U. A. Dauderstadt, P. H. S. de Vries, R. Hiratsuka, J. G. Korvink, P. M. Sarro, H. Baltes, and S. Middelhoek, "Silicon accelerometer based on thermopiles", *Sensors and Actuators A: Physical*, Vol. 46, Issue 1-3, Jan-Feb 1995, pp. 201-204.

[7] Sangwoo Lee, Sangjun Park, Jongpal Kim, Sangchul Lee, and Dong-il, "Surface/Bulk Micromachined Single-Crystalline-Silicon Micro Gyroscope", *Journal of MEMS*, Vol. 9, No. 4, December 2000, pp. 557-567.

[8] Han J. G. E. Gardeniers et al., "Silicon Micromachined Hollow Microneedles for Transdermal Liquid Transport", *Journal of MEMS*, Vol. 12, No. 6, December 2003, pp. 85-862.

[9] Sami Youssef, Jean Podlecki, Roy Al Asmar, Brice Sorli, Oliver Cyril, and Alain Foucaran, "MEMS Scanning Calorimeter With Serpentine-Shaped Platinum Resistors for Characterizations of Microsamples", *Journals of MEMS*, Vol. 18, No. 2, April 2009, pp. 414-423.

[10] Jong-Man Kim, Jae-Hyoung Park, Change-Wook Baek, and Yong-Kweon Kim, "Design and Fabrication of SCS(Single Crystalline Silicon) RF MEMS Switch Using SiOG Process", *17th IEEE International Conference on MEMS*, 2004, pp. 785-788.

[11] Baltes, Brand, Fedder, Hierold, Korvink, and Tabata, *CMOS-MEMS*, Wiley-VCH Verlag GmbH & Co., KGaA, Weinheim, Germany, 2005.

[12] J. M. Bustillo, R. T. Howe, R. S. Muller, "Surface micromachining for microelectromechanical systems", *Proceeding IEEE*, 1998, 86, pp. 1552 – 1574.

[13] J. Smith, S. Montague, J. Sniegowski, J. Murray, P. McWhorter, "Embedded micromechanical devices for the monolithic integration of MEMS with CMOS", *Proeeding IEEE IEDM '95*, 1995, pp. 609-612.

[14] Analog Devices, Norwood, MA, http://www.analog.com/imems/.

[15] Infineon Technologies, Munich, Germany, http://www.infineon.com/sensors/.

[16] Freescale Semiconductor, Austin, TX, http://www.freescale.com/.

[17] O. Brand, H. Baltes, "CMOS-based microsensors and packaging", *Sens. Actuators A* 2001, 92, 1-9.

[18] H. Baltes, O. Brand, A. Hierlemann,D. Lange, C. Hagleitner, "CMOS-MEMS – Presence and future", In: *Proceeding IEEE Micro Electro Mechanical Systems* 2002 (*MEMS* 2002); 2002, pp. 459-466.

[19] G. T. A. Kovacs, N. I. Maluf, K. E. Petersen, "Bulk micromachining of silicon", *Proceeding of IEEE* 1998, 86, 1536-1551.

[20] P. F. Van Kessel, L. J. Hornbeck, R. E. Meier, M. R. Douglass, "A MEMS-based projection display ", *Proceeding IEEE* 1998, 86, 1687-1704.

[21] C. W. Storment, D. A. Borkholder, V. Westerlind, J. W. Sun, N. I. Maluf, G. T. A. Kovacs, "Flexible, dry-released process for aluminum electrostatic actuators", *Journal of Microelectromechanical Systems*, 1994, 3, 90-96.

[22] Jiangfeng Wu, Gary K. Fedder, and L. Richard Carley, "Amplifier for a 50-μg/√Hz Monolithic CMOS MEMS Accelerometer", *IEEE Journal of Solid-State Circuits*, Vol. 39, No. 5, May 2004, pp. 722-730.

[23] Chih-Ming Sun, Ming-Han Tsai, and Weileun Fang, "Design and Implementation of a Novel CMOS-MEMS Single Proof-Mass Tri-Axis Accelerometer", *IEEE 2009 22nd International Conference on MEMS*, Jan 2009, pp. 809-812.

[24] Young-Sik Kim, et al., "Thermo-piezoelectric Si3N4 cantilever array on CMOS circuit for high density probe-based data storage", *Sensor and Actuator A: Physical*, Vol. 135, Issue 1, March 2007, pp. 67-72.

[25] V. Beroulle, Y. Bertrand, L. Latorre, and P. Nouet, "Monolithic Piezoresistive CMOS Magnetic Field Sensors", *Sensor and Actuator A: Physical*, Vol. 103, Issue 1-2, Jan 2003, pp. 23-32.

[26] G. Villanueva, et al., "Piezo Cantilevers in a commercial CMOS technology For Intermolecular Force Detection", *Microelectronic Engineering*, Vol. 83, April- Sep. 2006, pp. 1302-1305.

[27] A. A. Barlian, W. T. Park, J. R. Mallon, A. J. Rastegar, and B. L. Pruitt, "Review: Semiconductor Piezoresistance for Microsystems", *Proceeding Of IEEE*, Vol. 97, 2009, pp. 513-552.

[28] A. Chaehoi, L. Latorre, P. Nouet, and S. Baglio, "Piezoresistive CMOS Beams for Inertial Sensing", *Proceeding of IEEE Sensors*, Vol. 1, 2003, pp. 451-456.

[29] J. A. Plaza, A. Collado, E. Cabruja, and J. Esteve, "Piezoresistive Accelerometer for MCM Package", *Journal of MEMS*, Vol. 11, 2002, pp. 794-801.

[30] E. Kruglick, B. A. Warneke, and K. S. J. Pister, "CMOS 3-axis Accelerometer with Integrated Amplifier", *MEMS 1998 Proceeding*, 1998, pp. 631-636.

[31] H. Xie, L. Erdmann, X. Zhu, K. J. Gabriel, and G. K. Fedder, "Post-CMOS processing for high-aspect-ratio integrated silicon microstructures," *J. of MEMS*, Vol. 11 , 2002, pp. 93-101.

[32] H. Qu and H. Xie, "Process Development for CMOS-MEMS Sensors With Robust Electrically Isolated Bulk Silicon Microstructures," *J. of MEMS*, Vol. 16, 2007, pp. 1152-1161.

[33] S. Kal, S. Das, D. K. Maurya, K. Biswas, A. Ravi Sankar, and S. K. Lahiri, "CMOS compatible bulk micromachined silicon piezoresistive accelerometer with low off-axis sensitivity", Microelectronics Journal 37(2006), 2006, pp. 22-30.

[34] Kathleen A. Schmitz, et al., "Measurement of the Force Produced by an Intact Bull Sperm Flagellum in Isometric Arrest and Estimation of the Dynein Stall Force", *Biophysical Journal Volume 79*, July 2000, pp. 468–478.

[35] M. J. Moritz, et al., "Measurement of the Force and Torque Produced in the Calcium Response of Reactivated Rat Sperm Flagella", *Cell Motility and the Cytoskeleton* 49:33–40 (2001).

[36] F. Beyeler, et al., "Monolithically Fabricated Microgripper With Integrated Force Sensor for Manipulating Micro objects and Biological Cells Aligned in an Ultrasonic Field", *Journal of Microelectromechanical Systems*, Vol. 16, No. 1, pp. 7-15 (2007).

[37] Y. Sun, et al., "Characterizing Fruit Fly Flight Behavior Using a Microforce Sensor With a New Comb-Drive Configuration", *Journal of Microelectromechanical Systems*, Vol. 14, No.1, 2005, pp. 4-11.

[38] D. Fang, et al., "A 1mW Dual-Chopper Amplifier for a 50-µg/√Hz Monolithic CMOS-MEMS Capacitive Accelerometer," *Digest of Technical Papers of 2006 Symposium on VLSI Circuits,* Honolulu, HI, Jun. 15-17, pp.59 - 60, 2006.

[39] H. Qu, et al., "An Integrated Fully-Differential CMOS-MEMS Z-axis Accelerometer Utilizing a Torsional Suspension", *Proc. Of the 3rd IEEE Int. Conf. on Nano/Micro Eng. And Molecular Sys.*, 2008, pp. 1063-1066.

[40] Y. Sun et al, "Actively Servoed Multi-Axis Microforce Sensors", *Int. Conf. on Robotic & Automation*, Taipei, Taiwan, Sep. 2003, pp. 294-299.

[41] E. T. Enikov, and B. J. Nelson, "Three-dimensional Microfabrication for a Multi-degree-of-freedom capacitive force sensor using fibre-chip coupling", *J. Micromechanical and Microengineering*, 10(2000), page (1-6).

[42] Keekyoung Kim, Xinyu Liu, Yong Zhang, and Yu Sun, "MicroNewton Force-Controlled Manipulation of Biomaterial Using a Monolithic MEMS Microgripper with Two-Axis Force Feedback", *IEEE International Conf. on Robotic and Automation*, Pasadena, CA, USA, 2008, pp. 3100-3105.

[43] Reza Saeidpourazar and Nader Jalili, "Microcantilever-Based Force Tracking With Applications to High-Resolution Imaging and Nanomanipulation", *IEEE Transaction on Industrial Electronics*, Vol. 55, No. 11, Nov. 2008, pp. 3935-3943.

[44] J.H. Yi, K. H. Park, S.H. Kim, Y.K. Kwak, M. Abdelfatah, "Robust Force Control For A Magnetically Levitated Manipulator Using Flux Density Measurement", *Control Eng. Practice*, Vol. 4, No 7, 1996, pp. 957-965.

[45] Chuanwei Wang, Hung-Hsiu Yu, Mingching Wu, Weileun Fang, "Implementation of phase-locked loop control for MEMS scanning mirror using DSP", *Sensor and Actuators*, A 133, 2007, pp. 243-249.

[46] P.B. Chu and S.J. Pister, "Analysis of closed-loop control of parallel-plate electrostatic microgripper", *Robotic and Automation*, Vol. 1, 1994, pp. 820-825.

[47] Joshua Israelsohn, Technical Editor, EDN, http://www.edn.com/article/CA472836.html, October 2004.

[48] M. Haris, and H. Qu, "A CMOS-MEMS Piezoresistive Accelerometer with Large Proof Mass", *IEEE NEMS 2010, Xiamen*, China, Jan 2010.

[49] MOSIS, http://www.mosis.com/cgi-bin/cgiwrap/umosis/swp/params/ami-c5/t91t-params.txt, April 2009.

[50] P. J. French, "Polysilicon: A versatile material for microsystems", *Sensor and Actuator*, A 99(2002), 2002, pp. 3-12.

[51] Stephen D. Senturia, *Microsystem Design*, Kluwer Academic Publisher, Norwell, Massachusetts, 2001.

[52] Coventorware 2008 User Manual, Doc Ver 2008.010 Rev A.

[53] M. Haris, and H. Qu, "A CMOS-MEMS Force Sensor for Biomedical Application", *IEEE NEMS 2010, Xiamen*, China, Jan 2010.

[54] Huikai Xie and G. K. Fedder, "A CMOS z-axis capacitive accelerometer with comb-finger sensing", *13 Annual Int. Conf. on MEMS*, Miyazaki, Japan, Jan 2000, pp. 496-501.

[55] Arjun Selvakumar and Khalil Najafi, "A High-Sensitivity Z-Axis Capacitive Silicon Microaccelerometer with a Torsional Suspension", *Journal of MEMS*, Vol. 7, No. 2, 1998, pp. 192-200.

[56] S. Timoshenko and D.H. Young, *Elements of Strength of Materials*, 5th. Ed., Litton Educational Pub., Inc., 1968.

[57] Hongwei Qu, *Developement of DRIE CMOS-MEMS Process and Integrated Accelerometers*, PhD Thesis, University of Florida, 2006.

[58] Irvine Sensors, MS3110 Users Manual, Ver. 2004.

[59] Mohd Haris, Thanawit Pornthanomwong, Robert N. K. Loh, Hongwei Qu, " Nonlinear Controller and Observer Designs of a CMOS-MEMS Nano-Newton Force Sensor", *International Conference on Intelligent and Advanced System (ICIAS2010)*, Kuala Lumpur, Malaysia, 2010.

[60] D. G. Luenberger, "Observing the state of a linear system", *IEEE Transactions on Military Electronics,* April 1964, pp. 74-80.

[61] Hassan K. Khalil, *Non Linear Systems*, New Jersey: Prentice Hall Inc., 3rd Ed. 2002.

[62] Alberto Isidori, *Nonlinear Control Systems,* 3rd Edition, Springer, 1995.

[63] Robert N. K. Loh, *Optimal Control Theory (SYS 630)*, Department of Electrical and Computer Engineering, Oakland University, Rochester, Michigan, 2006.

[64] Stanislaw H. Zak, *Systems and Control*, New York: Oxford University Press, Inc., 2003.

[65] Robert N. K. Loh, *Short course of Nonlinear Observers*, Department of Electrical and Computer Engineering, Oakland University, Rochester, Michigan, 2009.